Integration of thin-film hexagonal boron nitride with photonic microstructures

by

Kyle Gregory Scheuer

A thesis submitted in partial fulfillment of the requirements for the degree of

Master of Science

in

Photonics and Plasmas

Department of Electrical and Computer Engineering
University of Alberta

Abstract

Single photon emitters hosted in hexagonal boron nitride have attracted significant attention over the past 5 years. This is in part due to their room temperature operation, chemical and physical stability, and high quantum efficiency. Continuous hexagonal boron nitride thin films (~ 10 – 20 nm thick) are of particular interest because of their potential to be integrated with existing silicon photonics devices. Additionally, there have been multiple reports of the deterministic activation of hBN emitters through the introduction of strain on the materials crystal lattice.

This thesis describes the theory, fabrication, and characterization of hexagonal boron nitride coated nano-/micro-structures as a method of both deterministically activating defect centers as well as spatially aligning them to resonant antinodes in buckled microcavity devices. First, the design and construction of an epifluorescence spectroscope/microscope instrument crucial to the optical characterization of hBN emitters, is presented. A particular emphasis was placed on accounting for undesirable autofluorescence from microscope objectives.

Next, a thin-film transfer technique for hexagonal boron nitride (hBN) multilayers was developed and refined. The technique was then used to transfer continuous hBN films to SiO_2 substrates patterned with structures ~ 100 – 200 nm in height with lateral dimensions on the order of a few μm. Blanketing the film over nanoscale-height features introduces strain on the hBN crystal lattice near feature edges, causing naturally present defects to emit across much of the visible range. Notably, the brightness of emitting arrays was characterized and shown to be much greater than emission from unintentional wrinkles in the film.

The transfer process was then used as a means of integrating hBN emitters inside recently demonstrated buckled microcavities, where two Bragg mirrors separated by a low-adhesion layer are thermally shocked resulting in the formation of a closed cavity structure due to the stress inherent to the thin films comprising the top mirror. Both the active and passive optical properties of the resulting devices were then measured. The scalability and deterministic placement provided by the hBN transfer process paired with the potential for cavity enhancement offers a promising platform for a real-world single photon source with broad applications in quantum information and computing.

Preface

Chapter 4 of this thesis was based on a version of the publication K.G. Scheuer, G.J. Hornig, and R.G. DeCorby, "A polymer transfer technique for strain-activated emission in hexagonal boron nitride" Opt. Express 27, 23633-23644 (2021). I was responsible for designing fabrication process flows, device fabrication and characterization, optical system design and construction, data collection, and manuscript preparation. I was assisted in optical system design and manuscript revisions by G.J. Hornig. R.G. DeCorby was the supervisory author and was responsible for concept formulation. R.G. DeCorby also assisted with optical system design and manuscript composition.

Some of the concepts and data contained in Chapter 5 were originally presented as K.G. Scheuer, P.S. Kirwin, and R.G. DeCorby, "Coupling Emission from Strained Hexagonal Boron Nitride Thin Films to Monolithic Buckled Microcavities" Optica Quantum Information and Measurement VI (2021). I was responsible for fabrication process flow design, device fabrication and characterization, optical system design and construction, data collection, FDTD simulation, and manuscript preparation. P.S. Kirwin assisted with fabrication, FDTD simulation, and manuscript preparation. R.G. DeCorby was the supervisory author and was responsible for concept formation and assisted with manuscript preparation.

“*Alright, alright, alright.*”

– *Matthew McConaughey* [1]

Acknowledgements

First and foremost, I would like to thank my supervisor, Dr. Ray DeCorby for his excellent guidance while I completed this degree. I am truly grateful to have had the opportunity to work in his laboratory and can confidently say that I could not have asked for a better graduate studies experience. I cannot overstate how much I appreciate his patience and willingness to work through any difficulties I encountered, regardless of his own deadlines. I aspire to one day reach the levels of kindness and patience he has achieved.

I would like to extend a particular thanks to Tim Harrison, who was quick to welcome me into the DeCorby lab and show me the ropes. I appreciated the opportunity to get involved with his research and was continuously surprised with how much confidence he placed in me. I would also like to thank Graham Hornig for his undying drive regarding headache-inducing research problems. He was always the first to enthusiastically suggest excellent ideas whenever I appeared to be stuck- which seemed to be daily.

This work wouldn't have been possible without support from other members of the DeCorby lab. Phillip Kirwin helped an incredible amount with Lumerical simulations and fabrication of buckled microcavity devices. Even though he was only here as a summer student he made a considerable impact around the lab. Thanks to Danny Pulikkaseril for his initial efforts in hBN-related projects and willingness to discuss fabrication methods; to Sanaa Al-Sumaidae for always being the first to offer help, even if that just means venting about our respective photoluminescence systems; to Lintong Bu for always being such a positive presence; to James Maldaner for showing me how to use many fabrication tools; to Seyed Azmayesh-Fard for helping me develop my critical thinking skills when it comes to open-ended problems; to Shirley Wang for being an absolute joy to work with, and to the entire University of Alberta nanoFAB staff who were always helpful and insightful when providing suggestions for my process flows.

I would like to thank my family for always knowing how to distract me from my work in the best way possible whenever they noticed I needed it. My parents have been more than encouraging during my academic career and were always excited to hear about what I was working on. I am beyond grateful for their love and support.

I also need to talk about the most important person in my life, my fiancée Samantha. I am consistently surprised by her resilience and attitude toward life. Coming home to see her is always the best part of my day and likely the only reason I’m still sane. We have been together for almost 9 years and I’m still finding new things that I love about her every day.

Finally, I was fortunate to receive support in many forms. I would like to thank the research labs of Dr. Vien Van, Dr. Robert Fedosejevs, Dr. Amina Hussein, Dr. Manisha Gupta, and Wilson Analytical Inc. for their generous sharing of expertise and equipment. This research was funded by the Natural Sciences and Engineering Research Council of Canada, Alberta Innovates Technology Futures, Alberta EDT Major Innovation Fund, Carcross Tagish First Nations, The Government of Alberta, and the University of Alberta.

Contents

List of Tables

List of Figures

List of Abbreviations and Symbols

Abbreviations

1D	one dimensional
2D	two dimensional
AZ 1512	MicroChemical AZ 1512 photoresist
AZ 1529	MicroChemical AZ 1529 photoresist
BF	bright field
BP	black phosphorus
BS	beamsplitter
CVD	chemical vapor deposition
CW	continuous wave
DBR	dielectric Bragg mirror
DBR	distributed Bragg reflector
DIC	dichroic mirror
EFL	effective focal length
FOM	figure of merit
FOV	field of view
FWHM	full-width half-maximum
hBN	hexagonal boron nitride
HG	Hermite-Gaussian
ICPRIE	inductively coupled plasma reactive ion etch
IPA	isopropanol alcohol
LAL	low-adhesion layer
LG	Laguerre-Gaussian
LPF	long pass filter
MLA 150	Heidelberg MLA150 maskless aligner
MMF	multi-mode fiber
NA	numerical aperture
ND	neutral density
NW	nanowire

OPL	optical path length
PDMS	polydimethylsiloxane
PECVD	plasma-enhanced chemical vapour deposition
PL	photoluminescence
PMMA	polymethyl methacrylate
PR	photoresist
PTFE	polytetrafluoroethylene
QED	quantum electrodynamics
QWS	quarter-wave stack
RIE	reactive ion etch
ROC	radius of curvature
ROI	region of interest
RTA	rapid thermal anneal
SEM	scanning electron microscope
SM^{3+}	samarium
SMF	single-mode fiber
SPE	single photon emitter
SPF	short pass filter
TE	transverse electric
TM	transverse magnetic
TMDC	transition metal dichalcogenide
UV	ultraviolet
VASE	variable-angle spectroscopic ellipsometer
ZYGO	ZYGO NewView 5000 optical profilometer

Symbols

E	energy
h	Planck constant
c	speed of light
λ	wavelength
I_f	fluorescence intensity

t	time
τ_0	fluorescence lifetime
k	rate constant
Θ	quantum efficiency
k_b	Boltzmann constant
T	temperature
n	refractive index
m	mass
ε	permittivity
$g^{(1)}$	first-order correlation function
$g^{(2)}$	second-order correlation function
ρ_{phonon}	crystal momentum
$\vec{K}$	wavevector
Na	lattice constant
d	film thickness
Λ	half-wave unit cell
R	reflectivity
L_{pen}	penetration depth
$\tilde{n}$	weighted index of refraction
τ_{RT}	round-trip time
$\mathcal{F}$	finesse
Q	quality factor
τ_p	photon decay rate time constant
f	frequency
z_0	Rayleigh range
z	distance along optical path
r	radius
L	cavity length
w_0	beam waist
w	beamwidth

$g_{1,2}$	stability factors
η	Gouy phase
V_0	mode volume
κ	photon decay rate
γ	non-resonant decay rate
A_{21}	Einstein coefficient for spontaneous emission
$\Delta\Omega$	angle subtended by cavity mode
W^{free}	free-space transition rate
$\lvert\vec{E}\rvert$	electric field magnitude
τ_{spon}	spontaneous emission time constant
μ_{21}	electric dipole matrix element
ε_{vac}	vacuum field magnitude
g_0	atom-cavity coupling rate
F_P	Purcell factor
W^{cav}	cavity transition rate
ω	angular frequency
$\vec{p}$	polarization
β	spontaneous emission coupling factor
d_{ap}	aperture diameter
f_{col}	collimator focal length
θ	angle
d_{core}	core diameter
d_{obj}	objective lens diameter

Chapter 1 – Introduction

The overall goal of this thesis is to successfully integrate continuous thin films of hexagonal boron nitride (hBN) into various photonic microstructures including micro-/nano-pillars, micro-/nano-holes, and buckled microcavities. Hexagonal boron nitride is part of a broad family of materials known as two-dimensional materials and it is important to discuss the properties of these materials as a whole. Light emission originating from thin film hBN has several interesting properties and potential applications which will be explored in the coming sections.

1.1. An overview of two-dimensional materials

In general terms, a two-dimensional (2D) material is a crystalline material that exists as a single layer of atoms, known as a monolayer, or a small stack of singular layers [2]. Graphene is widely regarded as the catalyst for research interest in 2D materials, since prior to the isolation of graphene it was thought that 2D materials were thermodynamically unstable and could not exist as free-standing structures. This argument was based on the fact that melting temperature dramatically decreases with film-thickness, eventually leading to decomposition or the formation of island-like structures. For this reason, the experimental study of 2D materials was limited to monolayers grown on a matching 3D crystal lattice. However, this skepticism was proven false when the existence of high quality, continuous 2D graphene crystals was discovered. Since then, many have demonstrated the high mechanical strength, high conductivity, and extreme thinness of graphene films, as well as their applications in the electronics industry [3]. These advances have prompted research into other potential 2D materials and their applications. **Figure 1.1** shows an overview of some of the most investigated 2D materials [4].

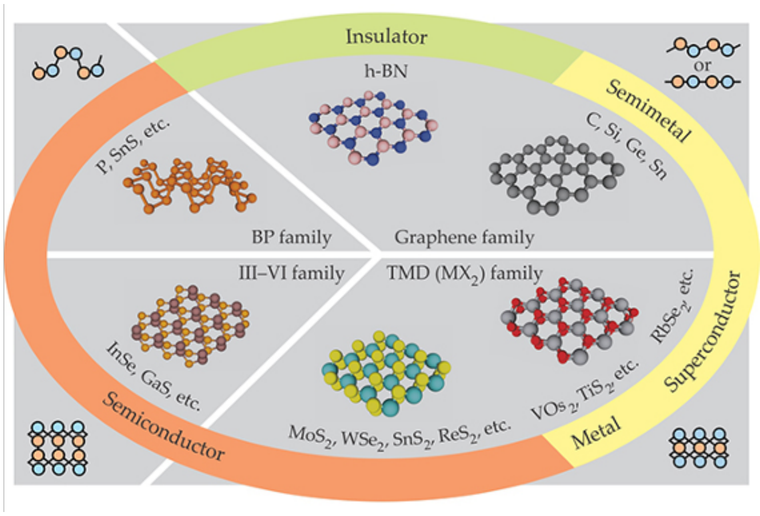

Fig. 1.1. An overview of the different families of 2D materials sorted by bandgap, atomic structure, and composition [4]. Legend: h-BN – hexagonal boron nitride, TMD – transition metal dichalcogenide, BP – black phosphorus.

One promising area for 2D materials is light-emitting layered semiconductors using transition metal dichalcogenide (TMDC) and hexagonal boron nitride (hBN) monolayers. TMDCs encompass materials of the form MX_2, where M is a transition metal (e.g. Mo or W) and X is a chalcogen element (e.g. S or Se) [2]. These materials possess strong Coulomb forces and large electron-hole binding energies which plays a central role in light emission. Such electron-hole pairs are commonly known as "excitons", and form when a 2D material absorbs a photon possessing energy just slightly lower than its bandgap energy. On the other hand, atomically thin hexagonal boron nitride boasts many interesting photonic properties, though its photo-physics are yet to be fully understood. While emission from continuous hBN films was the primary focus of the work contained within this thesis, a general overview of 2D materials and recent progress made within the field is required to give proper context.

There are many properties of 2D materials that could lead to interesting optical applications. To begin with, many 2D materials act as direct bandgap materials. The emission wavelength range and efficiency of these materials allows for interesting light emitter and detector applications [5,6]. Some 2D materials also exhibit exciton binding energies up to 100 times as strong as common III-V or II-VI semiconductors. This allows for the fabrication of new excitonic lasers and LEDs which operate at comparatively higher temperatures [7]. Another interesting property is that 2D materials are monolayers and hence have naturally passivated surfaces. This means that lattice mismatch is not an issue if one were to stack layers. It is therefore possible to create heterogeneously staggered films of 2D materials [8]. Such stacks could be useful for carrier injection and confinement in optoelectronics applications, as well as for integration into a silicon photonics platform [2]. It has also been noted that different excitonic species could be used to produce optical gain with much lower carrier density, potentially allowing for the development of new energy-efficient lasers [9]. Finally, defect-centers in 2D dielectric monolayers such as hBN have been shown to function as non-excitonic single photon emitters in certain conditions [10,11]. These properties will be explained in coming sections, with example applications given to highlight novelty.

Interestingly, 2D semiconductors are usually indirect bandgap materials in their 3D bulk form but transition to direct bandgap materials as layer thickness decreases. Because of their thinness, they exhibit decreased Coulomb screening, which is the dampening of electric fields due to mobile charge carriers [2]. This causes the valence-conduction bandgap of a given 2D semiconductor to be split into sections based on the exciton binding energy of the material, existing somewhere between the single atom model and the bulk material. The so-called optical bandgap of a 2D material is determined by its lowest excited state [9]. Techniques like photoluminescence are often useful in fingerprinting the optical transitions and relaxations of different excitons or defect centers depending on the origin of emission.

1.2. Recent progress in two-dimensional materials

1.2.1 Surface plasmon modified emission

One problem common with TMDCs is that the light emission or absorption is often weak due to defects or environmental factors. One solution to this problem involves surface plasmon polaritons (SPP). SPPs are the oscillation of free electrons at the interface of a metal and dielectric. Integrating TMDCs with metal nanostructures provides a method for enhancing performance, specifically regarding optoelectronic devices. For example, some have demonstrated an Ag nanowire/MoS_2 structure (**Fig. 1.2**(a)), in which the propagation of surface plasmons are coupled to excitons in the structure, leading to a cavity-free method of achieving 20x emission enhancement [12]. In this application, a nanowire is separated from a MoS_2 monolayer by a SiO_2 spacer to prevent undesired doping. Surface plasmon mode propagation was observed after irradiation with a 514 nm pump beam. The optical enhancement from metal nanostructure/TMDC devices is dependent on the strength of the localized field and efficiency of collection/emission. Intuitively, surrounding the hybrid structure with a strong field enhances emission, but absorption resulting from high extinction coefficients of metallic structures and the surrounding area can negatively affect emission. This implies an optimal metallic nanostructure density for emission enhancement. It is also understood that the presence of metallic nanostructures modifies the decay process since charge can transfer at the metal/dielectric interface, providing an alternate pathway. This causes a change in absorption and emission characteristics, as demonstrated using Au nanowires and MoS_2 [12]. Others have demonstrated success using similar approaches with hBN, notably with pillars [13] as well as with near-touching random plasmonic nanounits [14]. In the case of random nanounits, it was observed that the gold structures tended to provide higher enhancement factors as well as shorter decay times compared to hBN on quartz. This effect was particularly noticeable with shorter gold structures, which might be due to their tighter arrangement in combination with a larger contact area, again suggesting an optimal metallic density.

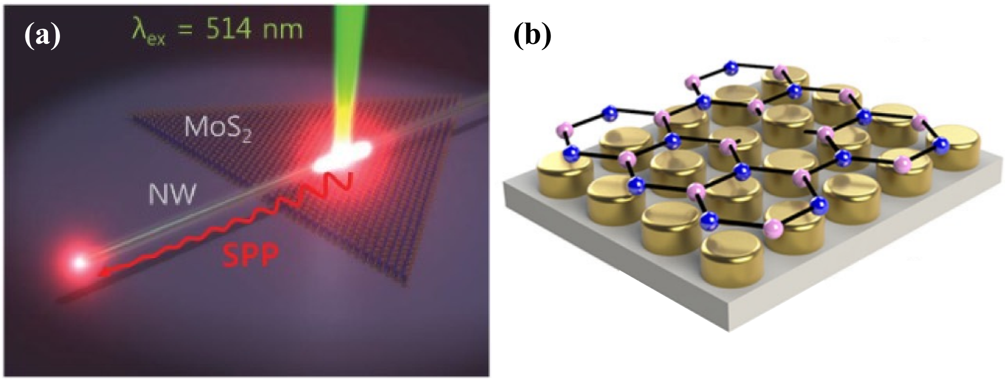

Fig. 1.2. **(a)** Schematic of a MoS_2/Au structure. Light emission is enhanced when laser light is incident on the Au nanowire as compared to just the MoS_2 structure [12]. **(b)** Schematic of a hexagonal boron nitride monolayer (alternating blue and pink) on top of a plasmonic nanostructure (gold) [14].

1.2.2 Ultraviolet detection and emission

Two-dimensional materials have recently been demonstrated to have applications in the ultraviolet (UV) region as both efficient photodetectors and UV lasing mediums [15].

In terms of photodetection, few-layer black phosphorus possesses some of the most attractive qualities including a broad detection range (310 – 390 nm), an extremely high responsivity (9×10^4 AW^{-1}), and a fast response time (4 ms) [16]. Many of the TMDCs have been shown to be good candidates for UV detection, including WS_2, MoS_2, and hBN. There have been reports of flexible MoS_2-based detectors, as well as other self-powered (*i.e.,* not requiring an external source), flexible detectors comprised of hybrid materials [15].

In terms of UV emission, hBN is currently one of the most promising materials for compact UV laser applications as it is a direct bandgap material emitting in the UV region and exhibits room-temperature lasing when excited via cathodoluminescence [17,18]. One particularly exciting detail is that the characteristic sharp single emission peak near 215 nm is over 10^3 times more intense than emission at the same wavelength from type IIa pure diamond. This type of emission in hBN has been attributed to localized exciton trapping near both grain boundaries and dislocations [19].

1.2.3 Staggered heterostructures

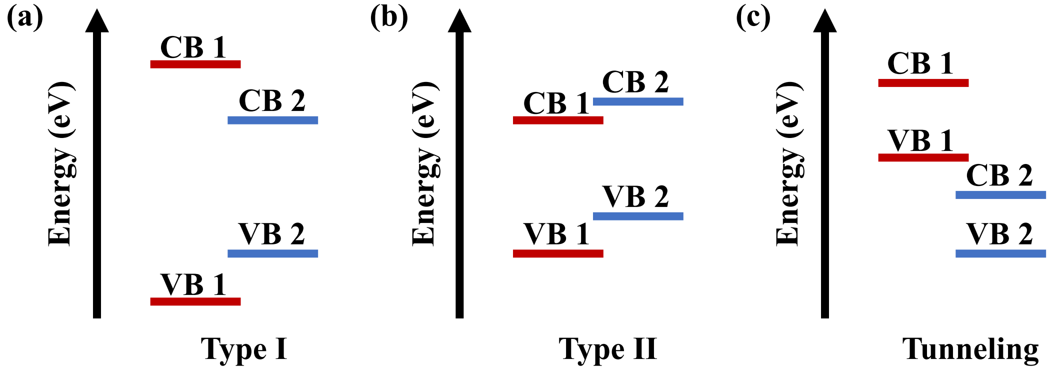

Fig. 1.3. Band structures for various 2D material heterostructures. **(a)** A type I heterostructure where one bandgap lies inside the other. **(b)** A type II heterostructure where one of the conduction bands is higher and one of the valance bands is lower. **(c)** A tunneling heterostructure where there is no overlap between the bandgaps.

The mechanical stacking of 2D materials offers flexibility in terms of fabrication methods, material choice, and bandgap characteristics. These characteristics are determined by material choice, sequence, thickness, and alignment. There are three types of 2D heterostructures: type I, type II, and tunnelling. The categorization of a heterostructure depends on the energy band alignment of the materials used.

In type I heterostructures, the valance band maximum and conduction band minimum of one material fits within the energy band of the other material (**Fig. 1.3**(a)). This is traditionally how quantum wells were fabricated. In terms of 2D materials, MoS_2 and RbS_2 have been used to show that carriers injected into the wide bandgap material (MoS_2) will rapidly transfer into the narrow bandgap material (RbS_2), but not the other way around [20]. **Figure 1.4**(a) shows a band diagram for this material combination. This is a novel method of carrier confinement that has applications in future nanoelectronics (diodes, transistors, etc.).

In type II heterostructures (**Fig. 1.3**(b)), there is some overlap between bandgaps of the wide and narrow bandgap materials, leading to an accumulation of charge in each layer. For example, MoS_2 and WS_2 have been used to demonstrate ultrafast carrier transfer between the two layers, as shown in **Fig. 1.4**(b). There is currently much interest in using type II nanoscale heterostructures for photocatalysis, specifically water splitting using solar energy [21].

Finally, tunnelling heterostructures are formed by stacking a TMDC and an insulator so that there is no bandgap overlap at the material junction (**Fig. 1.3**(c)). hBN is typically chosen as the insulator due to its large bandgap (~ 6 eV). When an electrical bias is applied across the layers, charge carriers can tunnel through the barrier and recombine in the TMDC layer. This type of heterostructure functions as a quantum well, where the movement of charge carriers can be restricted to the vertical direction, leading to improved performance in laser diode applications. In the case of **Fig. 1.4**(c), the authors used the heterostructure as a light-emitting transistor. They showed that sandwiching a layer of WSe_2 between hBN tunnel barriers can produce quantum wells with enhanced room temperature performance [22]. This achievement is notable, since previous devices used $MoSe_2$, which shows comparably poor operation at higher temperatures.

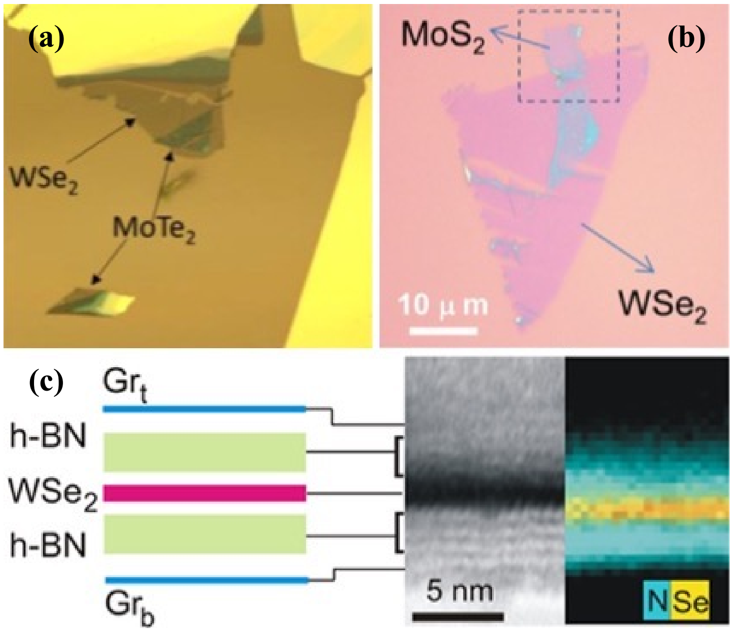

Fig. 1.4. (a) An example of a $WSe_2/MoTe_2$ type I heterostructure [23]. **(b)** An example of an MoS_2/WS_2 type II heterostructure [21]. **(c)** WSe_2/hBN tunnelling heterostructure schematic and corresponding image [22].

1.2.4 Defect-center originated emission in two-dimensional materials

Recently, SPEs have been discovered in TMDC and hBN monolayers. In the case of the TMDCs, it is widely regarded that defects in the crystal lattice act as exciton trapping sites [24,25]. For example, some have shown that WSe_2-based SPEs possess excellent spectral stability and could be useful in niche optoelectronics applications [26]. These emitters originate near surface edges of the material, as shown in **Fig. 1.5**(a) and have been shown to have spectral widths below 120 μeV. More relevant to current research, single photon emission from hBN has attracted much attention in recent years [11]. Defects hosted in hBN typically occur deep within its 6 eV bandgap and the emission mechanisms are not yet well-understood [11,27]. Regardless, hBN SPEs are of particular interest because of their polarized emission and narrow bandwidth, properties which are necessary to achieve higher signal-to-noise ratios in quantum communication applications. The comparatively narrow lineshape of an hBN SPE at room temperature is due to the fact that electronic transitions predominantly occur at the zero-phonon line rather than within the phonon sideband. Another novelty concerning hBN is that it can function as an SPE at room temperature, though the lineshape is greatly narrowed as temperature is decreased. **Figure 1.5**(b) shows arrays of hBN SPEs fabricated using a strain-activated technique [24]. **Table 1.1** provides a list of materials capable of single photon emission as well as operational temperatures and relevant comments.

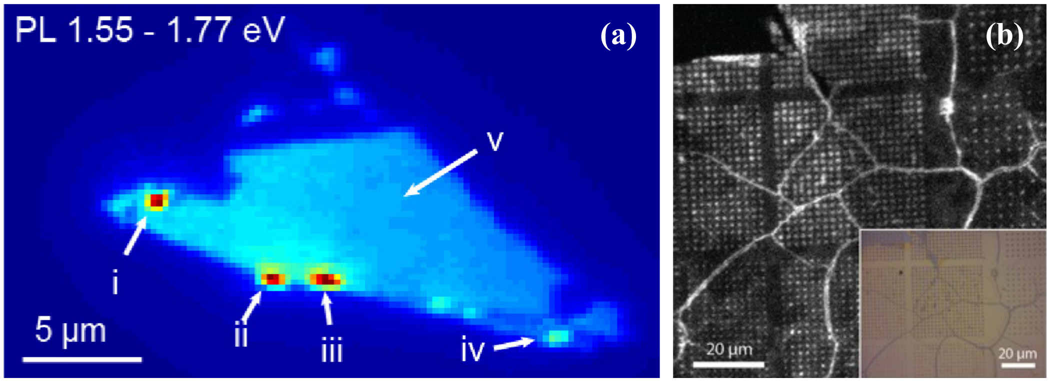

Fig. 1.5. Examples of wide-field photoluminescence imaging. **(a)** Photoluminescence intensity map of a WSe_2 flake [26]. **(b)** Photoluminescence intensity map of an hBN film transferred to a prepatterned substrate. The inset shows a bright field image of the corresponding region [24].

Table 1.1. Two dimensional materials that are currently known to be capable of single photon emission [25,28].

Material	Emission Wavelength	Operational Temperature	Relevant Comments
hBN	UV – NIR	Room Temperature	Brightest of the sources, extremely robust
WSe_2	~730–750 nm	Cryogenic	Fairly robust
WO_3	~620–730 nm	Room Temperature	Multilayers produced by thermal annealing of WS_2
WS_2	~640 nm	Cryogenic	-
GaSe	~600 nm	Cryogenic	Only multilayers
$MoSe_2$	~770 nm	Cryogenic	Photon emission statistics not characterized
MoS_2	~690 – 730 nm	Cryogenic	Often hBN encapsulated

1.3. Hexagonal boron nitride

Commonly referred to as “white graphene”, hexagonal boron nitride is currently one of the most heavily studied and most promising materials for quantum computing, quantum information, and quantum sensing [11,24,25,29,30]. It is comprised of alternating boron and nitrogen atoms in a hexagonal pattern as the name would suggest. Atomically thin hBN is remarkably robust, and was initially used as an encapsulating material for graphene until its own optical and electronic properties were realized [25]. In-plane B-N bonds are polar-covalent, but the only bonding between adjacent sheets comes from weak van der Waal forces, making it ideal for 2D applications [11]. Additionally, hBN shows bright single photon emission at room temperature, which is a rather unique property that cannot be overemphasized.

1.3.1 Hexagonal boron nitride transfer methods

There are four distinct methods for integrating hBN onto silicon-based devices. The first is dry transfer and variations thereof. The most well-known variation was used to isolate few-layer graphene and is commonly referred to as the "scotch tape" method [31], where graphene flakes are mechanically exfoliated by repeated peeling using scotch tape. The same technique has been modified and applied to hBN [32]. The strength of this type of transfer lies in its simplicity and low cost, but it is rather limited in terms of controlled placement and scalability. The second transfer method, and the one studied herein, is wet transfer. This type of technique relies on wet etching and intermediate carriers, typically a polymer, to transfer a thin film onto a substrate. Interest in polymer-assisted transfer processes for 2D materials also began with graphene [33] and recent progress has been made in developing wafer-scale transfer techniques [34,35]. In one method, graphene grown on a metal layer is lifted off using a polymer (such as PDMS or thermal tape) followed by soaking in solution. These continuous films can then be transferred to arbitrary substrates. Others have demonstrated successful polymer transfers with TMDCs using variations of wet transfer techniques [36]. Wet transfers of hBN can achieve good coverage but are generally more complex and time-consuming compared to dry transfer. The third transfer method is drop-casting, where a solution containing suspended hBN flakes is placed on a substrate. The host solution then evaporates leaving the hBN flakes on the samples surface [37]. This type of transfer is very simple and highly suited for small-scale studies. Some have demonstrated deterministic placement of hBN by "squeegeeing" small crystals across a patterned substrate [38]. Finally, there have been reports of direct growth of hBN on SiO_2 and sapphire substrates [39–41]. Direct growth can provide excellent coverage and film quality but requires specialized fabrication equipment and is still in its infancy. The collection of transfer methods used to converge on a set of parameters used in this work is presented in **Table 1.2** along with brief descriptions about each method.

Table 1.2. Various methods for the wet and dry transfer of hBN and related relevent materials.

Ref	Sample	Transfer Method	Resist/Adhesive Type	Spin/Bake Settings	Etchant	Resist Remover	Notes
[24]	20 nm hBN on 20 um Cu foil from Graphene Supermarket	Wet	PMMA	90 s bake at 180 C	Ferric chloride at 60 C	Acetone bath at 52 C for 90min	Used RCA 1 and 2 baths following Cu etch. Sample was heated for 20 min before acetone bath.
[35]	Graphene on Ni	Wet	PMMA	Not Given	Aqueous HCl	Acetone	Films can withstand sonication or acid treatment. Transferred films can be attached to most surfaces.
[42]	Pressed few-layer graphene onto hBN	Dry	Gelfilm and Nitto tape	N/A	N/A	N/A	Adhere target sample to gelfilm and use nitto tape to do mechanical exfoliation of bulk crystal. Stamp crystal onto target sample.
[43]	Monolayer and multilayer hBN/Cu samples from graphene supermarket.	Wet	PMMA	2000 rpm for 2 min	68% HNO_3 for 2 min	Placed on Si substrate, heated to 80 C, slow acetone flow	Dried with N_2. Annealed at 850 C to achieve maximum fluorescence intensity
[44]	Lab-grown hBN crystals	Exfoliated	N/A	N/A	N/A	N/A	Exfoliated onto SiO_2. hBN annealed at 850 C, 1Torr for 30 min.
[45]	Commercially available flakes from Graphene Supermarket in water/ethanol	Drop-cast	N/A	N/A	N/A	N/A	Sonicated to break up agglomerations. Drop-cast onto a Si wafer with iridium layer to enhance photon collection. Heated to 70 C to evaporate liquid.
[37]	Commercially available flakes from Graphene Supermarket in water/ethanol	Drop-cast	N/A	N/A	N/A	N/A	Drop-cast onto Si/SiO_2 and waited for the solvent to dry.
[46]	Grew hBN on Cu foil using CVD	Drop-cast	N/A	N/A	N/A	N/A	Drop-cast onto TEM grid. Dried in vacuum at 80 C and annealed for two hours at 200-220 C. Low temperature for TEM grid.
[47]	Grew hBN on Cu foil using CVD	Electro-chemical Delamination	N/A	N/A	N/A	N/A	Annealed at 850 C for 30 min with Ar flow following transfer.

[48]	hBN/Cu (25um) foil from Graphene Supermarket	Wet	PMMA	3500 rpm for 60 seconds. Cured at room temperature overnight	Ammonium persulfate (15 g/L) solution	Acetone rinse after 30 min annealing at 180 C	Scooped hBN film from etchant using target substrate.
[49]	Exfoliated hBN flakes from powder	Dry	PDMS stamp with PC layer that was melted to release	N/A	N/A	N/A	PC layer dissolved in chloroform. Samples annealed in Ar/H_3 at 350 C for 1 h.
[49]	Monolayer CVD-hBN grown on both sides of a Cu foil	Wet	PMMA	Not Given	0_2 dry plasma.	Acetone bath at 40 C for 10 min	Annealed on hotplate at 180C for 2min to remove remaining water following
[50]	hBN on Cu foil	Wet	PMMA	2500 rpm for 1 min	CE-100 Transene to etch copper, followed by 10% HCL (Fe)	Acetone vapor and thermal annealing at 450 C for 2 h with H_2/Ar	$FeCl_3$ is a by-product of the Cu etchant, so they used a Fe etchant afterward.
[38]	hBN nanocrystal clusters	Drop-cast	Patterned PMMA	N/A	N/A	Acetone bath for 1 min	Sample was 0.2 g/L multilayer hBN platelets in water.

1.3.2 Origins of emission in hexagonal boron nitride

It has long been known that boron nitride fluoresces in the UV region, a phenomena which is believed to be caused by exitons trapped at structural defects [19]. hBN has also found a home in infrared nanophotonics as a hyperbolic material, a special case of birefringence where the permittity also has an opposite sign along orthogonal axes [11]. There have even been recent reports of second harmonic generation from hBN flakes [51,52]. However, it was relatively recently that hBN began to attract interest in the quantum information community as a host for promising single photon emitters [43].

At the time of writing, the exact atomic origins of single photon emission from hBN are still heavily debated [24,53–57]. However, the community agrees that some form of atomic defect hosted within the hBN lattice is likely responsible. Several of the most promising theories are presented in the following section. Quantum emitters in hBN were first discovered in 2015 in a multilayer film that was transferred to a silicon substrate and annealed at high temperatures [43]. Operating on the assumption that the emitters were intrinsic to monolayers and multilayers of hBN, density functional theory was used to investigate potential origins of emission. The initial conclusion was that the N_BV_N defect (nitrogen occupied boron site with neighbouring nitrogen vacancy) was the likely candidate based on its ground to excited state energy and high degree of anisotropy.

Around the same time, a theory surfaced suggesting that so-called Stone-Wales defects might be stable in hBN [58]. Stone-Wales defects are the simplest defect in graphene-esque materials, and occur when a bond is rotated 90° in-plane about its center. Density functional theory was used to investigate the structural and electronic properties of these defects and it was noted that carbon related defects, and specifically the C_B defect (carbon occupied boron site), are likely to form in a Stone-Wales formation.

Another theoretical proposal based on density functional theory was made in 2017, suggesting that the C_BV_N (carbon occupied boron site with neighbouring nitrogen vacancy) defect might be the dominant source of photoluminescence within hBN [55]. This proposition was based on the Huang-Rhys (HR) factor, which predicts the relative strengths of the zero phonon line and phonon sidebands based on electronic and vibronic states. It was found that the delocalized phonon modes dominated the photoluminescence lineshape of the C_BV_N defect, whereas strongly localized modes dominated the lineshape of the N_BV_N defect.

In 2018, a theory was put forward that strain might play an important role in the activation of single photon emitters in hBN [24]. Transferring multilayer hBN films to a prepatterned substrate resulted in emission that preferrentially occurred near the edges of substrate features. After ruling out substrate-induced electrostatic effects as well as piezo-induced potential, it was thought that charge trapping occurred near the regions of highest strain, leading to the formation of potential wells. While this might sound similar to the exitonic emission seen in UV hBN emitters and the TMDCs, the physical mechanisms are not the same. Single photon emitters in hBN are the result of mid-bandgap defects rather than excitons trapped near the edges of the conduction and valance bands. Others have reported emitter formation near strained film regions, though the exact mechanism may differ [27,59–61].

A second theory arose from 2018 observed that the use of an argon plasma treatment could significantly increase emitter density near the surface of hBN flakes [56]. It was suggested that oxygen might be responsible for the defects observed in this case, with the V_BO_2 defect (boron vacancy saturated with two oxygen atoms) given as the most likely candidate.

In 2020, another first-principles study was carried out involving the vibrationally resolved optical fingerprint of a spin-triplet unique to the V_NC_B defect (nitrogen vacancy with a neighbouring carbon occupied boron site.) [54]. Notably, the calculated photoluminescence line shape was in excellent agreement with experimental results.

In 2021, a study was conducted that involved testing various impurities in hBN through ion implantation and bottom-up synthesis [53]. It was found that only the ion implantation of carbon resulted in the formation of visible range single photon emitters. Yet another computational analysis was performed, this time suggesting that the $V_BC_N^-$ defect (negatively charged boron vacancy with a neighbouring carbon occupied nitrogen site) might be responsible.

Table 1.3 summarizes each of the potential candidates speculatively behind single photon emission in hBN. While some claim to have settled the debate, there are still many conflicting findings that have yet to be unified by a single theory. Perhaps the most realistic explanation is that the photophysics behind single photon emission (and emission in general) in hBN are extraordinarily complex, and that there may be a number of causes and mechanisms [46].

Table 1.3. Various proposed mechanisms of single photon emission in hBN.

Year	Emission Mechanism	Reference
2016	N_BV_N defect	[43]
2016	Stone-Wales C_B defect	[58]
2017	C_BV_N defect	[55]
2018	Charge trapping near strained regions	[24]
2018	V_BO_2 defect	[56]
2019	Strain related near edges	[27]
2020	V_NC_B defect	[54]
2021	$V_BC_N^-$ defect	[53]

1.3.3 Strain activation in hexagonal boron nitride

There have been several reports of hBN emitter activation via strain in the literature. Interestingly, the proposed mechanisms vary widely, again suggesting rather complicated origins of emission. **Figure 1.6** showcases several of the reported emitter activation schemes that involve strain. The controlled-edge creation method, shown in **Fig. 1.6**(a), involves the creation of patterned hBN features by focused ion beam milling [27]. Single photon emitters tend to occur near the milled edges of the hBN film. However, this method shows the greatest success when performed in a wrinkle-free region, suggesting that the exact mechanism is somewhat complicated. Others have had success inducing strain by puncturing an hBN film with an atomic force microscope followed by argon annealing (**Fig. 1.6**(b)) [62]. These two methods have the advantage of fabrication on a flat, non-patterned substrate which is useful in an integrated photonic perspective. One of the earlier methods involved transferring an hBN film onto prepatterned substrates, typically nanopillars [24], where the strained regions are theorized to induce charge trapping, functioning as potential wells. Finally, emission originating from wrinkles and delaminated areas have been commonly reported. One such example is provided in **Fig. 1.6**(d), where an ultra-stable quantum emitter formed in the center of a bubble between an exfoliated flake and the underlying substrate [60].

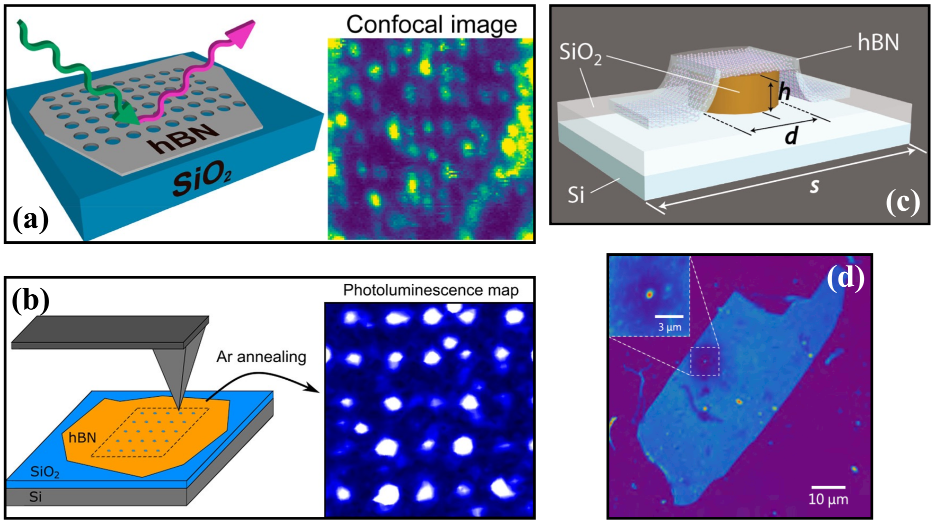

Fig. 1.6. Various methods of activating hBN emitters via strain. **(a)** Controlled edge creation method [27]. **(b)** Atomic force microscope indentation [62]. **(c)** Transfer to nanostructures [24]. **(d)** Emitter formation at bubbles in film [60].

1.3.4 Optical cavities and hexagonal boron nitride

The room-temperature operation and fabrication robustness of hBN make it a naturally good candidate for various optical resonator schemes. The concept of stain-activation also provides a method of deterministically aligning defect centers with cavity resonances. By introducing an emitter into a well-suited cavity it is possible to modify its rate of spontaneous emission as well as channel the emitted light into a cavity mode [63]. Such a device would be highly useful as a single photon source since the emitted photons would occupy the same spatial-spectral mode. One of the largest challenges in cavity integration is achieving spatial alignment between cavity resonance and an hBN emitter, which has led to a search for deterministic emitter activation [64]. Initial attempts at cavity-coupled emission typically involved either pre-locating emitters prior to fabrication or hybrid systems where the effective cavity size and placement can be modified. **Figure 1.7**(a) shows an example of a 1D photonic crystal structure that has been etched into an hBN flake supported by a silicon nitride layer [65]. An initial survey of emitters in the hBN flake was conducted before fabricating the cavity to align the resonator structure with respect to the emitters. **Figure. 1.7**(c) shows an example of a hybrid system formed between a dielectric Bragg mirror and a mirrored fiber [66]. A mobile cavity is formed between the fiber and mirror that allows individual emitters to be probed. The cavity length can be modulated by moving the fiber along the z axis indicated in the diagram which provides a method of tuning. **Figure. 1.7**(b) shows an example of a micro-ring resonator cavity where hBN has been transferred to the surface, resulting in deterministic activation around feature edges [67].

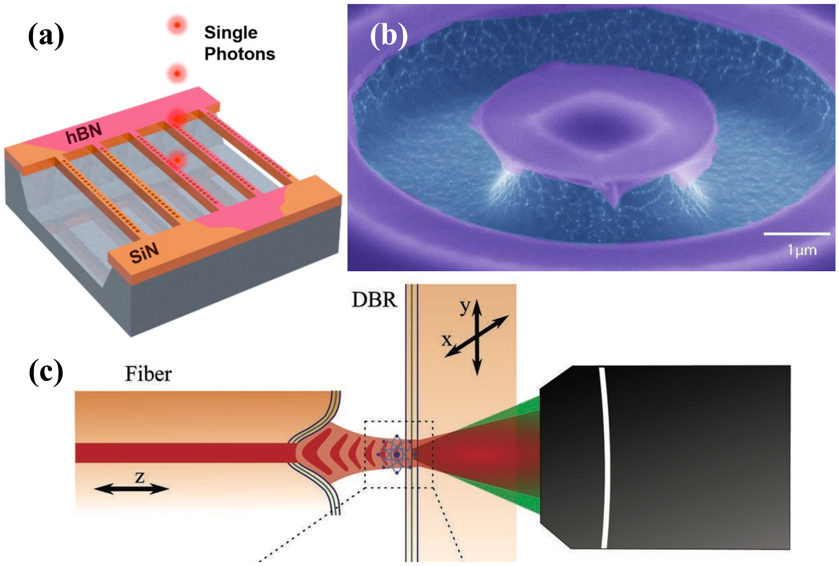

Fig. 1.7. Various hBN resonator schemes. **(a)** A schematic showing single photon emission from hBN coupling to the resonant modes of silicon nitride photonic crystal cavities [65]. **(b)** An SEM image showing hBN (purple) coating the surface of a silicon nitride (blue) micro-ring resonator [67]. **(c)** A schematic showing a hybrid system where an hBN emitter is enclosed in a hemispherical cavity comprised of a distributed Bragg reflector (DBR) and mirrored fiber [66].

1.4. Monolithic buckled microcavities

The DeCorby group has recently presented a type of optical microcavity that might be suitable for integration with hBN emitters. The devices are based on a plano-concave cavity formed by two dielectric Bragg reflectors (DBR). The fabrication process is described roughly as follows. After the first DBR is deposited on a wafer, a low-adhesion layer, typical a fluorocarbon, is deposited and patterned using a lift off technique. A second DBR is then deposited directly on top of the patterned low-adhesion layer. Cavities are formed by thermally shocking the substrate which causes the top mirror to buckle where the low adhesion layer was patterned due to the compressive stress inherent to the mirror layers. This micro-electro-mechanical-like self-assembly process results in highly geometrical symmetrical devices with predictable morphology and interesting optical properties. The height of the air gap formed between the two mirrors during the buckling process can be somewhat controlled by engineering the diameter of the low-adhesion feature and top mirror material properties. It is also worth noting that buckling is not limited to a circular geometry, and that square, donut, elliptical, and waveguide structures have also been explored.

The DeCorby group has made recent progress with these devices. Notable examples in include: (i) The integration of a free-standing silicon nitride film to form a membrane-in-the-middle optomechanical system [68]. (ii) The creation of open access cavities with the proposal of introducing emitters hosted in fluid such as rubidium vapor or quantum dots in solution [69]. (iii) Demonstrating tunability in closed-form cavities, both through changes in temperature [70] as well as pressure [71]. The domes appear to be an excellent candidate for integration with 2D materials, especially since monolithic resonator schemes with three-dimensional confinement have proven particularly elusive. Of all the 2D materials, hBN appears most approachable considering its robustness in terms of fabrication techniques and bright, room-temperature operation of the emitters hosted within hBN. Regardless of the exact origins of emission in hBN, strain has been shown to lead to the deterministic formation of single photon emitters. The goal pursued in this thesis work is to introduce patterned microstructures inside buckled microcavities, thus providing a method of aligning an emitting defect in hBN to an optical mode in a buckled microcavity. A schematic representation of this idea is shown in **Fig. 1.8**.

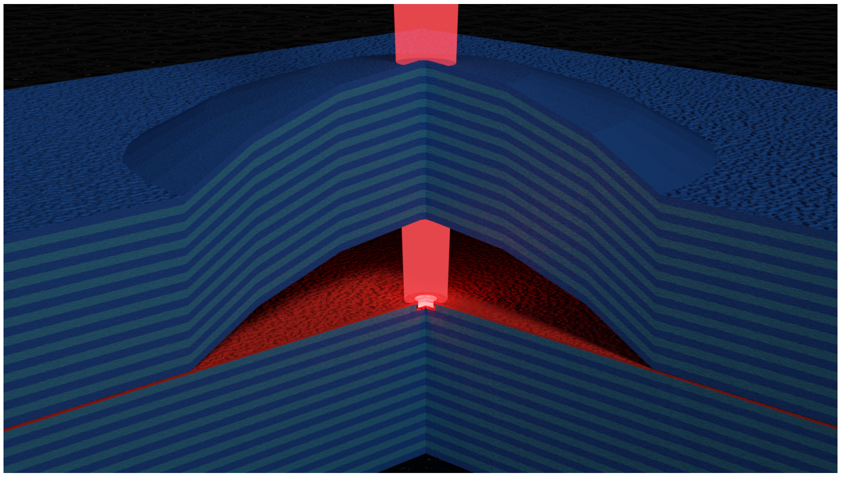

Fig. 1.8. A cross-sectional artistic rendering of the overall goal of this thesis – cavity-coupled emission from hexagonal boron nitride. The Ta_2O_5/SiO_2 layers of the Bragg mirrors are shown in dark blue/light blue, respectively. Emission from a continuous hBN film (red) is shown coupling

into the mode of a buckled microcavity (not to scale). A small hole has been etched into the top layer of the bottom mirror to align defect-based emission in transferred hBN to cavity modes.

1.5. Outline of thesis

This thesis begins by presenting relevant theory and contextual background information in Chapter 2. This can be broken into two sections. First, properties of quantum emitters are presented, with particular emphasis on hBN. Second, the underlying optical theory behind dielectric Bragg mirrors and Fabry-Perot cavities is laid out. The two sections are then tied together and emission enhancement using optical cavities is described.

Chapter 3 begins by describing the construction of an epifluorescence microscopy/spectroscopy station designed for measuring defect-originated emission in hBN. The system is then used to study the autofluorescence properties of objective lenses in the context of their potential to interfere with the identification of quantum emitters in a target sample. A brief discussion on planar Bragg mirrors and measurement techniques is also provided.

Chapter 4 presents a polymer-assisted technique that was devised for transferring continuous thin-films of CVD-on-copper hexagonal boron nitride to silicon wafer substrates. Moreover, the technique inherently serves to deterministically activate hBN emitters as the film comes into contact with prepatterned features on the target substrate as others have demonstrated [24]. The resulting emission is then optically characterized using a combination of photoluminescence imaging and spectroscopy.

Chapter 5 explores the integration of hBN thin films into Fabry Perot devices using the polymer-assisted transfer technique from the previous chapter. Simulation data is presented and ultimately used to devise a process flow for fabricating hBN-embedded buckled microcavity devices. Preliminary optical results are presented in the form of photoluminescence imaging and spectroscopy. Optical properties of the unloaded domes are also discussed.

Chapter 6 provides a summary of this thesis and gives direction for future work involving both cavity-coupled emission and quantum emitter work in general. The appendices provide additional fabrication and characterization information for Chapters 3, 4, and 5 as well as a streamlined Lumerical code for simulating buckled microcavities.

Chapter 2 – Theory and background

2.1 Optical properties of emitters

2.1.1 Photoluminescence

In general terms, photoluminescence is the emission of light after a material has absorbed photons. The process occurs via photoexcitation, where the absorption of a photon excites an electron to a higher energy state. Upon relaxation the electron releases a lower-energy, and therefore longer wavelength, photon [72]. Two distinct forms of photoluminescence are fluorescence and phosphorescence. The difference between fluorescence and phosphorescence lies in the spin of the excited states. In the case of fluorescence, the spin of the excited electron is opposite of the ground state resulting in an angular momentum difference of ħ, as required for angular-momentum-conserving emission of a photon It is also possible for the excited state to have the same spin as the ground state, provided an electronic conversion occurs during the emission process, in the form of an intersystem crossing. The relaxation of an electron in a triplet state to the ground state results in phosphorescence, which typically has longer lifetime due to the shift in electronic state, sometimes even lasting hours [73]. In contrast, fluorescence lifetime is typically on the order of nanoseconds [73]. A Jablonski diagram showing different excitation and relaxation process can be seen in **Fig. 2.1**. Phosphorescence typically occurs at longer wavelengths than fluorescence, a fact that can be explained by lower energy level of the triplet state after an intersystem crossing since the emitted photon would have a characteristic wavelength inversely proportionate to the phosphorescent transition ($E = hc/\lambda$).

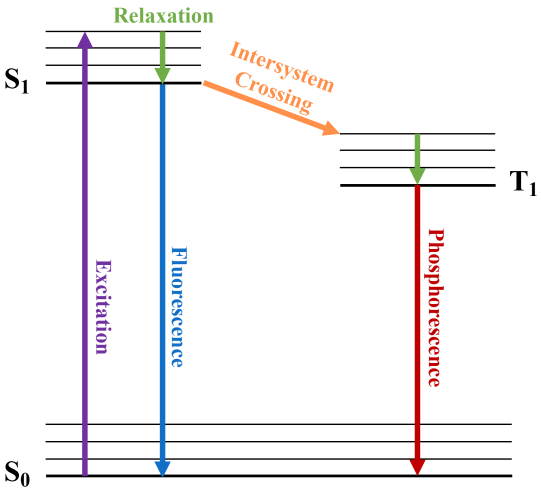

Fig. 2.1. A Jablonski diagram illustrating the difference between excitation, fluorescence, and phosphorescence. Adapted from [74].

It is commonly known that the decay rate of a molecule to its ground state typically follows an exponential decay law which can be expressed as:

$$I_f(t) = I_0 \exp\left(-\frac{t}{\tau_0}\right). \tag{2.1}$$

Here, $I(t)$ is the fluorescence intensity at time t, I_0 is the initial fluorescence intensity upon excitation, and t_0 is the fluorescence lifetime, defined by a decrease in fluorescence intensity by $1/e$ (*i.e.,* the average time the molecule spends in an excited state before emitting a photon and returning to ground state [74]) . The fluorescence lifetime can be written as [74]:

$$\tau_0 = \frac{1}{k_f + \sum k_{nr}}. \tag{2.2}$$

Here, k_f and k_{nr} are the fluorescence and non-radiative rate decay constants, respectively. It naturally follows that the quantum yield (Φ) is the probability that a photon is emitted after a photon has been absorbed, which can be expressed in terms of the rate constants [74,75]:

$$\Phi = \frac{\text{photons emitted}}{\text{photons absorbed}} = \frac{k_f}{k_f + \sum k_{nr}}. \tag{2.3}$$

Quantum efficiency, on the other hand, is the probability that a photon will be emitted only after the system has been excited to its emitting state [76]. It then follows that quantum yield and quantum efficiency will be equal in a two-level system; however, it is possible for quantum efficiency to be higher than quantum yield in a system where complicated pathways are present [77,78]. Quantum efficiency is a very important material characteristic, especially concerning lasers, LEDs, and light-emitting devices in general [2,8,79]. Unlike in hBN, QE measurements of TMDCs are challenging due to the low sensitivity of such materials, meaning that specialized techniques often need to be developed for light collection. One way to get around this is to compare the PL spectra at room temperature to a much lower temperature, since QE increases as temperature approaches absolute zero. Another common method is to surround a TMDC with hBN (acting as a wide bandgap dielectric) as a means of emission enhancement [80]. Others have had success increasing the QE by using super acid chemical treatment on very specific sulfur-based materials [79].

Crystal quality and purity is extremely important in 2D materials and can be quantified from linewidth and carrier lifetime measurements. The presence of unwanted defect centers in the bandgap can cause broadening of spectral features which can be revealed by techniques such as PL spectroscopy. The degree of broadening is often used to gauge material quality [2]. For example, the linewidth at the full-width-half-maximum (FWHM) might be compared to a theoretical value in order to determine how much background emission is present, and from there the material quality (or defect density) can be assessed. Excitonic transitions are often the dominant features in PL measurements of many TMDC materials. Under certain conditions, multiple exciton species can exist; this makes characterization of the material difficult due to complicated, multi-step decay pathways. However, time-resolved PL, photoconductance measurements, and ultrafast pump–probe techniques can be used to determine a large range of possible carrier lifetimes [81]. Using bi-exponential decay fits, lifetimes have been found to range between picoseconds to nanoseconds for excitons in a TMDC monolayer, and SPEs in hBN typically have lifetimes on the order of nanoseconds. Carrier lifetimes have been linked to material quality, and are dependent on stacking, thickness, and temperature, among other factors.

2.1.2 Single photon emission

The instantaneous field intensity and first-order correlation function can be written in terms of the quantized, time-dependent electric fields $E^{(+)}(t,\vec{r})$ and $E^{(-)}(t,\vec{r})$. Note also that the position of the electric field $\vec{r}$ becomes the operator, however spatial coherence can be neglected to obtain quantities that pertain only to time [82]:

$$I(t) = 2\varepsilon_0 c \langle E^{(-)}(t) E^{(+)}(t) \rangle, \tag{2.4}$$

$$g^{(1)}(\tau) = \frac{\langle E^{(-)}(t+\tau)E^{(+)}(t)\rangle}{\langle E^{(-)}(t)E^{(+)}(t)\rangle}. \tag{2.5}$$

From this arises the intensity-intensity correlation function, commonly referred to as the second-order correlation function, which gives the statistical character of intensity fluctuations and can be written in both classical and quantum forms:

$$g^{(2)}(\tau) = \frac{\langle I(t+\tau)I(t)\rangle}{\langle I(t)\rangle^2} = \frac{\langle E^{(-)}(t+\tau)E^{(+)}(t+\tau)E^{(-)}(t)E^{(+)}(t)\rangle}{\langle E^{(-)}(t)E^{(+)}(t)\rangle^2}. \tag{2.6}$$

The application of the second order correlation function to quantum emitters lies in measuring so-called photon antibunching, where photons are emitted one by one and separated by a time delay [82]. The importance of this metric can be illustrated by considering a two-level system, where the ejection of a photon is the result of an energy transition to the ground state. Another excitation cycle would then be required to produce a second photon, meaning that a time delay between photons must be present in this case. It is worth noting that such a time delay cannot easily be detected due to the detection frequency of modern photodetectors resulting from a dark period between detection events commonly referred to as a "dead-time". One way around this inconvenience is to split the emission between two detectors using a beamsplitter and plot a histogram of coincidence events in what is known as a Hanbury Brown-Twiss (HBT) measurement, a schematic for which can be seen in **Fig. 2.2**.

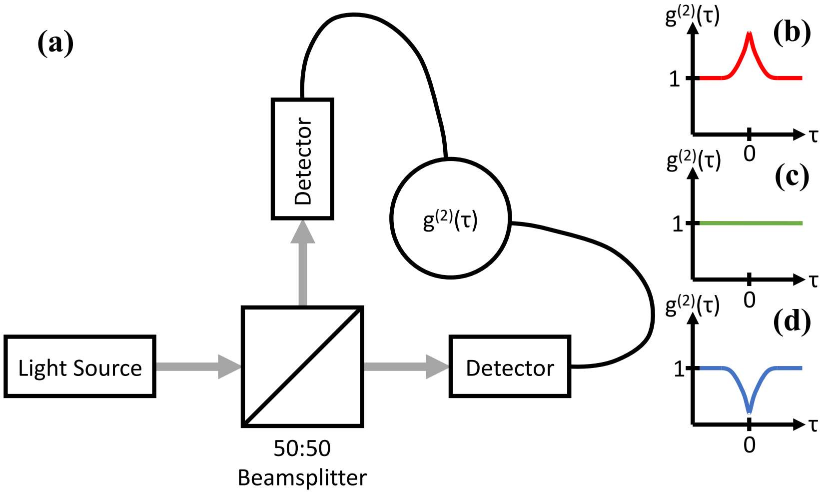

Fig. 2.2. Second-order correlation measurements. **(a)** A schematic showing a typical Hanbury Brown-Twiss measurement setup. **(b)** Example correlation plot for a thermal source. **(c)** Example correlation plot for a coherent source. **(d)** Example correlation plot for an anti-bunched source.

For a source emitting perfectly antibunched light the probability of detecting a photon at both detectors without any time delay should be zero:

$$g^{(2)}(0) = 0. \tag{2.7}$$

This behaviour cannot be explained classically as it contradicts the Cauchy-Schwartz inequality, which states that $\langle \mathrm{I}(\mathrm{t}+\tau)\mathrm{I}(\mathrm{t})\rangle \leq \langle \mathrm{I}(\mathrm{t})^2\rangle$. An example of second-order correlation functions for various light sources can be seen in **Fig. 2.2**. Simply put, the closer the minimum on the plot is to zero at $\tau = 0$, the lower the probability of detecting more than one photon at a given time and the more ideal the single photon emitter [25]. This hints at the quantum properties of light and is a very important figure of merit when designing a device that supposably emits a steady stream of single photons.

2.1.3 Single photon emission and hexagonal boron nitride

Unlike the TMDCs, hBN is a wide bandgap insulator, making its single photon emission rather unique. It is currently theorized that point defects within hBN are responsible for emission rather than the bulk material itself, similar to defect sites in diamond or silicon carbide [83]. Much of the single photon emission from hBN occurs in the visible region (*i.e.,* photon energy ~ 2 – 3 eV) implying the existence of mid-bandgap defect centers functioning as artificial atoms [11]. A simplified bandgap diagram showing defects in hBN can be seen in **Fig. 2.3**(a). Optical phonons, which are collective oscillations in a crystal lattice, are also important to consider. Longitudinal optical phonons are of particular interest in hBN as they can also participate in carrier recombination and therefore contribute to photoluminescence spectra [84]. The crystal momentum of a photon can be modelled as

$$\rho_{\text{phonon}} = \hbar\vec{K} \tag{2.8}$$

$$\vec{K} = \frac{q\pi}{Na} \quad q = 1,2,3,\ldots \tag{2.9}$$

Here, K is the wavevector of the lattice wave which supports half-wavelength multiples of the crystal length Na [85] commonly referred to as phonon replicas. The in-plane lattice spacing of hBN is nominally 0.25 nm [86]. **Figure. 2.3**(b) shows a hypothetical emission spectrum where a zero-phonon line and several longitudinal optical phonon modes are separated by a characteristic energy ΔE, which is often useful in defect identification.

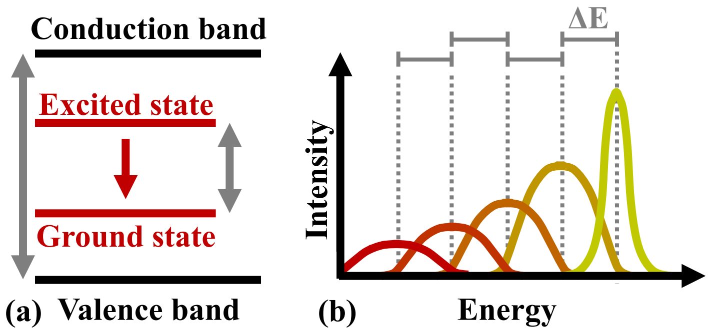

Fig. 2.3. An overview of single photon emission. **(a)** A band diagram showing an emitting defect hosted in hBN, adapted from [11]. **(b)** A simplified schematic showing a zero phonon line and longitudinal optical phonon sidebands seperated by some energy ΔE.

2.2 Thin-film optics

2.2.1 The quarter-wave stack and dielectric Bragg reflectors

Consider the alternating stack of dielectric layers shown in **Fig. 2.4**. The respective thickness of each layer is denoted as d_1 and d_2. The indices of the layers are given as n_1 and n_2 assume $n_1 > n_2$. This stack has been designed around central wavelength λ_{Bragg} such that the following relationship is true:

$$\lambda_{\text{Bragg}} = 4n_1d_1 = 4n_2d_2. \tag{2.10}$$

This specific structure is referred to as the quarter-wave stack (QWS) and possesses several interesting optical properties. The first is that reflected light (*i.e.,* from each interface in the stack) of a certain bandwidth centered around λ_{Bragg} interferes in a constructive fashion and thus the overall reflection can approach with enough layers and/or sufficient index contrast [87]. The alternating high/low index interfaces combined with the quarter-wave layers creates a phenomenon where reflected waves are in phase and constructively interfere with each other. These alternating stacks are also commonly referred to as Bragg reflectors or dielectric Bragg reflectors (DBRs) when the materials are dielectrics.

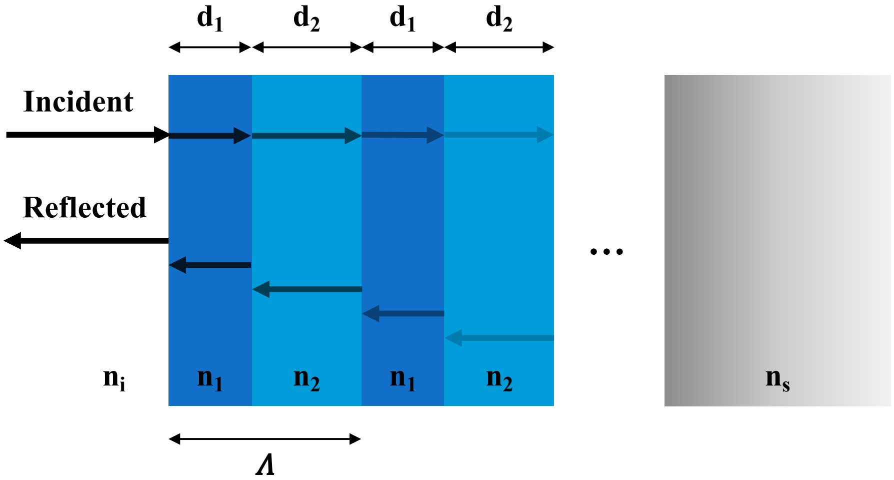

Fig. 2.4. A schematic showing alternating quarter-wave layers forming a planar Bragg mirror. The high index and low index materials are shown as dark and light blue, respectively. The repeating half-wave unit cell is denoted by $\Lambda = \mathrm{d}_1 + d_2$. Adapted from [87].

The reflectivity of a DBR depends on the refractive indices of the materials involved, denoted as n_i, n_1, n_2, and n_s, which correspond to the incident medium material, the high index material, the low index material, and the exit medium material, respectively. It is also important to distinguish between mirrors with N periods and those with $N + 1/2$ periods, the latter of which typically start and end with a high index layer. For those two cases, the peak reflectance at the Bragg wavelength can be expressed [88]:

$$R_N = \left\{ \frac{1 - \left(\frac{n_s}{n_i}\right)\left(\frac{n_2}{n_1}\right)^{2N}}{1 + \left(\frac{n_s}{n_i}\right)\left(\frac{n_2}{n_1}\right)^{2N}} \right\}^2 , \qquad R_{N+1/2} = \left\{ \frac{1 - \left(\frac{n_1}{n_i}\right)\left(\frac{n_1}{n_s}\right)\left(\frac{n_2}{n_1}\right)^{2N}}{1 + \left(\frac{n_1}{n_i}\right)\left(\frac{n_1}{n_s}\right)\left(\frac{n_2}{n_1}\right)^{2N}} \right\}^2 . \tag{2.11}$$

Referencing the equations above, it becomes clear that there are essentially two routes for maximizing reflectivity. The first is to select materials with a high index contrast, as is commonly done in the near-infrared region with amorphous silicon ($n \sim 3.7$) and silicon dioxide ($n \sim 1.46$). The second is to construct a mirror with a large number of periods from materials with lower refractive index contrast and also typically very low extinction coefficients, as was done in this work ($N = 10.5$) with tantalum pentoxide ($n \sim 2.17$) and silicon dioxide ($n \sim 1.46$).

Assuming a 'fully-formed' stopband (*i.e.,* a sufficient number of periods that peak reflectance approaches unity across the band), the bandwidth of the stopband for a given mirror depends solely on the index contrast between the high and low index layers and can be written as

$$\frac{\Delta\lambda_{\text{Bragg}}}{\lambda_{\text{Bragg}}} = \frac{4}{\pi}\arcsin\left(\frac{n_2 - n_1}{n_2 + n_1}\right). \tag{2.12}$$

Finally, it is important to note that a dielectric interface is not a hard boundary to light and that there will be a so-called penetration depth into the mirror that becomes increasingly important when designing cavities comprised of dielectric mirrors. For considerations of the distribution of energy within a mirror as well as mode volume, the so-called energy penetration depth is most relevant [89].

$$L_{\text{PEN}} = \frac{\lambda_{\text{Bragg}}}{4\tilde{n}(n_1 - n_2)}. \tag{2.13}$$

In this case, an effective medium approximation based on weighted film thickness is used to model the 'average' index of the mirror denoted by:

$$\tilde{n} = \frac{n_1 d_1 + n_2 d_2}{\Lambda}. \tag{2.14}$$

It is worth noting that the use of this effective medium approximation is most crucial for mirrors with high index contrast, and that Equation (2.13) can be simplified as $L_{\text{PEN}} = \lambda_{\text{Bragg}}/4(n_1 - n_2)$ for low index contrast mirrors.

2.2.2 Planar Fabry-Perot cavities

Considering a simple cavity formed by two mirrors with reflectivity R and radius $r \approx \infty$, separated by distance L (**Fig. 2.5**), commonly referred to as a planar Fabry Perot resonator. This model allows several quantities of interest to be obtained. First, the time a photon takes to reflect off both mirrors and return to its initial position is defined as the round-trip time $\tau_{\text{RT}} = 1/v_f$. The time constant of the photon decay rate can then be obtained by considering the reflectivity of the mirrors $\tau_p = \tau_{\text{RT}}/1 - R_1R_2$.

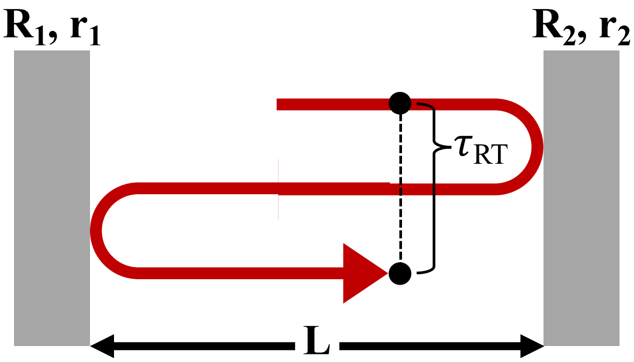

Fig. 2.5. A simple Fabry-Perot cavity of length L formed by two mirrors, each with a reflectivity R and a radius of curvature $r_{1,2} \approx \infty$. The time it takes a photon to travel the entire length of the cavity and reflect off of both mirrors is denoted as τ_{RT}.

It is also important to note that a planar cavity will support integer half-wavelength resonances of the mirror spacing nL such that $m\left(\frac{\lambda_0}{2n}\right) = L$, where $m = 1,2,3 \ldots$ represents the longitudinal mode number. The free spectral range (or spacing in wavelength between neighbouring modes) can be written as [87]:

$$\Delta\lambda_{\mathrm{FSR}} = \frac{\lambda_m^2}{nL}. \tag{2.15}$$

The reflection finesse quantifies the spectral sensitivity of a given cavity by relating the fringe spacing to the FWHM of the fringes. Finesse can also be expressed in terms of the reflectivity of the mirrors which form the cavity and can be further simplified if R_1 and R_2 are close to 1. A general expression for any high-quality-factor, low-loss resonator can then be obtained by defining the fraction of photons lost per round trip as $\mathcal{L}_{\mathrm{tot}} = 1 - R_1R_2$.

$$\mathcal{F}_{\mathrm{R}} = \frac{\Delta\lambda}{\delta\lambda} = \frac{\pi(R_1R_2)^{\frac{1}{4}}}{1-(R_1R_2)^{\frac{1}{2}}} \xrightarrow{R_1,R_2\approx 1} \mathcal{F}_{\mathrm{R}} \approx \frac{2\pi}{1-R_1R_2}. \tag{2.16}$$

However, non-idealities such as parallel deviation, spherical deviation, and surface roughness will impact the effective finesse of a mirror [90]. These effects are generally bundled into a defect finesse term $\mathcal{F}_{\mathrm{D}}$. The effective finesse $\mathcal{F}_{\mathrm{E}}$ is then the squared parallel sum of the reflection finesse and defect finesse $\mathcal{F}_{\mathrm{E}}^{-2} = \mathcal{F}_{\mathrm{R}}^{-2} + \mathcal{F}_{\mathrm{D}}^{-2}$.

One of the most important figures of merit for an optical resonator is the quality factor, which is the ratio of the energy contained within the resonator to the energy lost in one radian cycle. Quality factor can be related to finesse by Equation (2.17). It then follows that quality factor can be increased in a fixed Fabry-Perot cavity by operating at a higher order longitudinal mode m. The quality factor can also intuitively be expressed in terms of the photon decay time constant.

$$Q = m\,\mathcal{F} = 2\pi f_0 \tau_p. \tag{2.17}$$

Here, $\tau_p = \tau_{\mathrm{RT}}/1 - R_1 R_2$ is the time constant associated with the photon decay rate inside the cavity. The stability parameters for an optical cavity comprised of two mirrors can be expressed in terms of the cavity length and the mirror radii of curvature, though the full derivation relies on ABCD matrix parameters:

$$g_{1,2} = 1 - \frac{L}{r_{1,2}}. \tag{2.18}$$

The condition for stability can then be expressed as $0 \leq g_1 g_2 \leq 1$ [91]. The cavities studied in this work ranged from planar to 'half-symmetric' (*i.e.,* a positive and finite r_2). It is important to note that an ideal planar cavity will always be critically stable ($g_1 g_2 = 1$).

2.2.3 Half-symmetric Fabry-Perot cavities

Planar cavities are highly subject to misalignment due to their critically stable nature, making both fabrication and optical measurement challenging. One common workaround is to introduce a finite radius of curvature into one of the mirrors, forming what is known as a 'half-symmetric' cavity, shown in **Fig. 2.6**. A half-symmetric cavity will remain stable so long as the radius of curvature of the non-planar mirror is larger than the cavity length ($r_2 \ll L$). The introduction of a curved mirror provides optical confinement and can support a number of modal sets that satisfy the paraxial wave equation in addition to the longitudinal modes supported by the 1D cavity. The solutions of interest first require a discussion on the properties of Gaussian beams.

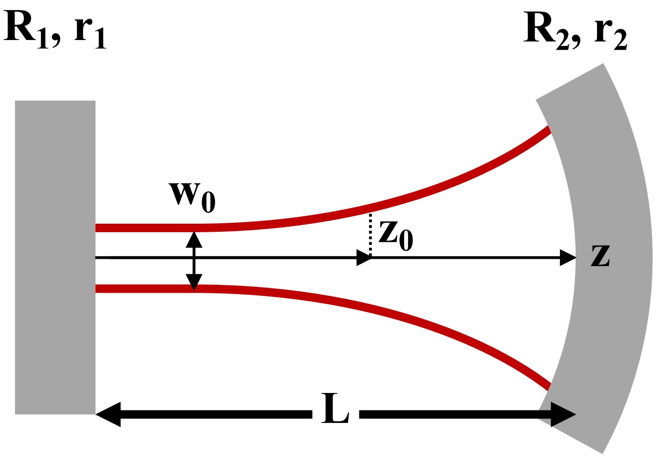

Fig. 2.6. A hypothetical half-symmetric Fabry-Perot cavity of length L formed by two mirrors, each with a reflectivity R and a radius of curvature r, where r_2 is finite. The beam waist and Rayleigh range are denoted as w_0 and z_0, respectively.

The Rayleigh range is an important property for any Gaussian beam and is defined as the distance along the optical axis, measured from the beam waist position, that it takes for the beam diameter to increase by a factor of $\sqrt{2}$ (this also corresponds to the position at which the effective area of the beam is double that at the waist). It is possible to obtain an equation for the Rayleigh range given the effective cavity length L and the radius of curvature of the non-planar mirror r_2 [91]:

$$z_0 = \sqrt{(Lr_2)\left(1 - \frac{L}{r_2}\right)}. \tag{2.19}$$

The Rayleigh range can then be used to calculate the beam waist w_0 which is the minimum radius of the beam along the axis of propagation [91]:

$$w_0 = \sqrt{\frac{\lambda z_0}{\pi}}. \tag{2.20}$$

The beam diameter at a given distance along the optical axis from the beam waist can then be calculated using the results from Equations (2.19) and (2.20). This quantity is extremely important when considering mode matching for light collection as well as pumping schemes for cavity-coupled emission.

$$w(z) = w_0\sqrt{1 + \left(\frac{\lambda z}{\pi w_0^2}\right)^2}. \tag{2.21}$$

The ratio of the beam waist and Rayleigh range can then be used to approximate an effective numerical aperture for the cavity systems studied in this work. The equation for effective numerical aperture is given as $NA_{eff} = \sin{(w_0/z_0)}$ which is also half of the total angular spread.

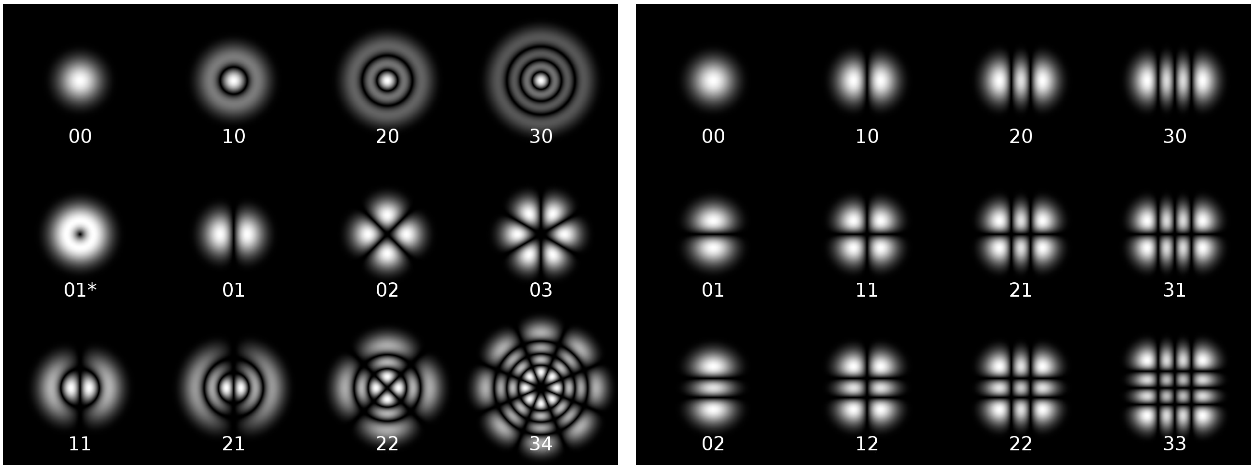

Fig. 2.7. Theoretical predictions of different Laguerre-Gaussian (left) and Hermite-Gaussian (right) modes. Adapted from [92,93].

Two of the most common sets of solutions to the paraxial wave equation are the Laguerre-Gaussian and Hermite-Gaussian modes. Some of the lower-order modes from each set can be seen in **Fig. 2.7**. Starting with the HG modes, the equation describing the electric field distribution for a given mode is written as [94]:

$$\begin{aligned} E_{l,m} = E_0 \frac{w}{w(z)} H_l\left(\frac{\sqrt{2}x}{w(z)}\right) H_m\left(\frac{\sqrt{2}y}{w(z)}\right) \\ \times exp\left[-\frac{x^2+y^2}{w^2(z)} - ik\frac{x^2+y^2}{2R(z)} - ikz + i(l+m+1)\eta\right]. \end{aligned} \tag{2.22}$$

Here, H_a is the Hermite polynomial of order a, $R(z) = (z^2 + z_0^2)/z$ is the radius of curvature of the wavefront, and $\eta = \arctan(z/z_0)$ is the phase shift on the optical axis due to the radius of curvature of the wavefront. A similar equation can be derived that describes the LG modes, though it is often presented in cylindrical coordinates due to the cylindrically symmetric nature of the LG modes [94]:

$$\begin{aligned} E_{p,l} = E_0 \frac{\sqrt{2}r}{w(z)} L_{p,l}\left(\frac{2r^2}{w^2(z)}\right) \\ \times exp\left[-\frac{r^2}{w^2(z)} \pm il\phi - ik\frac{r^2}{2R(z)} - ikz + i(2l+p+1)\eta\right]. \end{aligned} \tag{2.23}$$

Here, $L_{a,b}$ is the Laguerre polynomial of order (a, b) and r represents the radial distance in the cylindrical coordinate system rather than mirror curvature.

2.3 Cavity-enhanced emission

The theory presented in the previous two sections can now be combined in the treatment of cavity-coupled emission, where the atom can both absorb photons from the cavity modes as well as emit photons into the cavity by radiative pathways [63]. Many interesting phenomena occur when the transition frequency of the atom matches the inherently resonant modes contained within the cavity. Considering a matched system where the atomic transitions are fixed, the relative strength of the atom-cavity interaction can be expressed in terms of the photon decay rate of the cavity κ, the non-resonant decay rate γ, and the atom-photon coupling parameter g_0 (**Fig. 2.8**). The relative value of these parameters determines the time scale for the coupled system, which can either be characterized as lying in the strong coupling or weak coupling regimes.

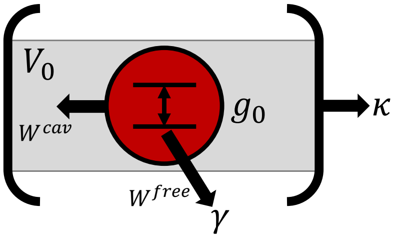

Fig. 2.8. A schematic showing cavity-coupled emission from a two-level atom. The grey box surrounding the two-level atom represents the cavity mode volume V_0. Adapted from [63].

The photon decay rate depends on the cavity quality factor and the wavelength of the corresponding cavity mode. The inverse relationship between photon decay rate and quality factor again highlights the importance of designing a cavity with a very high Q.

$$\kappa = \frac{2\pi c}{\lambda Q}. \tag{2.24}$$

The non-resonant decay rate accounts for three distinct possibilities that do not result in a photon being emitted into the resonant mode of interest. First, it is possible that a photon of the correct wavelength is emitted, but in a direction that is not suitable for cavity-coupling, as hinted at in **Fig. 2.8** Second, a photon of a non-resonant wavelength could be emitted that would not couple into a cavity mode. Third, the atom in the excited state could decay through non-radiative pathways via scattering to other states. The non-resonant decay rate can be written in terms of the Einstein coefficient A_{21} and the angle contained by the cavity mode $\Delta\Omega$.

$$\gamma = \frac{A_{21}}{2}\left(1 - \frac{\Delta\Omega}{4\pi}\right). \tag{2.25}$$

It is worth noting that the Einstein coefficient A_{21} is the rate of spontaneous emission into free space and can be written as:

$$A_{21} = W^{\text{free}} = 1/\tau_{\text{spon}} = \frac{16\pi^3\mu_{12}^2}{3\pi\varepsilon_0 h\lambda^3}. \tag{2.26}$$

Finally, the atom-cavity coupling rate can be described by the electric dipole interaction between the atom and the cavity vacuum field $\Delta E = \hbar g_0 = |\mu_{12}\varepsilon_{\text{vac}}|$. Here μ_{12} is the electric dipole matrix element of the transition and ε_{vac} is the magnitude of the vacuum field and the coupling parameter is given by [63]:

$$g_0 = \sqrt{\frac{2\pi^2 c\mu_{12}^2}{\varepsilon_0 h\lambda V_0}}. \tag{2.27}$$

2.3.1 Weak-coupling regime

The weak-coupling regime is defined as $g_0 \ll (\kappa, \gamma)$, where the time scale of the atom-cavity interaction is slower than the photon decay rate of the cavity resulting in the emission of a photon being an irreversible process. This results spontaneous decay, but with the spontaneous emission rate of the atom and the spatial/spectral characteristics of the emission being affected by the cavity. The extent of the modification of the spontaneous rate of emission can be quantified by the Purcell factor, which can be expressed as the ratio of the cavity transition rate and free space transition rate. The Purcell factor can also be written to include several nonidealities, such as electric field misalignment, spectral misalignment, and polarization misalignment [63]:

$$F_P = \frac{W^{\text{cav}}}{W^{\text{free}}} = \left(\frac{3}{4\pi^2}\right)\left(\frac{Q}{V_0/\lambda_0^3}\right)\left(\frac{|\vec{E}(\vec{r})|^2}{|\vec{E}_{\max}|^2}\right)\left(\frac{\Delta\omega_c^2}{4(\omega-\omega_c)^2 + \Delta\omega_c^2}\right)\left|\frac{\vec{p}\cdot\vec{E}(\vec{r})}{|\vec{p}|\cdot|\vec{E}(\vec{r})|}\right|^2. \tag{2.28}$$

Here $(\omega - \omega_c)$ represents the spectral misalignment between the cavity and emitter, $\vec{p}$ is the polarization orientation, and V_0 is the cavity mode volume. It is worth noting that the mode volume for the buckled microcavities discusses in this work can be approximated based on cavity length and the radius of curvature of the top mirror [95]:

$$V_0 \approx \frac{\pi}{4} w_0^2 L \approx \frac{\pi}{4} L^{3/2} r_2^{1/2}. \tag{2.29}$$

The fractional number of photons that couple into a cavity mode is described by the spontaneous emission coupling factor β, which can be written in terms of coupling rates or Purcell factor. An ideal atom-cavity system sees all its emission coupled into the cavity, leading to a β-factor of 1. Another way to look at this would be to consider the limit of β as the Purcell factor approaches infinity.

$$\beta = \frac{W^{\mathrm{cav}}}{W^{\mathrm{free}} + W^{\mathrm{cav}}} = \frac{F_P}{1 + F_P}. \tag{2.30}$$

2.3.2 Strong-coupling regime

The strong-coupling regime is defined as $g_0 \gg (\kappa, \gamma)$. The atom-photon interaction is faster than the irreversible processes involving photon loss from the cavity mode, effectively making the emission of a photon a reversible process since it can be reabsorbed before it leaves the cavity. In other words, an emitted photon can be reabsorbed by the atom faster than it is lost from the cavity mode. Operation within this regime can be described by the Jaynes-Cummings model [96], the exact details of which are beyond the scope of this thesis.

Chapter 3 – Designing and characterizing an epifluorescence spectroscopy/microscopy instrument

Because of the small, sensitive nature of measuring emission from defect centers, a specialized epifluorescence microscopy/spectroscopy system needed to be designed. This presented several non-trivial problems involving controlled pumping and efficient spectral collection. The design process regarding relevant optical elements is described below. A study of the autofluorescence properties of microscope objective lenses is also presented for the first time in the context of quantum emitters. Finally, spectral broadening in the context of Bragg mirrors is discussed.

3.1 Epifluorescence system optical design

The first step was to consider the impact of a collimator and optical fiber on the collection of spectral data. Using a simple geometric optical treatment with small-angle approximations, the magnified aperture of a fiber through a collimator lens d_{ap} can be written as

$$d_{\mathrm{ap}} \approx 2 \cdot f_{\mathrm{col}} \cdot NA. \tag{3.1}$$

Typically, the physical collimator aperture is chosen to be smaller than the that of the fiber ($d_{\mathrm{actual}} < d_{\mathrm{ap}}$) to ensure that all incident light falls within the acceptance angle or NA or the fiber. Otherwise, light incident near the edges of the collimator lens would not be accepted into the fiber. However, this can be exploited to limit both the spatial and angular FOV. The divergence angle for a collimator is determined by the ratio of the fiber core to the collimator focal length and describes the maximum accepted ray angle that will couple into the fiber. This quantity becomes increasingly important as fiber core size decreases and can be exploited to create an effective pinhole.

$$\theta_{\mathrm{col}} \approx \frac{d_{\mathrm{core}}}{2 \cdot f_{\mathrm{col}}}. \tag{3.2}$$

Next, the impact of the microscope objective used for both pumping and collection needs to be considered. For this calculation, we made the approximation that we were trying to capture uniform, isotropic emission. In this case, the diameter of the collimated beam exiting the objective relies solely on the focal length f_{obj} and numerical aperture NA_{obj} of the objective:

$$d_{\mathrm{obj}}^{\mathrm{iso}} = 2 \cdot f_{\mathrm{obj}} \cdot NA_{\mathrm{obj}}. \tag{3.3}$$

It is important to note that this is not the case when imaging a laser beam since the reflected beam has a tighter angular spread than the objective, as well as a gaussian intensity profile. In this case, the diameter of the beam exiting the objective can be roughly estimated by substituting the objective numerical aperture for the half-angle divergence $\theta_{\mathrm{D}}^{\mathrm{laser}}$ characteristic to a particular laser:

$$d_{\mathrm{obj}}^{\mathrm{laser}} \approx 2 \cdot f_{\mathrm{obj}} \cdot \theta_{\mathrm{D}}^{\mathrm{laser}}. \tag{3.4}$$

Finally, the effective collection ROI (and therefore FOV) on the sample can be determined by assuming that the ROI divergence angle θ_{ROI} is matched to the collimator divergence angle:

$$\theta_{\mathrm{ROI}} = \arctan\left(\frac{\mathrm{ROI}}{\mathrm{EFL}}\right) \Rightarrow \mathrm{ROI} \approx \tan\left(\theta_{\mathrm{col}}\right) \cdot \mathrm{EFL}. \tag{3.5}$$

Using the equations described above, a series of optical fibers can be selected that cover a wide range FOVs in combination with a Thorlabs F810FC-635 collimator (NA = 0.25, $f_{\mathrm{col}} = 35.41$ mm). **Table 3.1** provides examples of FOVs that can be obtained with different multimode fibers for the 0.9 NA 100x objective used in this work.

Table 3.1. Optical fiber selection and the resulting sample FOV with a 100x objective (EFL $\approx 1.6\ mm$)

Optical Fiber	θ_{col}	d_{obj}	FOV diameter
50 µm core (FG050LGA)	1.44 mrad	2.88 mm	4.6 µm
200 µm core (FG200UEA)[a]	5.76 mrad	2.88 mm	18.4 µm
600 µm core (FP600URT)	17.27 mrad	2.88 mm	55.3 µm

[a] Example fiber that theoretically could be used for this work.

The epifluorescence system described here ultimately relies on a small core fiber acting as a pinhole to set the FOV through a high-magnification objective. This allowed for the measurement of individual sites while blocking unwanted background emission. Further detail regarding the exact optical components used is given in the coming sections. It is also worth noting that the mechanical stability of the system and its quasi-confocal nature can become an issue when using a shallow depth of focus (high magnification) objective combined with a fiber pinhole, and that manual adjustment often was required to remain focused on the same plane.

3.2 Accounting for objective lens autofluorescence in quantum emitter measurements

3.2.1 Introduction and motivation

The recent increase of interest in quantum emitters in 2D materials such as transition metal dichalcogenides (TMDCs) [97] and hexagonal boron nitride (hBN) [11,98] has prompted many to construct homebuilt optical systems often targeting photoluminescence microscopy/spectrometry as a particularly important measurement. Single photon emission (SPE) from such materials has a broad range of potential applications in quantum cryptography, communication, and computing [82]. However, because of the small-signal nature of many emitting materials, it is often a challenge to locate and correct for background fluorescence within a setup. The pieced-together nature of a homebuilt system adds an additional layer of complexity. In this short report, we show that microscope objectives, even those specifically designed for fluorescence applications, can be a significant source of background signal within many epifluorescence setups. The issue of "autofluorescence" within objectives has been widely studied in the context of fluorescence imaging [99–101], where it is typically treated as background noise that interferes with high contrast measurements. However, there is minimal discussion in the literature with respect to the spectral properties of this autofluorescence, which in the context of quantum emitters can be viewed as a ubiquitous and characteristic source of system noise. Moreover, when considering small-signal spectral measurements common in experiments involving SPEs, such background signals can be on the same order of magnitude as that from the sample. Thus, it is critically important to characterize and remove this background autofluorescence from any photoluminescence measurement of quantum emitters.

3.2.2 Results and discussion

Figure 3.1 shows a comparison of fluorescence obtained from various microscope objectives (**Table 3.2**) using a 405 nm CW laser (Pangolin LDX-405NM-200MW) as an excitation source. Each spectrum is representative of a time-stable system autofluorescence that appears to depend on the objective lens used. Some of the spectra contain sharp lines while others exhibit only broad background features. The data presented is as measured (*i.e.,* no averaging or post-processing) so that the amplitude of each spectrum can be directly compared. These measurements were taken using the homebuilt quasi-confocal photoluminescence spectrometry setup shown in **Fig. 3.2**. This system was designed to measure defect-center emission from hBN, which spans a wide range of visible and near-infrared wavelengths (~ 500 nm – 850 nm) [11].

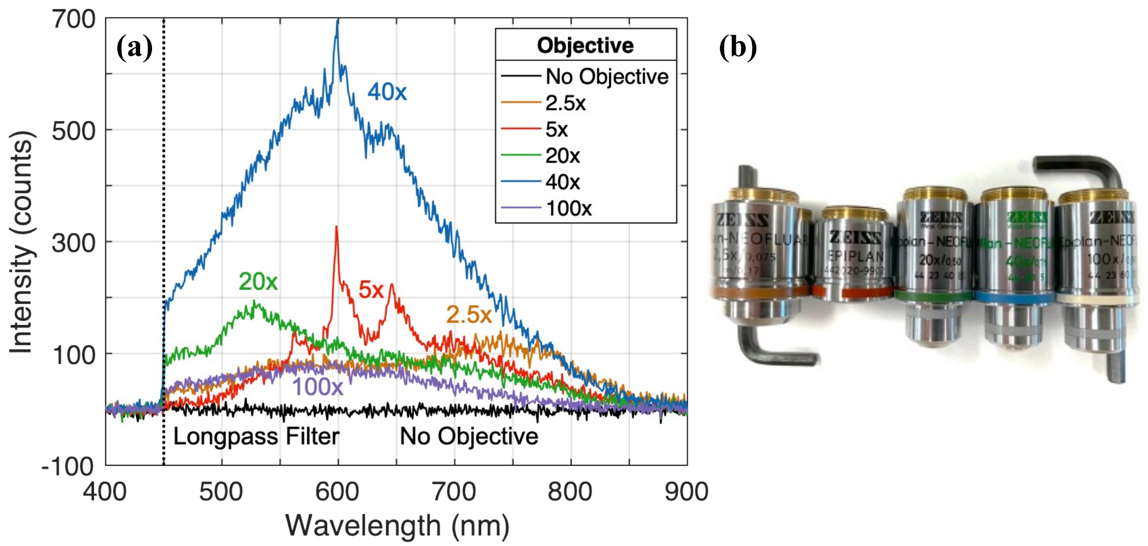

Fig. 3.1. Photoluminescence from microscope objectives. **(a)** Representative photoluminescence signals for various objective lenses (Table 1) under 20 mW of 405 nm CW excitation. The sharp cut-off at 450 nm is due to the presence of a long pass filter in the collection path. **(b)** A photograph of the objectives studied.

Table 3.2. A list of the infinity-corrected Zeiss microscope objectives studied.

Magnification	*Numerical Aperture*	*Objective*[a]
2.5x	0.085	Zeiss EC Plan-Neofluar
5x	0.13	Zeiss Epiplan
20x	0.5	Zeiss Epiplan-Neofluar
40x	0.75	Zeiss Epiplan-Neofluar
100x	0.9	Zeiss Epiplan-Neofluar

[a] Although the objectives are not all from the same series, they are all listed as photoluminescence-grade by the manufacturer.

As with any fluorescence measurement, one primary goal is to efficiently deliver the pump light to the desired region of the sample, while eliminating (as much as possible) its presence in the detection path. To that end, the excitation source was first sent through a neutral density filter (Newport FBS series) and an adjustable iris for attenuation and spatial filtering, then passed through a 450 nm cut-off short pass filter and a 468 nm cut-off short pass filter (Thorlabs FESH0450 and Semrock FF01-468, respectively). The filtered pump beam was reflected by a dichroic mirror (Thorlabs DMLP425R) towards the objective under test. In a typical measurement of a sample placed at the focus of the objective, some of the light emitted by the sample is collected back into the objective lens and then passed upwards through the dichroic mirror. To illustrate the role of microscope objective autofluorescence as a potential source of noise, we replaced the sample with an angled silver mirror. This mirror was located at a large distance (~ 10 cm) below the objective to minimize the possibility of scattered/reflected light coupling back into the system while also ensuring that it did not sit at the focal plane of any objective, so that potential luminescence from any surface debris was not collected. The collection side of the system (above the dichroic) was configured in the same way as it would be for typical fluorescence measurements. The collection path contained a 450 nm cut-off long pass filter (Thorlabs FELH0450) to further remove residual pump photons. The filtered light was delivered to a 90:10 beamsplitter (Thorlabs BS025); a CMOS camera (Thorlabs CS895MU) received 10% of the split beam, while the remaining 90% was sent towards a 50 µm-core pickup fiber (Thorlabs FG050LGA) mounted to a 34.74 mm focal length fiber collimator (Thorlabs F810FC-543). The output of the fiber was coupled directly into a USB spectrometer (Ocean Optics QE Pro) configured with a 25 µm slit.

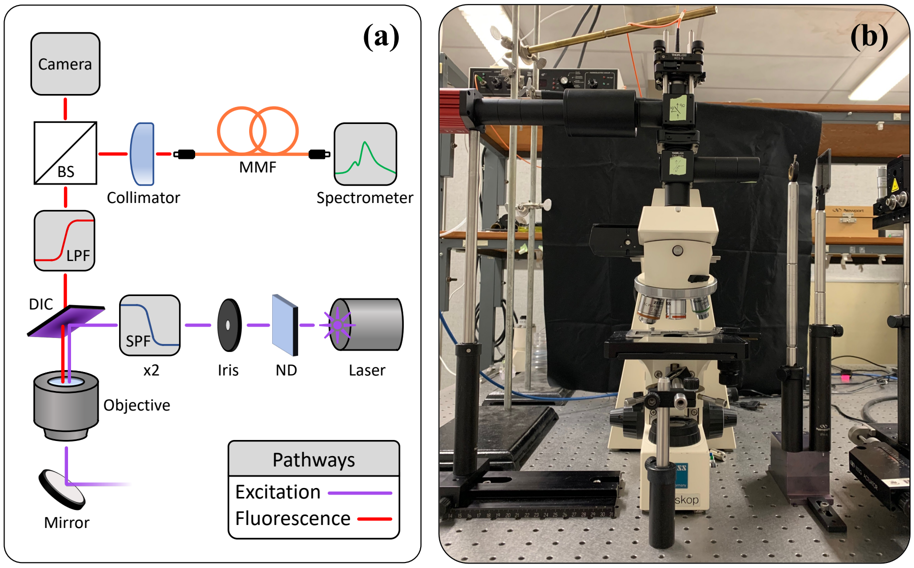

Fig. 3.2. Experimental setup. **(a)** A schematic of the experimental setup used to perform photoluminescence measurements with no sample in place. An angled silver mirror was placed far below the focal plane of the objective lens to minimize collection of back-scattered pump photons. (Legend: DIC – dichroic mirror, ND – neutral density filter, BS – beamsplitter, MMF – multimode fiber, SPF/LPF – short-pass/long-pass filter). **(b)** A photograph of the experimental setup.

To investigate the variation of autofluorescence signal with pump power, we collected spectra for pump powers in the 2 mW ~ 50 mW range using the 5x objective lens. The 5x lens was selected because of its particularly sharp spectral features. **Fig. 3.3**(a) shows the evolution of fluorescence spectra for varying pump laser power. The relationship between pump power and the fluorescence signal power is given in the inset of **Fig. 3.3** (a), where the reported fluorescence signal power is integrated over all wavelengths. A linear fit to this data revealed a slope of 163 ± 1 counts s^{-1} mW^{-1} with $R^2 = 0.9985$. While the collected power is system-dependent, the linear relationship between the fluorescence and illumination ($I_{flu} \propto I_i$) is evidence of emission below saturation [102].

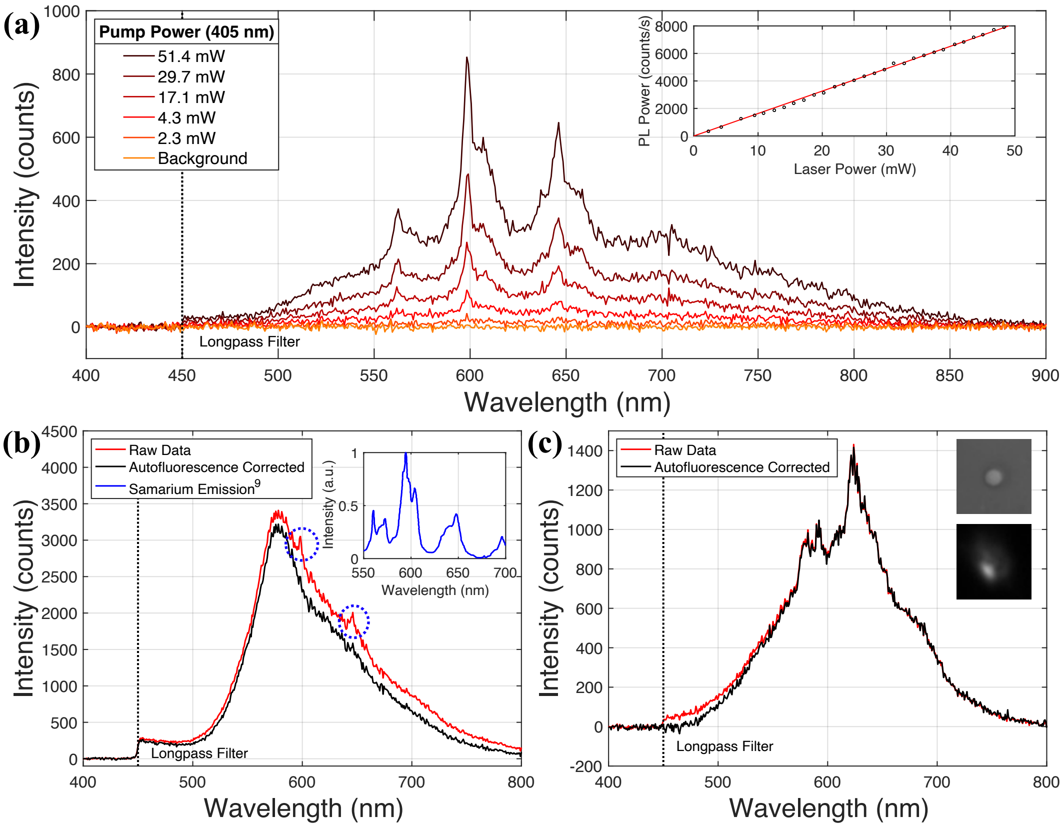

Fig. 3.3. (a) Effect of pump power on photoluminescence spectrum for the 5x objective from Table 1. The laser pump power incident on the objective was adjusted as the resulting photoluminescence signal was collected at each step. The inset shows pump laser power versus photoluminescence power for the same objective (black circles). Photoluminescence power was obtained by integrating over the detection range for each spectrum. An approximately linear relationship (red line) was observed, with a slope of 163 ± 1 counts s^{-1} mW^{-1}. **(b)** Photoluminescence obtained from an ensemble of hBN emitters with (black) and without (red) autofluorescence correction applied captured using the 5x objective (Table I) with ~ 20 mW of pump power. Blue circles contain peaks likely corresponding to objective lens autofluorescence. The inset shows an extracted photoluminescence measurement (blue) obtained from samarium defects in natural fluorite excited with a 400 nm pump. The data contained in the inset has been reproduced with permission from

Phys. and Chem. of Minerals 30, 8 (2003). Copyright 2003, Springer Nature [103]. **(c)** Photoluminescence obtained from an ensemble of hBN emitters with (black) and without (red) autofluorescence correction applied captured using the 100x objective (Table 1) with ~ 3 mW of pump power. The inset shows BF and PL images of the corresponding hBN-coated region, which was a ~ 3.6 μm SiO_2 pillar in this case.

As is clear from **Fig. 3.1**, even with no sample of any kind present, spectra intrinsic to the experimental setup are observed and appear to be unique to each objective lens. In all cases, the emission extends from < 450 nm to ~ 850 nm, and in some cases contains sharp, distinct spectral features. The most likely sources of this apparent emissive property of the objective lens, and specifically the sharp emission lines centered at ~ 600 nm produced by the 5x and 40x objectives, are defects and impurities within the objective glass itself. Fluorite glass, among many others, has long been known to contain luminescing defects [104–106]. Most of the Zeiss objective lenses used in this study contain fluorite, though the exact compositional breakdown is not provided by the manufacturer. It is well known that fluorite and other host materials contain dopants/impurities such as Sm^{3+}, Dy^{3+} and Eu^{3+} which have atomic transitions near 600 nm [103,107–110]. For example, L-band excitation (~ 400 nm) of fluorite and crown glass containing Sm^{3+} produce emission spectra [103,110] that almost exactly match that observed from the 5x and 40x objectives lenses in this study (*i.e.,* compare **Fig. 3.3**(a) and the inset of **Fig. 3.3**(b)). Sharp emission lines in this range have significant potential to interfere with those of SPEs hosted by hBN [11] and other materials, a fact which has not been widely discussed in the context of quantum emitters. To add to the confusion, one of the hallmarks of single photon emission in hBN is the energy spacing between a narrow zero phonon line and a broader phonon sideband (ΔE ~ 160 meV or ~ 50 nm) [98]. Some of the data from the 5x and 40x objectives could easily be mistaken for such features. For example, consider the sharp feature near 650 nm and broad feature centered about 700 nm in **Fig. 3.3**(a). To demonstrate this point, we have included an emission spectrum from a continuous hBN film (Graphene Supermarkets CVD-2X1-BN-ML) that was transferred to an SiO_2 substrate using a polymer-assisted transfer process [57]. An ensemble of emitters measured using the 5x objective is shown in **Fig. 3.3**(b). The raw, uncorrected spectrum (red) contains the same interference signals (circled blue) present in **Fig. 3.3**(a) that we attribute to the objective lens. Performing a background subtraction with no sample (black) using the spectra in **Fig. 3.3**(a) almost entirely removes these features while leaving other spectral content undisturbed. If not accounted for, such autofluorescence signals have potential to obscure the identification of single photon emitters. However, with proper alignment and high collection efficiency this background autofluorescence can be reduced to a relatively innocuous level, for example as shown in **Fig. 3.3**(c), where an ensemble of emitters was measured using the 100x objective.

The fact that each objective has a unique emissive characteristic is likely owed to a combination of effects involving their differing physical construction (*i.e.,* size, material composition) and optical properties (*i.e.,* working distance, numerical aperture) further complicating the process of identifying, tracking, and calibrating for this autofluorescence. In addition, other optical components within the epifluorescence system such as the dichroic mirror, beamsplitter, and fiber pinhole have potential to further colour the collected spectra. Photoluminescence measurements of the objective lenses in isolation are presented in Appendix A to demonstrate this point.

We are confident in stating that laser non-idealities are not the source of the signals we observed here. Multi-stage input filtering was used to suppress spectral content above ~ 450 nm wavelength prior to the beam entering the objective turret. The effectiveness of this filtering was verified by addition of extra short-pass excitation filters, confirming that this had no impact on the measured spectra above. Furthermore, we found that replacing the objective under test with a silver mirror eliminated the photoluminescence signal, as shown in **Fig. 3.1**, providing additional evidence that the photoluminescence spectra shown are attributable to emission by the objective lenses.

3.2.3 Conclusion

In summary, we have demonstrated that background fluorescence from microscope objective lenses can be a potentially problematic source of interference in the context of quantum emitters. Certain materials like samarium contained within objective lens glass might produce sharp emission lines which can easily be mistaken for defect-based emission. For the epifluorescence system described here, this autofluorescence approaches the order of 10^2 counts/second. The important message is that researchers need to be mindful of all materials contained within the beam path of their photoluminescence systems when measuring small signals. Performing a system characterization as shown in **Fig. 3.2** may yield concerning but nonetheless necessary results.

3.3 Spectral broadening

While epifluorescence microscope systems are commonplace for measuring emission from relatively isotropic, uncoupled quantum emitters, such systems are problematic when Bragg mirrors come into play. First, consider that the (half-symmetric) cavity modes studied in this work are highly directional but also divergent. This makes collection increasingly challenging as distance from the sample increases, which is often the case for low-NA objective lens. The second problem has to do with planar cavities formed between the regions containing buckled domes on samples. Since both mirrors have a theoretical infinite radius of curvature, they will form a critically stable resonator at any cavity length since $g_{1,2} = 1$. This essentially means that light is free to walk across the mirrors on reflection and accrue an angle while doing so. The angular dependence of this type of cavity means that the collected spectrum is dependent on the numerical aperture or acceptance angle of the instrument used to collect the light. **Figure 3.4** shows an example of this effect, where a series of objective lenses were used to collect reflected light from a planar cavity. A simple microscope illuminator was used as the source and each spectrum was normalized against source reflection plots collected with a silver mirror. A planar cavity mode is clearly contained within the mirror stop band when collecting using a 5x objective with an NA of 0.13, as evident by the dip in reflection near 560 nm. This feature is washed out when higher magnification, and therefore higher NA objectives are used due to the angular dependence of the DBR structure. This type of planar cavity is often present in the areas between buckled half-symmetric cavities and can obscure cavity modes. For these reasons, it was determined that the previously discussed quasi-confocal microscopy/spectroscopy station was not well-suited for studying the buckled dome microcavities fabricated by the DeCorby group. Photoluminescence measurements proved particularly problematic due to the high NA of the objective lenses used, which often led to light collection outside the area of interest (*i.e.,* the cavity mode). This discovery meant that other methods of obtaining reflection and fluorescence measurements of cavity modes needed to be devised, the exact details of which will be explored in the coming chapters.

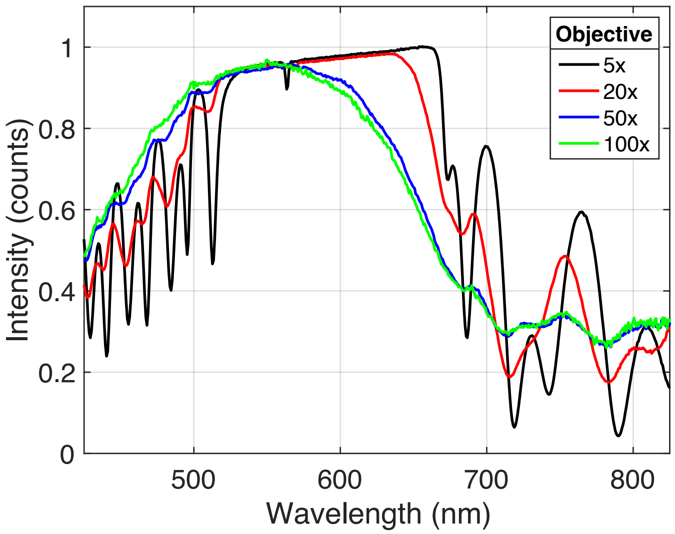

Fig. 3.4. Normalized reflection plots illustrating the effect of increasing numerical aperture for a planar cavity formed by two asymmetrical Bragg mirrors. Plots were obtained using a microscope illuminator source and Ocean Optics QEPro spectrometer.

Chapter 4 – A polymer transfer technique for strain-activated emission in hexagonal boron nitride

We present a hexagonal boron nitride (hBN) polymer-assisted transfer technique and discuss subtleties about the process. We then demonstrate localized emission from strained regions of the film draped over features on a prepatterned substrate. Notably, we provide insight into the brightness distribution of these emitters and show that the brightest emission is clearly localized to the underlying substrate features rather than unintentional wrinkles present in the hBN film. Our results aid in the current discussion surrounding scalability of single photon emitter arrays.

4.1 Introduction

The single photon emitter (SPE) is a device crucial to the development of many emerging technologies in the areas of quantum metrology, quantum computing, and quantum information, with continuous-variable quantum key distribution being a noteworthy application [11,55,111]. There have been many proposed material platforms for SPEs, including carbon nanotubes [112], quantum dots [113], diamond nitrogen vacancy centers [114], trapped calcium ions [115], transition metal dichalcogenides (TMDCs) [26], and more recently, defect centers in hexagonal boron nitride (hBN) [43,116]. Among these materials, hBN has emerged as one of the most promising [11,24,55].

Much of the popularity of hBN is due to (a) its bright emission, (b) the room-temperature operation of its SPEs, and (c) its ability to withstand aggressive fabrication techniques. SPEs in hBN also possess good photostability (though not a unique property) and high quantum efficiency [55,117,118], in-plane linearly polarized emission [56], and optically addressable spin states [119,120]. The optical transition energies corresponding to defect-originated emission are typically embedded deep within the bandgap, meaning that zero phonon lines are detectable above the ambient thermal noise floor without cryogenic cooling [30]. The exact origin of defect emission in hBN is still a point of discussion, with several proposed models circulating [43,55]. Recently, however, there have been significant advances including the discovery of mechanically decoupled electronic transitions in some defect centers [121], quantum emission from the $N_B V_N$ nitrogen-boron substitution in which a neighbouring nitrogen atom is missing [122], and unique spin properties from the V_B^- defect [123,124]. The rapid pace of such advances means that the origins of defect-based emission within hBN are becoming increasingly well understood. Reliable fabrication techniques at the wafer-scale will soon be in demand as progress is made towards device implementation rather than first principle investigations.

While emission from hBN has been studied using mechanically exfoliated flakes prepared in the style of graphene [116,125,126], investigations involving thin, continuous films have been rising in popularity. There has already been some success in devising methods of polymer-assisted thin film transfer for hBN as well as many of the TMDCs [24,127]. Such transfer methods are scalable and therefore highly suited for integration with existing silicon-based technology such as waveguides, microdisks, and optical cavities. In the case of hBN, wet transfer methods provide the potential for the deterministic activation of defect-based emitters by introducing strain on the crystal lattice [24,43,128]. While the outlines of several proposed hBN thin film schemes have surfaced [129,130], none so far have provided a fully detailed process flow. This is problematic since such transfer processes involve many non-trivial steps. Additionally, studies are typically more concerned with small-scale transfers, rather than a scalable process useful for integrated devices [24,127].

One promising way to construct arrays of SPEs is to drape a thin hBN film over nanostructures patterned on a silicon substrate, as demonstrated by Proscia *et al.* in their modified wet transfer technique [24]. They theorized that charge carrier trapping occurs near the regions with highest strain, causing defect centers to function as potential wells. More recently, work by Li *et. al.* has disputed the role of strain in hBN defect emitter activation. Rather, they reported localized single photon emission only from hBN films deposited directly via CVD onto prepatterned substrates [129]. The conflict between these findings leaves this important topic openly debated in the current literature. Our contribution to this discussion is two-part. First, we present an hBN transfer process flow and describe common problems one might encounter. Then, using this method, we transfer hBN films to a substrate containing nanoscale-height features and verify that the brightest emission is localized to the underlying features rather than unintentional wrinkles.

4.2 The hBN transfer process

We began by fabricating pillar-patterned substrates from SiO_2 which were eventually used as the target substrates for our hBN transfer. The details of this process can be found in Supplement 1.

The first step in our transfer process was to cut ~20 nm thick CVD-grown multilayer hBN/Cu foil (Graphene Supermarket CVD-2X1-BN-ML) into ~1 cm by ~1 cm squares using scissors cleaned with isopropyl alcohol. The squares were individually coated with 950K molecular weight PMMA using a Brewer spinner/hotplate combo. Note that a sanitized miniature gasket seal was used to hold the foil in place on the substrate vacuum. The spin settings were 10 seconds at 100 RPM for the spread step and 40 seconds at 2200 RPM for the spin step. The coated films were then immediately transferred to a 180° C hotplate for 120 seconds to bake the resist. A schematic representation of the device at this point in the process is shown in the first step of **Fig. 4.1**.

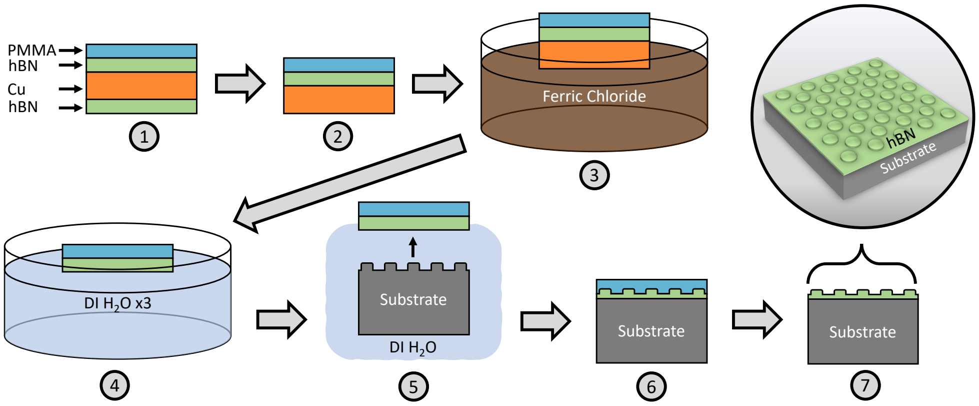

Fig. 4.1. A visualization of the hBN transfer process. PMMA is spun onto CVD hBN/Cu in step 1. The backside hBN is roughened in step 2, followed by a ferric chloride etch to remove the copper in step 3. The film is cleaned and lifted from solution using a target substrate in steps 4-6, followed by removal of the PMMA layer in step 7. The hBN film conforms to the substrate surface topology during the transfer process.

It is important to remove the exposed hBN film on the side of the foil opposite the PMMA, so that ferric chloride etchant used in subsequent steps comes into direct contact with the copper. We found that hBN is somewhat resistant to the ferric chloride, and that islands of copper can become encapsulated between hBN layers, resulting in gaps in the final devices as well as long etching times that could otherwise be avoided. We have had success roughening the exposed hBN film using an aggressive O_2 plasma etch in a reactive ion etching (RIE) system. Exact etching parameters are given in Table 1. The samples were placed PMMA-side down in the processing chamber without worry of damaging the target hBN film, which was sandwiched between copper and PMMA layers (step 2 in **Fig. 4.1**).

Table 4.1. Etching parameters for backside hBN roughening.

Recipe	O_2 Flow Rate	Power	Time	Temperature	Pressure
O_2 Strip	50 sccm	200 W	2 min	20 ℃	100 mTorr

Next, the films were floated copper side down via surface tension on a room-temperature ferric chloride bath (MG Chemicals 415) to etch the copper (step 3 in **Fig. 4.1**). It was crucial for the film to remain floating on the surface of the solution. We noted that if the film became submerged, it was difficult to transfer between baths. Additionally, the orientation of the film could easily change, making it difficult to determine which side was PMMA-coated. Once all the copper had been etched, leaving a transparent hBN/PMMA film (endpoint determined visually, ~24 hours), the films were lifted from the surface of the etchant using a quartered Si wafer piece held with wafer tweezers, which were rinsed between each step. The films were immediately transferred between three sets of deionized water beakers in an attempt to dilute any leftover ferric chloride, again being careful to 'float' the films on the surface (step 4 in **Fig. 4.1**). Finally, the films were lifted from the final deionized water bath using piranha-cleaned pillar-patterned substrates (step 5 in **Fig. 4.1**) and allowed to dry overnight (step 6 in **Fig. 4.1**). It was important to allow the devices to dry before continuing, otherwise excess moisture trapped between the substrate and hBN film boiled out in following steps, resulting in areas where the hBN appears to be missing. Water between layers also negatively impacts transfer success rate, resulting in "patches" of hBN being lifted away in later wet processing steps. Drying or cleaning with pressurized nitrogen gas was avoided since the hBN/PMMA films could be blown off of the substrate.

Before removing the PMMA layer, each chip was heated to 200 °C using a hotplate to remove any trapped gas between the hBN and underlying substrate. This has been shown to lead to better film conformity [24]. Heating at this point in the process flow did not damage the hBN film since the hBN/substrate interface was dry. Annealing times ranging from 10 min to 30 min were tested based on current literature [24,48]. However, there was no discernable difference in film conformity between devices annealed for different times. The devices were then placed in room-temperature acetone overnight to remove the PMMA layer before being submerged in IPA, rinsed with DI water, and allowed to dry (step 7 in **Fig. 4.1**).

The method described above produced ~80% successful transfer, measured by area in the regions where contact was initially made between the hBN and substrate. A typical final transfer product can be observed on a large scale in **Fig. 4.2**(a). Most imperfections were located near the edges of the transferred films. These results have been verified over multiple trials, with the expectation that even higher yield is possible through additional process refinement such as further dilution of the leftover ferric chloride or a more delicate way of transferring the thin film stack between baths. **Figure 4.2**(b) shows an optical microscope image of a 1 mm by 1 mm unit cell that has been successfully transferred, while **Fig. 4.2**(c) shows the edge of the transferred film. More hBN coated unit cells representing an entire transfer can be seen in **Fig. B.4** in Appendix B. All prepatterned substrates were fabricated from a thermally oxidized wafer (Appendix B) and features ranged in height from 150 nm to 170 nm. It should be noted that our transfers were done using 1 cm by 1 cm substrates, though the technique could be scaled up for single transfers to entire wafers, with the limiting factor being the availability of appropriately sized CVD hBN on copper foil. Additionally, only one brief device heating step is required during the process, leaving plenty of room in the thermal budget of silicon for additional processing steps.

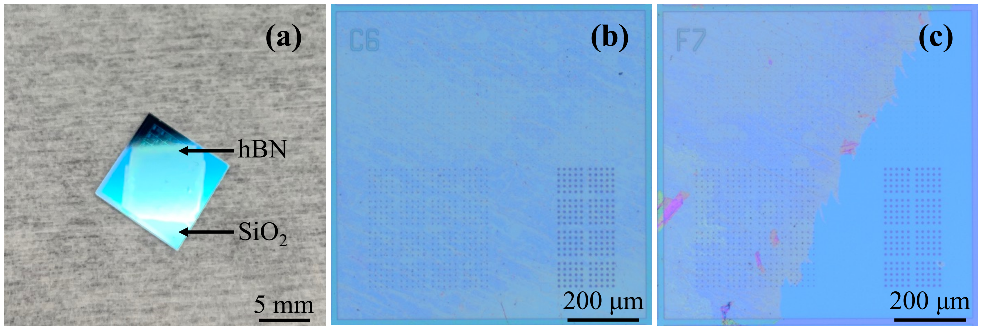

Fig. 4.2. Images of the hBN transfer process product. **(a)** A photograph of a 1 cm by 1 cm substrate coated with hBN. **(b)** A microscope image of a 1 mm by 1 mm unit cell completely coated with hBN. **(c)** A unit cell from the same wafer that contains the edge of the transferred film. Note that the areas near the edge of the hBN film have more defects compared to the interior region.

Figure 4.3 shows an array of images taken with a scanning electron microscope (SEM). It is important to note that discontinuities and edges were specifically presented to provide contrast between coated and uncoated regions. These images clearly show the film making contact with the structures before bending back in contact with the substrate, such as in **Fig. 4.3**(e), where the edge of a film falls on a bullseye structure.

It also appears that wrinkles in the film were transferred to the SiO_2 substrate. This is visible in **Fig. 4.3**(a) and **Fig. 4.3**(d) as lines that run diagonal to the array of pillars, as well as in **Fig. 4.3**(c) where a wrinkle crosses over a pillar. Some have theorized that these "natural wrinkles" are formed during the hBN CVD growth process rather than the transfer process [24], though we were unable to verify this claim. In similar hBN transfer methods, others noted that nanopillars over certain heights (>155 nm) resulted in "piercing" of the hBN film [24,129]. Piercing was not observed in our devices which typically ranged from 150 nm to 170 nm in height. We believe that this was due to the decreased aspect ratio of our micro/nanostructures, which were not patterned with electron beam lithography.

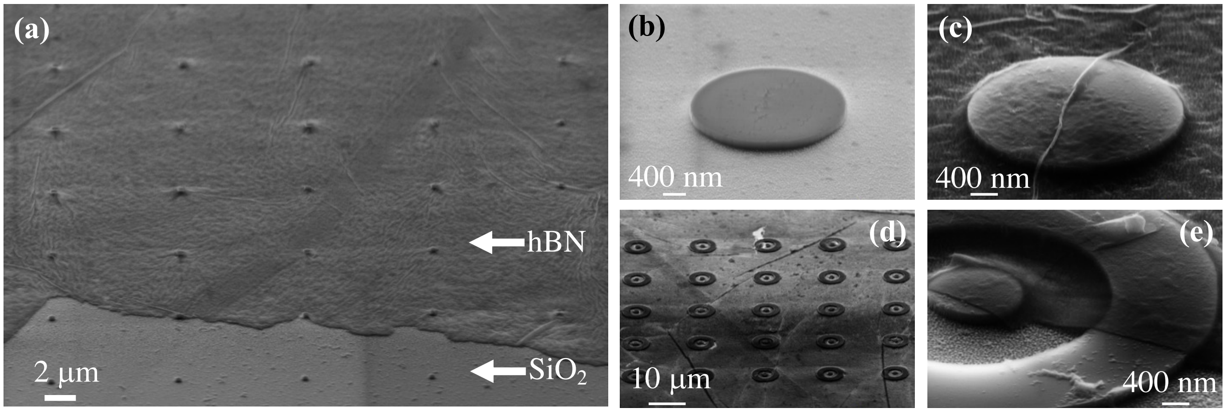

Fig. 4.3. Scanning electron microscope images of transfers to various structures. **(a)** An array of ~0.6 μm diameter pillars near the hBN film edge. **(b)** An uncoated ~2 μm pillar. **(c)** A coated ~2 μm pillar with a wrinkle. **(d)** An array of coated bullseyes clearly showing varying layer thickness and so called "natural wrinkles", and a missing patch above the middle bullseye in the top row. **(e)** An hBN film conforming to the topology of a bullseye feature.

The method presented is highly suited for integration with optical cavities because of the potential to position defects at resonant antinodes paired with the robustness of hBN. However, the etched surface of the substrate appears to be somewhat rougher than the top surface which could affect optical quality. Other etching techniques, such as a buffered oxide etch could be used to improve uniformity, while still preserving the sharp edges of mask features. The topic of surface roughness characterization is left for future work. A flowchart showing the entire transfer process can be seen in **Fig. B.6**. The flowchart contains variations of the optimized process described here as well as dead ends and potential pitfalls.

4.3 Optical results and discussion

All photoluminescence images and spectra were obtained using a modified Zeiss Axioscope, as shown in **Fig. 4.4**. The excitation source was a 405 nm Pangolin laser (LDX-

405NM-200MW) aligned to a pinhole. The beam was then passed through a 450 nm short pass filter and a 468 nm short pass filter (Thorlabs FESH0450 and Semrock FF01-468, respectively). The filtered pump beam was reflected off of a dichroic mirror (Thorlabs DMLP425R) towards an infinity-corrected objective, ranging in magnification from 5x to 100x. Measurement of individual sites was performed with a 0.9 NA 100x objective lens (Zeiss EC Epiplan) and ~4 mW of laser power incident on the sample. Light from the sample was then collected through the same objective and passed through the dichroic mirror. A subsequent 450 nm long pass filter (Thorlabs FELH0450) was used at the input of a 90:10 beamsplitter (Thorlabs BS025) to remove pump light. The collected light was split between an 8.9 MP CMOS camera (Thorlabs CS895MU) and a 50 μm core pickup fiber (Thorlabs FG050LGA). The fiber was mounted to a FC/PC collimator with a focal length of 34.74 mm (Thorlabs F810FC-543) at the 90% terminal of the beamsplitter. The output of the fiber was coupled directly into an Ocean Optics USB 4000 visible range portable spectrometer. The integration time on the spectrometer was typically set to the maximum value of 10 seconds. This put a clear limitation on the achievable signal-to-noise ratio, as well as the minimum resolvable signal. The relatively small core size of the pickup fiber functioned as a pinhole, limiting the FOV seen by the spectrometer to a ~ 5 μm window on the sample. The experimental setup prohibited the study of individual SPEs, which will be the subject of future work. The focus of the following study was to verify that the brightest hBN emission is localized to the underlying features of a target substrate.

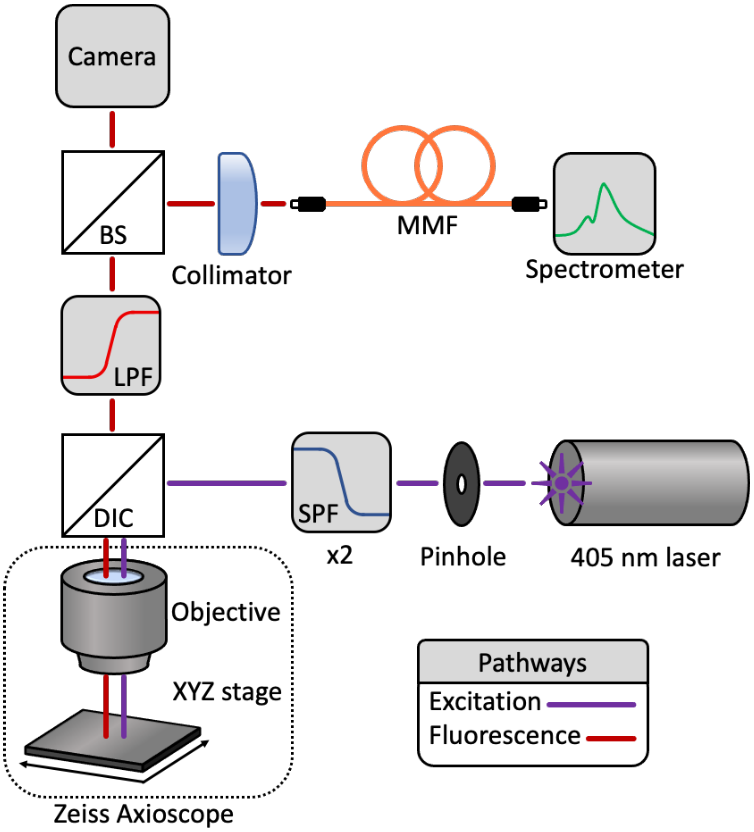

Fig. 4.4. A schematic of the setup used to perform photoluminescence measurements. Where DIC stands for dichroic mirror, BS stands for beamsplitter, MMF stands for multimode fiber, and SPF/LPF stand for short pass filter and long pass filter, respectively. The components enclosed by a dotted outline were built into a Zeiss Axioscope that was used as a starting point for the setup.

Wide-field photoluminescence (PL) images of hBN-coated nanostructures are shown in **Fig. 4.5**. The entire FOV was illuminated by aligning the pump laser to the sample at a glancing angle with an irradiance of ~ 0.2 W/cm^2. Camera images were collected using a 10 second integration time. The large dark strip near the top right corner of the PL image shows an area where the hBN transfer failed, leaving the SiO_2 underneath exposed. As expected, there is little emission in this area, except for trace amounts of hBN that were left behind when the bulk of the film was ripped away. The area containing a defect in the hBN transfer was specifically chosen so that a control region would be present in the image. Additionally, there are many bright lines running horizontally across the coated areas in the PL image, which could either be an artifact of the CVD growth process or regions of the film that were strained as they came into contact with rough areas of the substrate during the transfer process. These results clearly show that the hBN emission is highly correlated to the underlying structures, as verified by the corresponding bright field (BF) image shown in the insets of **Fig. 4.5**.

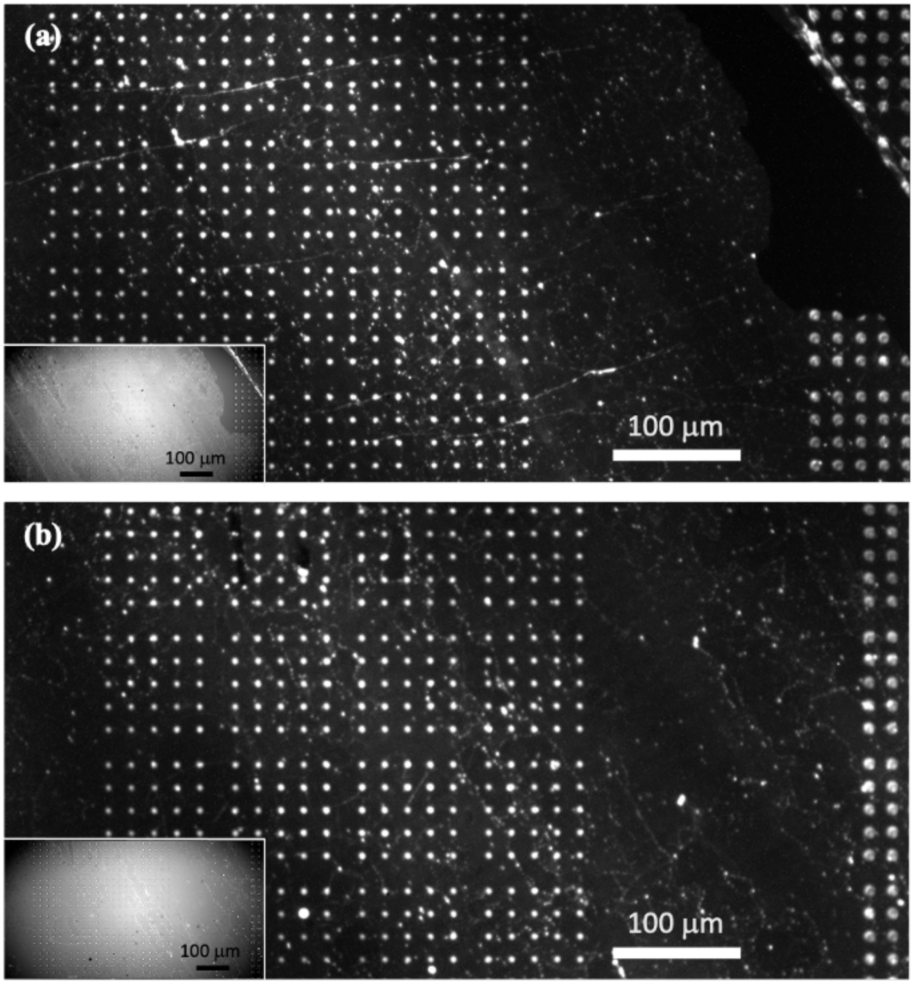

Fig. 4.5. Wide-field images showing arrays of emitters with the corresponding BF image as the inset. Note that the area at the very top right of **(a)** is coated with hBN, though the spread of the microscope illuminator makes it difficult to see from the BF inset. Some tearing as the film came into contact with the pillars is evident near the top left corner in (**b**).

Figure 4.6 shows spectra collected by focusing the pump beam near the edges of various structures using a 0.9 NA 100x objective lens (Zeiss EC Epiplan). We noted that larger features typically resulted in a greater number of peaks from distinct emitters shown in **Fig. 4.6**(a)-(c), which show spectra collected from a 1.6 μm pillar, a 3.6 μm pillar, and an 8 μm bullseye feature. The large density of peaks in **Fig. 4.6**(c) can be attributed to the underlying bullseye feature, where strain is introduced along the inside and outside circumference of the ring feature, in addition to the center pillar. The wavelength distribution of distinct emitters in these figures falls within the well-documented range of hBN emission [24,43,116,129]. These types of sharp spectral features were generally not present in regions between structures. There are two potential causes of the broad background emission accompanying the sharp features present in these spectra. The first is that spectral diffusion resulting from the time-dependent nature of SPEs in hBN might result in what is perceived as broadening [24]. This theory is further supported by 'blinking' diagrams, such as the one presented in **Fig. 4.7**(d), where the respective intensities of individual emitting sites vary greatly over time. This likely impacts the spectra seen in **Fig. 4.6**(a)-(c), since long integration times were necessary to achieve a desirable signal-to-noise ratio. The second potential explanation is the existence of inhomogeneous broadening resulting from the pumping and collection of out-of-plane defects within the multilayer hBN [131,132]. In this case, spectral features from many emitters closely spaced in wavelength could appear as a broad background feature. This theory is further supported by the fact that PL measurements conducted with low NA, higher working distance objectives typically resulted in broad emission spectra that could represent the statistical distribution of hBN emitters across all wavelengths. One such measurement can be seen in **Fig. 3.3**(b)

Figure 4.6(d)-(e) shows a comparison of BF and PL images for a bullseye feature. In this case, the pump beam was expanded (by passing the beam through the lens contained in the microscope illuminator pathway) such that it was larger than the bullseye feature (~ 8 μm) so that the brightness distribution could be visualized on a small scale. A majority of the bright emission (red) is located at the edges of ring and pillar structures, which is consistent with previous findings [24,129] and supports the theory that strain plays a role in some types of hBN emission.

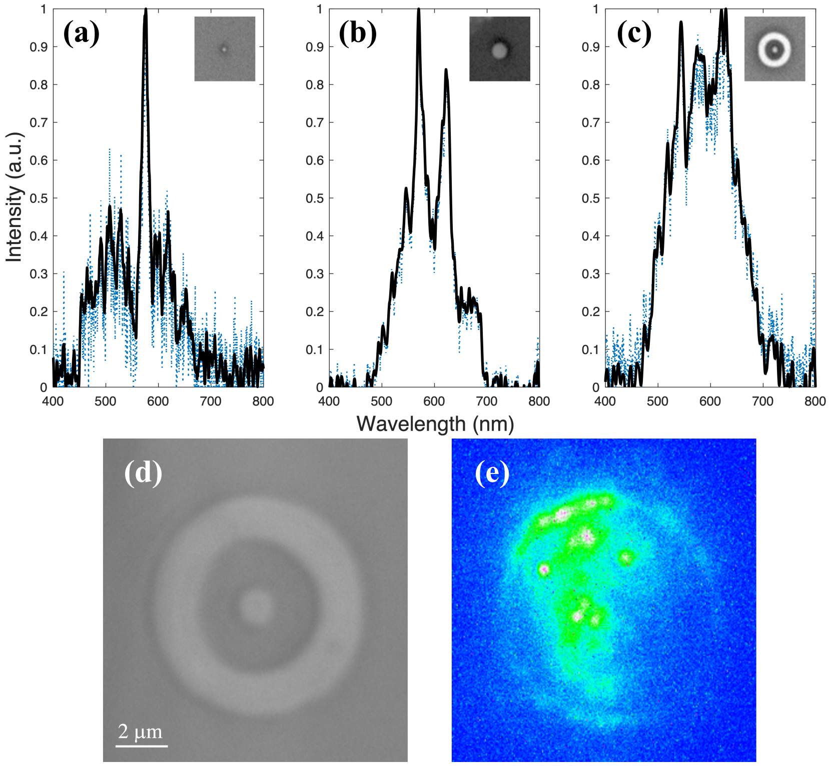

Fig. 4.6. Typical PL results for various features with BF insets shown for reference. Spectrometer data is shown in blue and smoothed data is shown in black. **(a)** Emission from hBN draped on a 1.6 µm diameter pillar. **(b)** Emission from hBN draped on a 3.6 µm diameter pillar. **(c)** Emission from hBN draped on an 8 µm (outer) diameter bullseye feature. **(d)** A BF image of a bullseye feature separate from the spectra shown in (c). **(e)** A PL image showing brightness distribution across the bullseye feature in (d). Emission originates from regions corresponding to the strained film edges.

To further elucidate the origin of emission in our devices we performed a spectral trace measurement on a collection of emitters located on a single 3.6 µm diameter pillar. A PL spectrum of the region is presented in **Fig. 4.7**(a) and shows a number of emitters distributed in the wavelength range 500 nm to 600 nm. The corresponding BF and PL images in **Fig. 4.7**(b)-(c) show that the "hotspots" or brightest regions fall on or near the circumference of the pillar. The corresponding spectral trace measurement in **Fig. 4.7**(d) shows potential spectral jumping of some emitters [133] as well as possible photobleaching around 535 nm. This type of spectral blinking is well documented within hBN [24,43,129,133] and is one indicator that single photon emission could be the dominant mechanism at play.

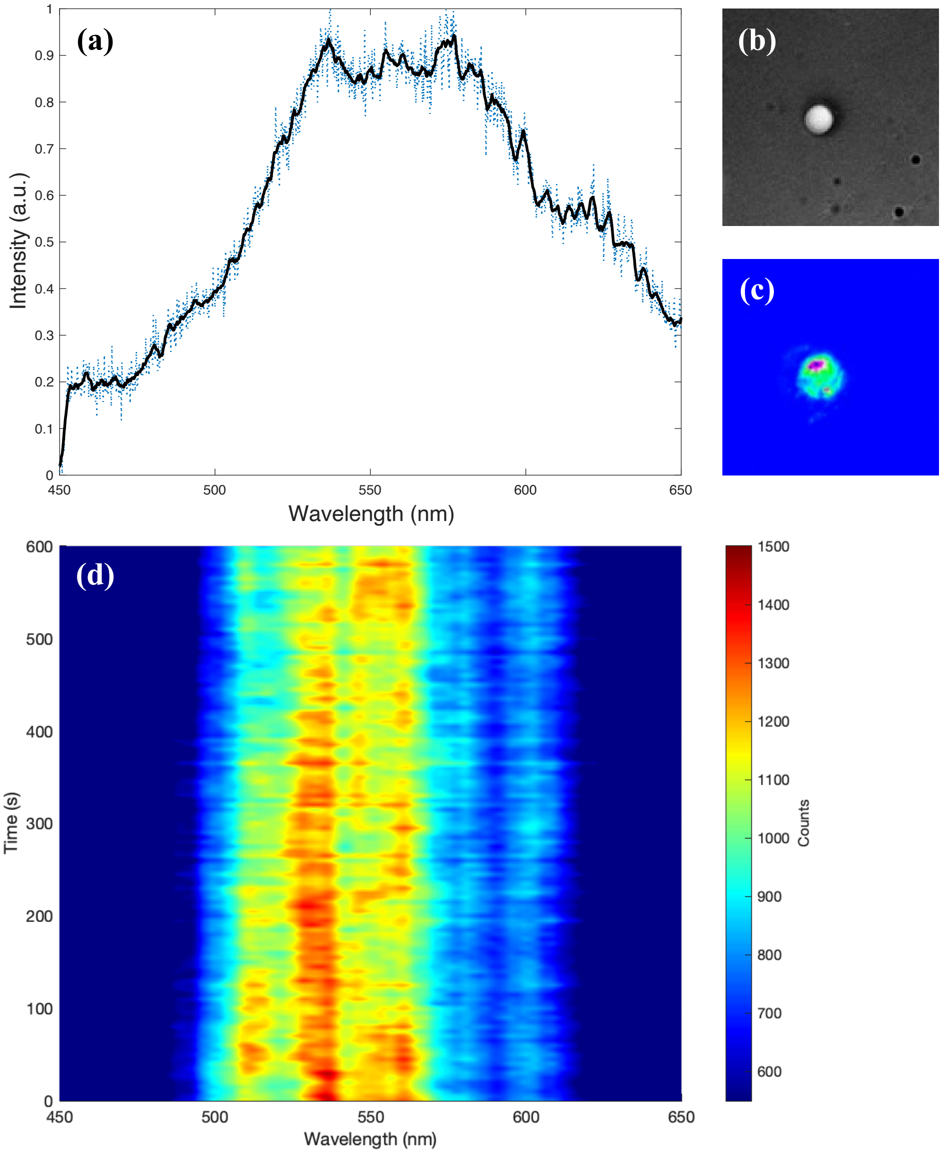

Fig. 4.7. Time dependence of emission in hBN. **(a)** Spectrum of a particular 3.6 µm diameter pillar site showing raw (blue dotted) and smoothed (black) data. **(b)** BF image of the 3.6 µm diameter pillar site. **(c)** PL image of the pillar site. **(d)** Spectral trace diagram illustrating blinking nature of emitters in hBN as well as potential spectral diffusion.[1]

Next, we performed a brightness analysis across multiple arrays of emitters, the locations of which are shown in **Fig. 4.5**(b), using the same wide-field pumping arrangement. It is important to note that the 0.4 NA 20x objective lens (Zeiss EC Epiplan) used to capture these images has a

---

[1] The data presented here is identical to that in the corresponding publication but has been smoothed and scaled for better presentation. This is also more appropriate considering the spectrometer used has a resolution of 7 nm.

depth of field on the order of several microns, so that the light collection efficiency (at fixed focus) is not impacted by the difference in height between the etched and non-etched regions of the samples. **Figure 4.8**(a) shows a set of 12 arrays which have been assigned X and Y coordinates. **Figure 4.8** (b) shows the total distribution of pixels not capturing emission (or "dark pixels") centered around 3.9% of the maximum camera signal before saturation. To see where the brightest pixels were located relative to the sample, we applied a filter that highlighted pixels within a certain 8-bit brightness range and set all other pixel values to zero. The minimum value for which a pixel was considered to be capturing emission (a "bright pixel") was qualitatively set to 24% of the maximum camera signal before saturation. Similarly, the maximum value for which a pixel was determined to be capturing emission was set as 78% of the maximum camera signal before saturation. The upper threshold was applied to remove detector noise, which was naturally present due to the long integration times used to capture images.

The distribution of "bright pixels" across all arrays is given in **Fig. 4.8** where the number of pixels was plotted against the relevant binning range of the 8-bit detector. The inset of **Fig. 4.8**(d) shows the same range of data, but for each individual array. From this, we note that the brightness distribution between neighbouring arrays is relatively consistent, providing a method of determining which arrays are likely to contain many high-quality emitters, such as array X3Y3, where there are many tightly distributed bright pixels.

We were then able to apply this brightness filter directly to the camera images themselves to see where the brightest pixels were occurring. **Fig. 4.8**(c) shows the same X3Y3 array as **Fig. 4.8**(a), but with all "dark pixels" removed, and a uniform color applied to the remaining "bright pixels". The most interesting part of this analysis is that the emission originating from pillar sites appears to be appreciably brighter than emission originating from film wrinkles, given that the outlines of the wrinkles are generally not present in the filtered image. This finding supports the theory of strain activated defect emission, since the phenomenon cannot easily be explained by preferential nucleation during CVD growth as is theorized to be the case in direct-grown methods [129].

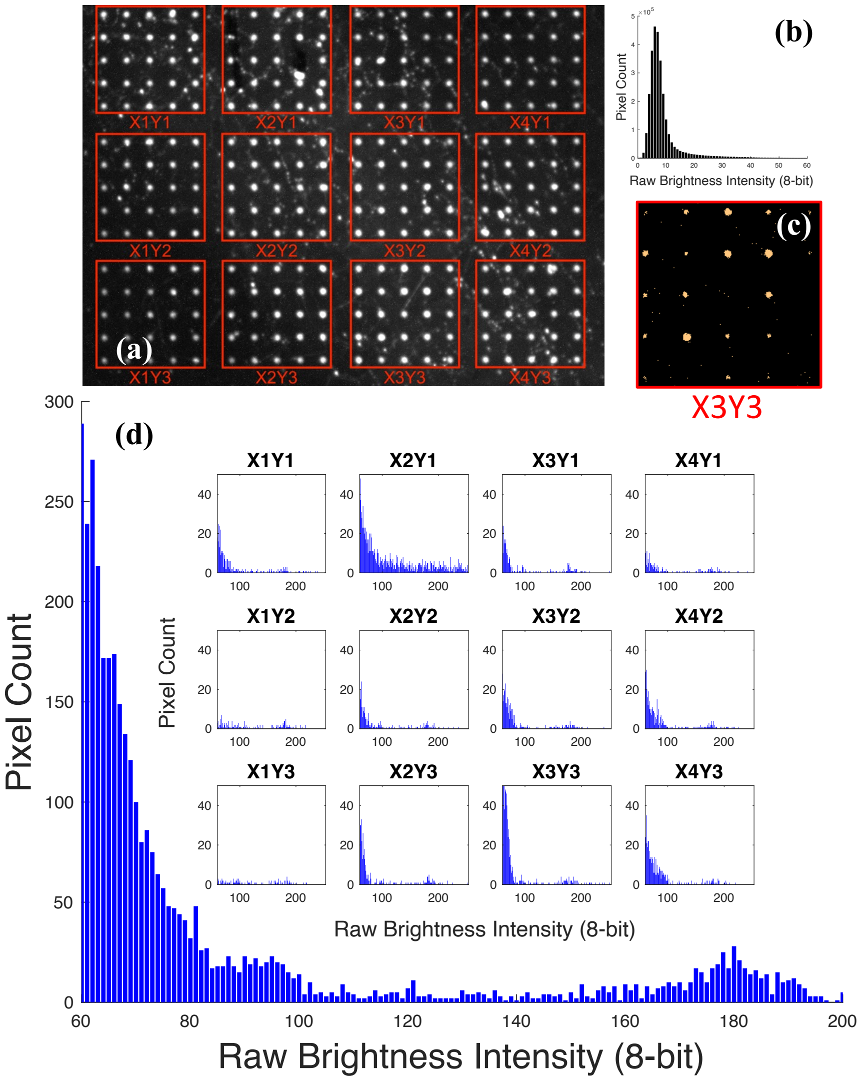

Fig. 4.8. Brightness distribution for an array of ~3.6 μm pillars. **(a)** Arrays of emission corresponding to an array of pillars that have been assigned arbitrary names. **(b)** Distribution of "dark pixels" (*i.e.* pixels not capturing emission) across all arrays. **(c)** A single array from (a) that has been filtered to show the brightest emission or "bright pixels". **(d)** Distribution of bright pixels across all arrays in (a), with the inset showing the distribution of bright pixels for individual arrays.

A similar brightness filter was applied to a large set of arrays on a different area of the sample, shown in **Fig. 4.9**(a), that was entirely coated with hBN. This figure is a combination of BF (red) and PL (cyan) data, with only the brightest pixels coloured. Again, we found that the brightest emission was correlated to pillar sites rather than wrinkles, and furthermore, that this observation held true across different regions of the transfer. **Figure 4.9**(b-d) shows the effect of increasing the bright pixel floor on the emission from arrays of different hBN coated features. We chose to sweep from 3.9% to 35.3% as this range showed both emission from unintentional wrinkles as well as emission from pillar sites being gradually filtered out. Emission originating from wrinkles was generally filtered out at a lower brightness floor compared to emission originating from substrate features. Additionally, we found that emission from larger pillars (diameter ~ 3.6 μm) was generally more uniform in brightness between individual features compared to smaller pillars (diameter ~1.6 μm) or bullseyes. The difference in circumference and therefore potential for emitters to form might explain the difference between small and large pillars. In the case of the bullseye features, the brightness is far less consistent between emitting sites, which might be due to the comparatively low aspect ratio resulting in less uniform strain from feature to feature. For example, **Fig. 4.3**(e) shows the edge of an hBN film partially conforming to a bullseye feature in a somewhat unique way compared to the coated pillars in **Fig. 4.3(a)**.

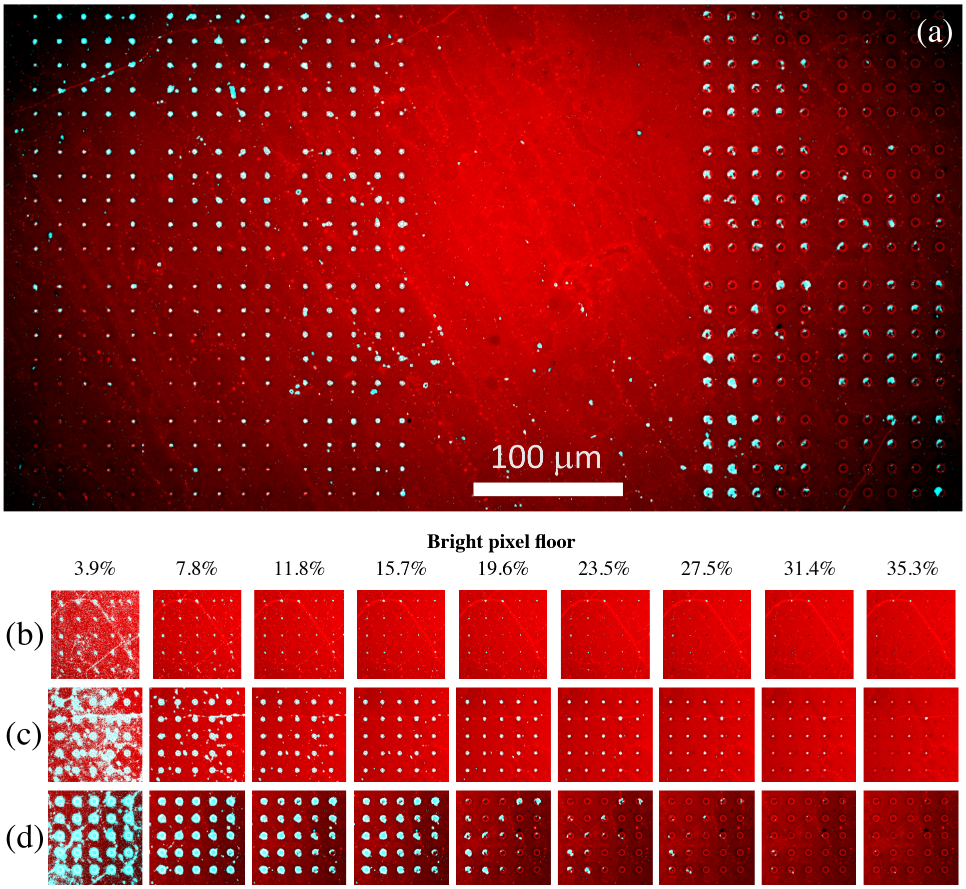

Fig. 4.9. Filtered PL images overlayed on BF images of the same region. These images were generated using post-processing similar to that described in Fig. 8. **(a)** Wide-field PL measurement showing pixels in the range 24% to 78% brightness before saturation. **(b)** Varying brightness floor

applied to an array of 1.6 μm pillars. **(c)** Varying brightness floor applied to an array of 3.6 μm pillars. **(d)** Varying brightness floor applied to an array of 8 μm bullseyes. Emission corresponding to wrinkles is filtered out at a lower brightness floor compared to emission corresponding to patterned features. This observation holds true for all feature types.

4.4 Further optical characterization

The spectral results in Section 4.3 were collected using an Ocean Optics USB 4000 spectrometer configured to have a resolution of ~ 7 nm, placing a limit on our characterization abilities. The DeCorby group recently acquired a far superior Ocean Optics QEPro configured to have a resolution of ~ 0.7 nm (as well as significantly higher sensitivity) which allowed us to expand upon our existing results. **Figure 4.10** provides a more complete optical characterization for a 5x5 array of hBN-coated 1.6 μm diameter pillars using the optical system shown in **Fig. 4.4**. In this case, the integration time was 1 second and a Newport FS-ND 30 filter was used to limit the power incident on the sample to ~ 0.7 mW. These results provide further insight into the spectral properties of hBN emitters, particularly **Fig. 4.10(b-c)** where the spatial and spectral distribution of presumed ZPLs across all emitters are analysed. **Figure. 4.10(b)** shows the statistical distribution of the dominant peak from each pillar site, binned into 5 nm windows. Some pillars exhibited multiple dominant peaks very close in intensity such as **Fig. 4.10(e)**, in which case all the maxima were included in the analysis. The dominant ZPLs across the array were centered around ~ 594 nm, which is consistent with other accounts of transferred hBN films [11,24]. The 1.6 μm diameter pillars each hosted ~ 7 distinct emission peaks on average, as shown in **Fig. 4.10(c)**. A PL blinking diagram for the emitters hosted on pillar X5Y5 is also presented in **Fig. 4.10(i)** very clearly demonstrating spectral blinking of an emitter centered near 600 nm.

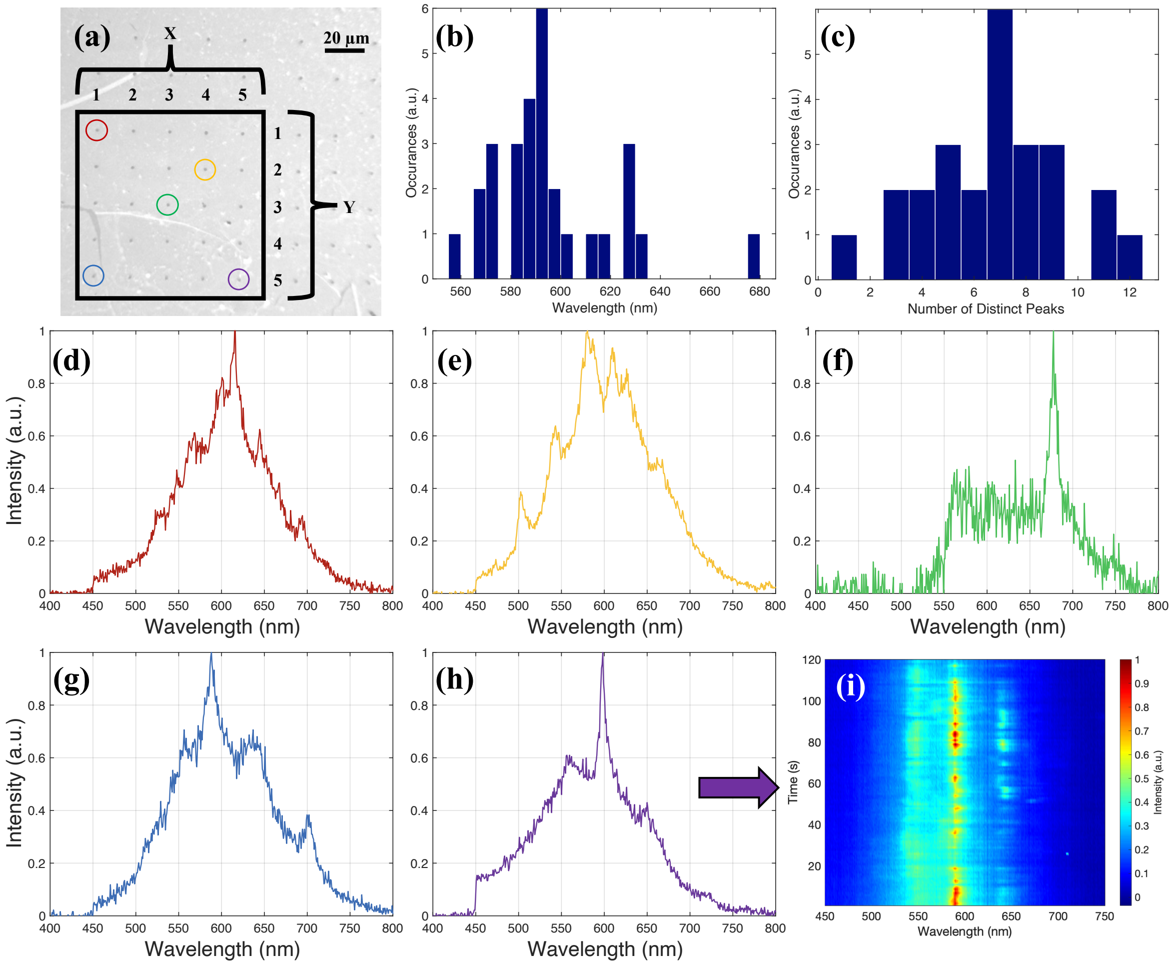

Fig. 4.10. Optical characterization for a 5x5 array of hBN-coated 1.6 µm pillars. **(a)** A BF image showing an array of pillars with assigned X and Y values. Pillars with optical measurements presented have been circled in their respective trace colours. **(b)** A histogram showing the wavelength of the dominant peak of the pillars shown in (a). **(c)** A histogram showing the number of distinct PL peaks collected from the pillars shown in (a). **(d)** A PL spectra of pillar X1Y1. **(e)** A PL spectra of pillar X4Y2. **(f)** A PL spectra of pillar X3Y3. **(g)** A PL spectra of pillar X1Y5. **(h)** A PL spectra of pillar X5Y5. **(i)** A time trace showing blinking and diffusion of the emitters from pillar X5Y5. All spectra have been background corrected by subtracting the photoluminescence signal obtained from a nearby area.

4.5 Conclusions

In summary, we have presented a polymer-assisted hBN transfer method that reliably produces defect-based emission in strained areas. This method achieved ~80% successful transfer by area. Our wide-field PL results show not only that areas of hBN emission correspond to underlying patterned structures, but also that the brightest emission occurs at these areas rather than at unintentional wrinkles in the film. Our findings reinforce the theory that strain is one of the mechanisms responsible for emitter activation in hBN. We also presented emission spectra collected near the strained edges of hBN-coated structures and showed that the number of distinct emitters scales with feature size. Future work will involve a more complete optical characterization with the overall goal of realizing arrays of hBN-embedded optical cavities functioning as SPEs.

Chapter 5 – Integrating thin-film hexagonal boron nitride into buckled microcavities

5.1 Introduction

Quantum emitters within hexagonal boron nitride (hBN) have been demonstrated to possess several attractive properties, such as room temperature operation and chemical stability [11,55], which make them excellent candidates for integrated technologies with broad applications in quantum computing, quantum information, and quantum sensing [55,82,134,135]. On top of this, hBN emitters are bright, exhibit good photostability, and possess high quantum efficiencies, in some cases upwards of 80% [11,118]. Recent progress has seen position-controlled emission in hBN (activated via electron beam irradiation) that is reliably reproducible in wavelength [136], emission linewidth reduction by use of a conductive host substrates [137], and high-fidelity photonic microelements fabricated directly from hBN flakes [138], to name a few.

In addition to engineering the optical properties of hBN, particular emphasis has been placed on developing a deeper understanding of the physical mechanisms behind its emissive properties. There are currently several viable models circulating including donor-acceptor pair transitions [139], quantum emission from the V_NN_B lattice defect based on density functional theory calculations [122], as well as several reports of carbon-based defects being the source of single-photon emission [53,54,140]. At the same time, experimental evidence for so-called strain-activated emission has been observed [24,27,57,60,62], with one potential explanation for this phenomenon being that emission from strained regions is the result of charge carrier trapping. Regardless of the exact origin of emission, widefield photoluminescence images clearly reveal localized emission near prepatterned substrate features [24,57], making this method an exciting candidate for optical device integration.

The aforementioned advances in understanding emission mechanisms paired with recent developments in fabrication methods means that various resonator schemes are becoming more feasible. Examples include hybrid tunable cavities [66], dielectric cavities [64,141], plasmonic cavities [142], and micro-ring resonators [67]. While substantial progress has been made in this area, three-dimensional confinement with a fully integrated device has largely remained a challenge. However, our recently developed "monolithic buckled microcavity" devices are a promising candidate [95,143]. We present a fabrication process for embedding hBN nanofilms into three-dimensional cavities, fabricated using a thermal buckling self-assembly process and show preliminary optical results.

5.2 Optical design and simulation

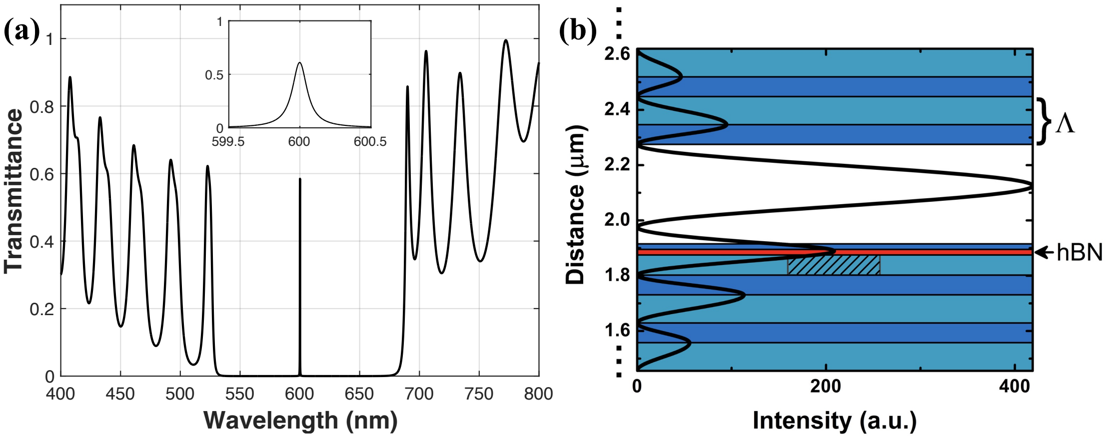

Fig. 5.1. Transfer-matrix predictions and FDTD simulation of a dome compatible with hBN emission. **(a)** Transmittance spectrum for the planar equivalent model of the cavity showing a resonant mode at 600 nm with a linewidth of ~ 0.13 nm. **(b)** Electric field intensity profile corresponding to the resonant mode shown in (a). The diagonal lines represent a region in the oxide that is etched in the physical device. Note that only a portion of the top and bottom mirror are shown so that the inner layer structure can be seen clearly.

We used a planar mirror approximation (given the large radius of curvature of the buckled top mirror) and ran transfer matrix simulations to converge on a set of film thicknesses and etch parameters. We noted that it was possible to maximize the electric field magnitude within the hBN film relative to the cavity airgap by treating the SiO_2 etched hole layer and hBN as a singular quarter wavelength stack, effectively adding another half-period to the 10.5 period bottom mirror. This design decision can be modelled using the following equations:

$$(\lambda_0/2)(a-1/2) = \mathrm{OPL}_{\mathrm{hBN}} + \mathrm{OPL}_{\mathrm{oxide}}, \tag{5.1}$$

$$\Rightarrow d_{\mathrm{oxide}} \approx [(\lambda_0/2)(a-1/2) - d_{\mathrm{hBN}} n_{\mathrm{hBN}}]/n_{\mathrm{oxide}}. \tag{5.2}$$

Here, the optical path length (OPL) of the pillar and hBN layers are the product of the index and film thickness, and a represents the periodically recurring quarter-wave condition required to align the electric field to the hBN layer. Setting the cavity resonance at $\lambda_0 = 600$ nm (the approximate center of the Bragg mirror stopband), it was found that $a = 1$ resulted in a hole depth of ~ 73 nm, and that any higher-order solution resulted in feature heights which reported will pierce a PMMA-transferred hBN film [24,129]. Once the lower mirror has been designed to position the cavity resonance roughly at the hBN emitter location, the buckled airgap height determines the resonant wavelength of the device. **Figure 5.1**(a) shows a simulated transmission plot for a Bragg cavity with the resonance centered at $\lambda_0 = 600$ nm (with an airgap thickness of 361 nm). **Figure 5.1**(b) shows the corresponding electric field intensity vs distance plot for the theoretical planar cavity described. The secondary field intensity maximum has been aligned to the hBN film within the cavity. The relation between the hBN field intensity and airgap intensity has important implications on emission enhancement that can be described by the equation:

$$F_P = (3/4\pi^2) \cdot (Q\lambda_0^3/V) \cdot \left(\left|\vec{E}(\vec{r})\right|^2 / \left|\vec{E}_{\max}\right|^2\right), \tag{5.3}$$

Where the conventional Purcell factor can be written to include the effect of a field misalignment when the emitter is no longer located at the maximum electric field within a cavity. Using the transmittance plot at ~ 600 nm shown in **Fig. 5.1**(a), we estimate a simulated linewidth of ~ 130 pm and therefore a quality factor of ~ 4600. The mode volume for a 40 μm diameter cavity centered on the second-order fundamental is on the order of ~ 3.6 λ^3 based on equations presented in previous work [95]:

$$V_M \approx \left({}^{\pi}/_{4}\right) w_0^2 L \approx \left({}^{\pi}/_{4}\right) L^{3/2} r_2^{1/2}. \tag{5.4}$$

Combining this with the field intensity plot shown in **Fig. 5.1**(b) to account for the electric field offset, we estimate a Purcell factor of ~ 60 for an emitter in for the theoretical device described. It is also worth noting that additional non-idealities can be introduced in the Purcell factor equation, such as spectral misalignment and polarization misalignment, though these are inherently more challenging to account for in our cavity design and have therefore been neglected in the analysis above.

Finite-difference time-domain simulations of a 40 μm diameter dome can be seen in **Fig. 5.2**. A representative Lumerical script has also been included in Appendix D. The field optimization layer and the hBN layer were approximated by a single quarter-wave low index layer, effectively making the bottom mirror 11 layers thick. The peak buckle height was chosen to couple to the first-order fundamental resonance ($L = 300$ nm) both for simplicity as well as to decrease simulation time. As shown in **Fig. 5.2**(a), the simulated Purcell factor for the first-order fundamental was ~ 54 which is in reasonable agreement with analytical predictions for the second-order fundamental mode above. The spacing between transverse modes is ~ 3 nm. The first three z-normal Laguerre-Gaussian mode profiles can be seen in **Fig. 5.2**(c-e) and are consistent with what has previously been observed in DeCorby group buckled microcavities [68,95].

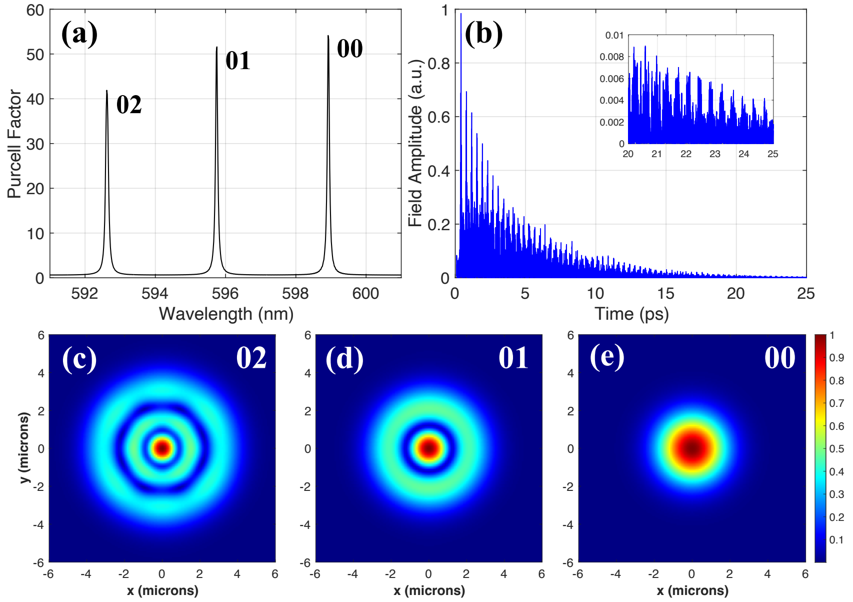

Fig. 5.2. FDTD simulations for a 40 μm diameter cavity without an etched hole in the field optimization layer. **(a)** A plot showing the first three resonant modes with the fundamental centered near 599 nm. **(b)** A time monitor showing the electric field decay inside the cavity. **(c)** Mode profile for the LG02 mode. **(d)** Mode profile for the LG01 mode. **(e)** Mode profile for the LG00 mode. The mode profiles have been scaled to arbitrary units in accordance with the colour bar on the right-hand side.

5.3 Device fabrication

The first step in our fabrication process was to deposit a 10.5 period Ta_2O_5/SiO_2 Bragg mirror on a piranha-cleaned silicon substrate (**Fig. 5.3** Step 1) using the parameters given in **Table 5.1**. The ~ 73 nm SiO_2 field optimization layer was sputtered directly on top of the final mirror period, and a reflection plot of the thin film structure following this step can be seen in **Fig. C.2**. The entire structure was once again piranha-cleaned in preparation for patterning the hole layer. The wafer was spin-coated with AZ 1529 resist using 10 seconds at 500 rpm for the spread step and 60 seconds at 3000 rpm for the spin step. A bake time of 60 seconds at 100 °C was used to cure the resist, which was typically ~3 μm thick. A Heidelberg MLA 150 was used to pattern the resist with a dosage of 230 mJ/cm^2 at a wavelength of 405 nm. The wafer was developed using AZ 400K in a 1:4 dilution with water for 115 seconds to remove the exposed photoresist. Holes were etched all the way through the SiO_2 field optimization layer using an inductively coupled plasma reactive ion etching system following the parameters given in **Table 5.2** (**Fig. 5.3** Step 2). The leftover resist was removed in a room-temperature acetone bath followed by an oxygen plasma etch, the recipe for which is also shown in **Table 5.2**.

Table 5.1. Bottom mirror sputtering parameters

Layer	Ta_2O_5	SiO_2	Field optimization (SiO_2)
Target thickness [nm]	71	102	73
Time [m:ss]	5:42	6:43	4:48
Temperature [C]	150	150	150
Power [W]	200	200	200
Off-time [µs]	5	0.8	0.8
Frequency [KHz]	20	150	150
Gas/Rate [sccm]	Ar/40	Ar/50	Ar/50
Gas/Rate [sccm]	O_2/20	O_2/3.2	O_2/3.2
Deposition pressure [mT]	3.7	3.7	3.7
Ramp-up [s]	60	600	600
Burn-in [s]	120	120	120
Ramp/burm pressure [mT]	7	10	10
Film Stress [MPa]	-189	-258	-258

We subsequently multilayer hBN (Graphene Supermarket CVD-2X1-BN-ML) to the surface of the patterned mirror using a process flow described in previous work [57]. 20 nm of Ta_2O_5 was deposited directly on top of the hBN surface to serve as a protective capping layer for subsequent processing steps (**Fig. 5.3** Step 3). We performed a second lithography process to pattern domes centered around each hole feature, this time using a thinner photoresist (AZ 1512). The spin settings were 10 seconds at 500 rpm for the spread step and 40 seconds at 5000 rpm for the spin step. The exposure dosage was 180 mJ/cm^2, again patterned using the 405 nm diode laser contained within the MLA 150. The wafer was developed using AZ 400K in a 1:4 dilution with water for 20 seconds A ~ 15 nm thick fluorocarbon low adhesion layer was deposited on the patterned wafer using an Estrelas ICPRIE (Oxford) followed by liftoff via sonication in acetone for ~ 1 hour. The devices were then rinsed with isopropyl alcohol followed by water and allowed to dry. A second 10.5 period Ta_2O_5/SiO_2 Bragg mirror was then deposited directly on top of the patterned fluorocarbon layer (**Fig. 5.3** Step 4) again using the parameters from **Table 5.1**. The domes were buckled using either a rapid thermal annealer or a standard hotplate. In the case of the rapid thermal annealer, buckling was performed in an argon environment at either 475 °C or 550 °C. Hotplate buckling was performed under a fume hood by ramping the devices from 150 °C to

500 °C at a rate of 50 °C/min. Thermal shock combined with stress inherently present in the top mirror causes buckling delamination to occur wherever the low adhesion layer was patterned, resulting in the formation of closed dome-shaped cavities.

Table 5.2. Etching equipment parameters

Step	O_2 Strip	SiO_2 Etch	PTFE Deposition
Gas/Rate [sccm]	O_2/50	CHF_3/50	C_4F_8/40
Gas/Rate [sccm]	N/A	SF_6/25	N/A
Gas/Rate [sccm]	N/A	Ar/25	N/A
Time [sec]	120	140	7
Power [W]	200	1000	600
Temperature [C]	20	20	0
Pressure [mT]	100	90	5

A schematic representation of the final device can be seen in **Fig. 5.3**. Hole diameters were either 1 µm or 2 µm and buckled dome diameters ranged from 40 µm to 60 µm. A bright field image showing a top-down view of a fabricated device is also presented, along with an example scanning electron microscope image of an etched hole showing an hBN film conforming to the substrate topology, thus introducing strain.

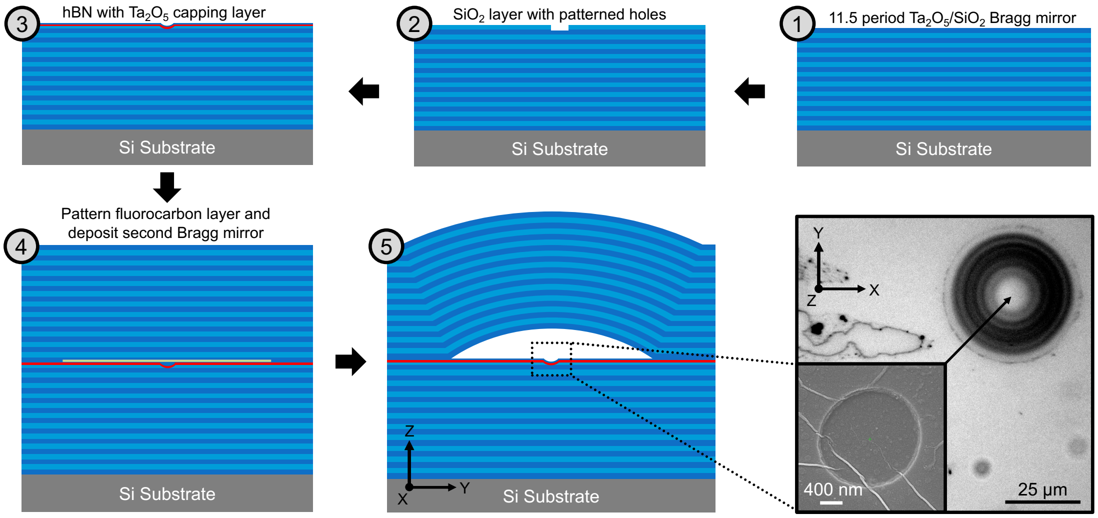

Fig. 5.3. Fabrication overview for hBN embedded buckled microcavities. The process was carried out as follows. (1) A 10.5 period Ta_2O_5/SiO_2 (dark blue/light blue) Bragg mirror starting and ending with Ta_2O_5 is sputtered onto a Si (grey) substrate. (2) A field optimization SiO_2 layer is deposited, patterned with photoresist, and etched. (3) A continuous hBN film (red) is transferred on to the substrate, followed by a Ta_2O_5 capping layer. (4) A low adhesion fluorocarbon layer (light green) was patterned, and liftoff was performed before a second, identical Bragg mirror was deposited. (5)

The device was heated, which caused the upper Bragg mirror to buckle (not to scale). The bright field image in the bottom right pane shows the top-down view of a non-hBN-coated 50 μm diameter buckled dome containing a 2 μm diameter hole. The accompanying SEM inset shows a representative top-down view of an SiO_2 hole with transferred hBN film. Wrinkled areas were specifically imaged to show the resulting deformation as the hBN film conforms to the hole topology.

An array of buckled 60 μm microcavities containing 2 μm is shown in **Fig. 5.4**. Note that these cavities are from an area where hBN transfer was not preformed. Finally, we noted that aggressive processes such as piranha cleaning had to be avoided once hBN was transferred to a substrate, as these processes resulted in the film delaminating from the substrate, even in the presence of a 20-50 nm $Ta2O_5$ capping layer sputtered directly on top of the hBN. This problem could potentially be avoided using a thicker capping layer at the expense of electric field optimization (and therefore Purcell enhancement) within the cavity. In the future, the ability to piranha clean prior to patterning the low-adhesion layer could potentially lead to a higher device yield as well as improved optical results.

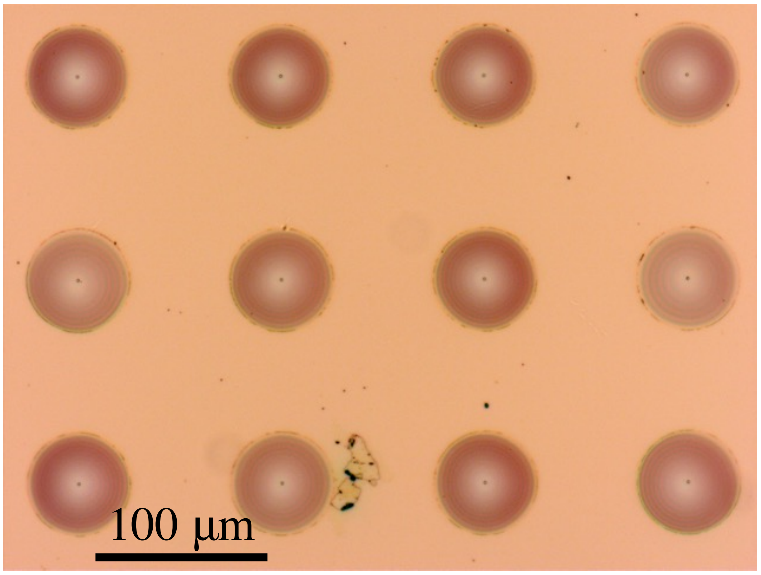

Fig. 5.4. A microscope image showing an array of 60 μm diameter microcavities containing 2 μm diameter holes etched into the top layer of the bottom mirror. The holes are somewhat visible through the top mirror.

5.4 Device characterization

Fig. 5.5 shows dome height measurements of gold-coated (40, 50, and 60 µm diameter) domes containing 1 µm holes, as measured with ZYGO profilometry of a 1 cm by 1 cm unit cell. The average heights in each case were 1.8 ± 0.2 µm, 2.5 ± 0.2 µm, and 3.2 ± 0.5 µm, respectively. Interestingly, but perhaps expectedly, both the 40 µm and 50 µm diameter domes have a tighter distribution about the mean than the 60 µm domes, and the standard deviation from mean buckle height seems to increase with diameter. Example profilometry measurements along with fits to radii of curvature are presented in **Fig. 5.6**. While the example 50 µm dome presented is a statistical outlier in terms of height, the buckled mirror effective ROC (100 µm) for all the example devices is quite representative of the domes studied below. As an example, using Equations (2.19) and (2.20), a Rayleigh range of 13.3 µm, beam waist of 1.6 µm, and therefore effective NA of 0.12 can be estimated for an average 40 µm dome. **Table 5.3** summarizes the buckle height and radius of curvature results. A sampling of the gold-coated domes used in profilometry measurements can be seen in **Fig. C.4**

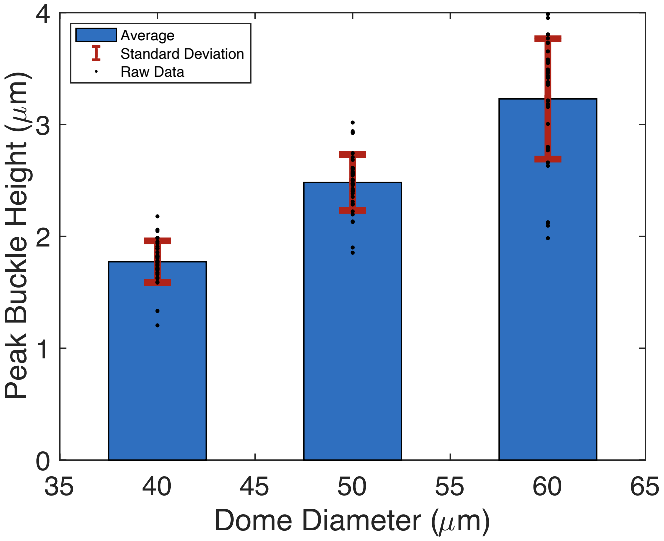

Fig. 5.5. Peak buckle height statistics for domes of each diameter, all containing a ~ 1 µm diameter hole etched into the field optimization layer.

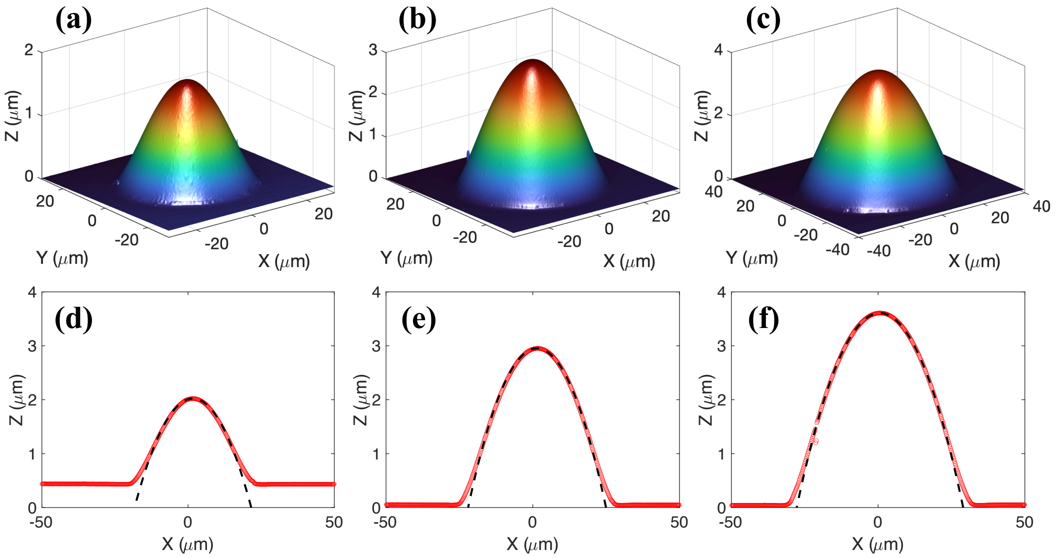

Fig. 5.6. Profilometry fits for sample devices. ZYGO data for **(a)** A 40 μm dome, **(b)** a 50 μm dome, and **(c)** a 60 μm dome. Extracted radii of curvature for **(d)** A 40 μm dome, **(e)** a 50 μm dome, and **(f)** a 60 μm dome.

Table 5.3. Overview of dome statistics.

Dome diameter	Mean peak buckle height	Standard deviation	Example ROC
40 μm	1.8 μm	0.2 μm	99.4 μm
50 μm	2.5 μm	0.2 μm	95.0 μm
60 μm	3.2 μm	0.5 μm	113.3 μm

Photoluminescence images and spectra of planar regions were obtained using a homebuilt quasi-confocal system similar to that described in Chapters 3 and 4. Briefly, the excitation source was a 405 nm Pangolin laser (LDX-405NM-200MW) aligned to a neutral density filter (Newport FSQ) and adjustable iris. The beam was then passed through a 450 nm short pass filter and a 468 nm short pass filter (Thorlabs FESH0450 and Semrock FF01-468, respectively) and directed towards the sample at a glancing angle. Light emitted from the sample was then collected with a 0.13 NA 5x objective lens (Zeiss EC Epiplan). A subsequent 450 nm long pass filter (Thorlabs FELH0450) was used at the input of a 90:10 beamsplitter (Thorlabs BS025) to remove pump light. The collected light was split between a CMOS camera (Thorlabs CS895MU) and a 50 μm core pickup fiber (Thorlabs FG050LGA). The fiber was mounted to a FC/PC collimator with a focal length of 34.74 mm (Thorlabs F810FC-543) at the 90% terminal of the beamsplitter. The output of the fiber was coupled directly into an Ocean Optics QE Pro visible range spectrometer with a slit width of 25 μm. Planar reflection measurements were obtained using the microscope halogen illuminator as a source. A 50 µm core fiber was again used to limit the FOV to a specific region on the sample.

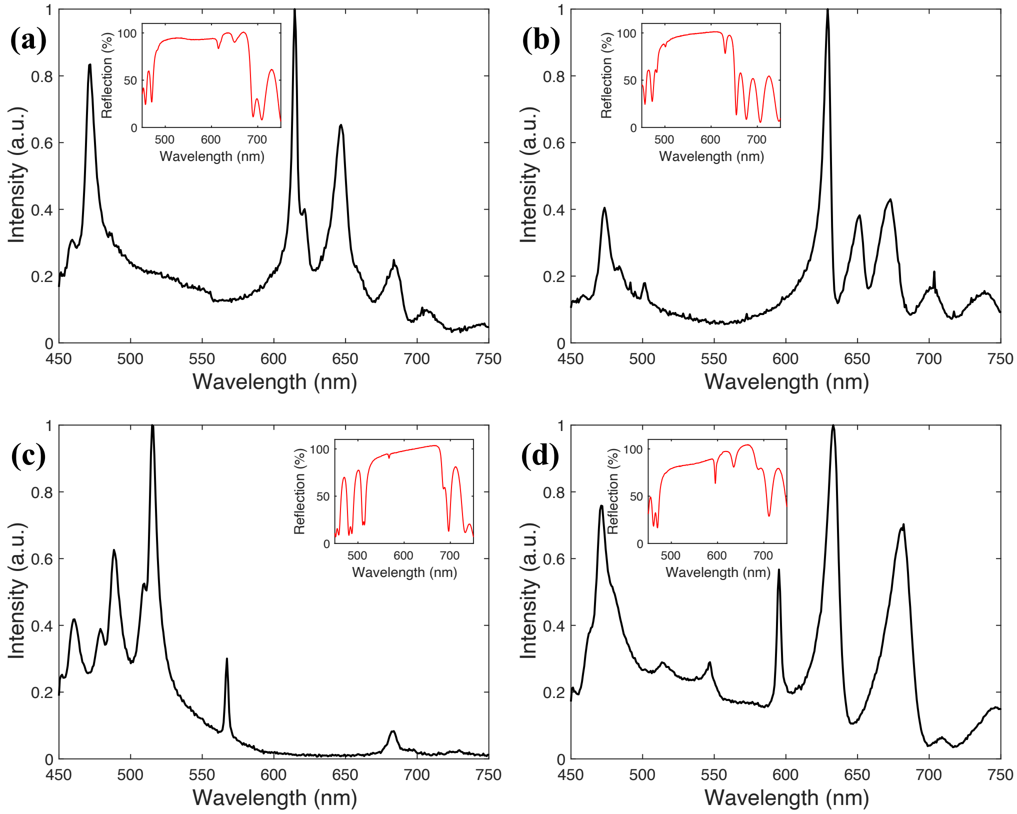

Fig. 5.7. (a) – (d) Photoluminescence measurements for a variety of hBN-coated planar regions. Corresponding reflectance plots are also shown as insets. Wavelength shifts in the modes and stopbands are due to variations in film thickness across samples.

Figure 5.7 contains PL spectra from planar regions on the sample where a mode is supported within the stopband or strong coupling into the edge of the stopband is observed. Respective reflection measurements of the same regions are shown as insets for reference. The modes observed here possess a FWHM on the order of several nanometers, as opposed to ~ 130 pm as was predicted by transfer matrix simulations. One possible explanation for this discrepancy is spectral broadening resulting from a combination of the NA of the collection optics and walk-off due to the critically stable planar mirrors. This theory is supported by the fact that the spectral broadening became increasingly apparent as higher magnification (and thereby higher NA) objectives were used, as demonstrated in Chapter 3.

Figure 5.8(a) shows a widefield PL image of an hBN-coated region partially covering an array of unbuckled (*i.e.,* planar) devices. A bright-field image of the same region is shown in **Fig.**

5.8(b) for comparison. Emission is somewhat localized to the center of the cavities that contain holes, but there is also undesirable emission originating from other places, such as wrinkles, cracks, and regions corresponding to unbuckled PTFE pads. Photoluminescence images of buckled domes with corresponding BF images can be seen in **Fig. 5.8**(c-f). There is clearly emission originating from the regions corresponding to buckled domes, however there is also a large amount of undesirable emission originating from much of the hBN-coated region. We theorize that some of the undesirable emission and roughness here might be a result of sputtering a capping layer directly over the hBN layer. In addition to the poor optical quality of most of the hBN-embedded domes, we found that selecting a buckling method and temperature was non-trivial. For the samples that were buckled using an RTA, entire regions coated with hBN tended to delaminate from the surface. **Figure C.8** shows a region where a millimeter-sized portion of the top mirror has detached from the sample over an hBN-coated feature. Although hotplate buckling resulted in a much lower overall yield, the major advantage was that a small region of interest could be monitored during the process by mounting a camera directly overhead.

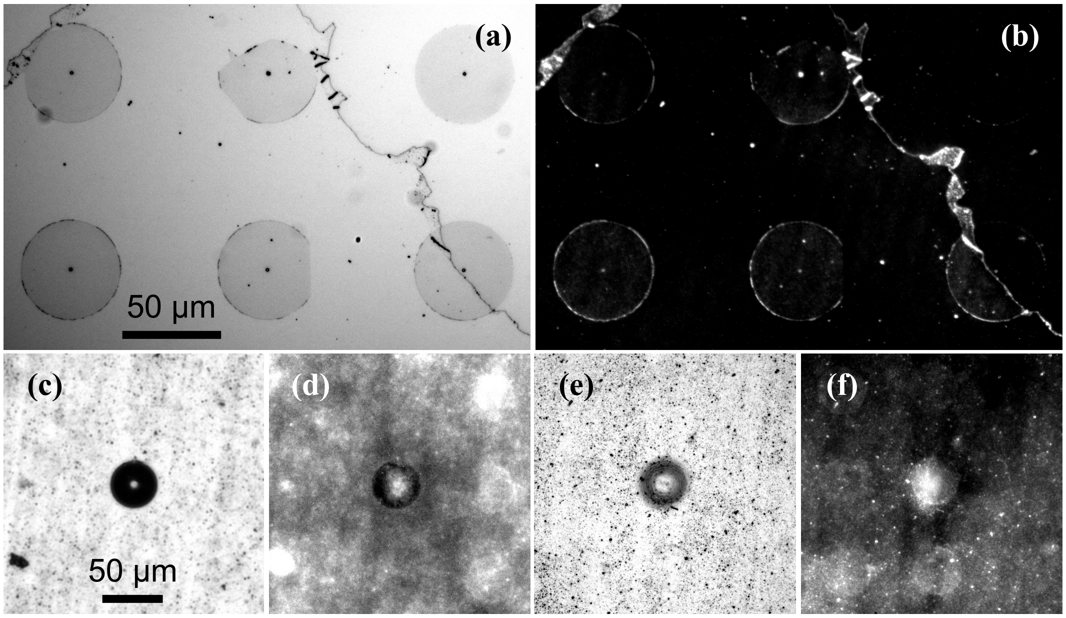

Fig. 5.8. Photoluminescence and bright-field images for various regions. **(a)** A BF image showing a partially hBN-coated set of unbuckled 50 µm domes. **(b)** A PL image showing preferential emission near edges of the hBN film corresponding to etched holes and PTFE pads. **(c)** A BF image taken with a 5X objective showing a 40 µm dome buckled over top of a rough hBN-coated region. **(d)** A corresponding PL image taken with a 5X objective of the region in (c). **(e)** A BF image taken

with a 20X objective showing a 40 μm dome buckled over top of a rough hBN-coated region. **(e)** A corresponding PL image taken with a 5X objective of the region in (f).

While Bosch-process Teflon was used as the low-adhesion layer for patterning the domes, we noticed that certain conditions caused the hBN layer to delaminate from the substrate. Sometimes this naturally occurred in a circular pattern, resulting in the formation of "accidental" domes. **Figure C.7** shows an image of a region where this has happened. The implication of this finding is that it may be possible to use hBN as the low-adhesion layer, simplifying the fabrication process. This might be achieved by masking and etching the transferred layer in the same way the Teflon was patterned in our process flow, similar to how others have integrated hBN into 1D photonic crystal cavities [65]. The caveat here is that we are not certain what happens to the low-adhesion layer during the buckling process, and that the hBN could be damaged or displaced from the local field maxima.

Neither reflection measurements nor emission spectra could be obtained for individual domes with the microscope setup used, due to the nature of the curved surface and spectral broadening discussed in Chapter 3. Transmission scans were also unachievable as the bottom Bragg mirror was deposited on a silicon substrate, which was an oversight during the fabrication process. To get around this inconvenience we developed a measurement scheme based on a cleaved fiber, a full diagram of which can be seen in **Fig. 5.9**. A supercontinuum source (NKT Photonics SuperK COMPACT) was connected to the primary input of a 90:10 wideband directional coupler (Thorlabs TW560R2A2). The 10% tapped output was connected to a cleaved 460HP fiber that was positioned directly above the device under test. The 90% primary output was capped with a broadband fiber terminator. The reflected light from the sample that coupled back into the cleaved fiber was collimated into free-space and measured using a spectrometer (Ocean Optics QEPro) at the tapped input terminal of the splitter. Two cameras with zoom attachments were used for precise alignment of the cleaved fiber.

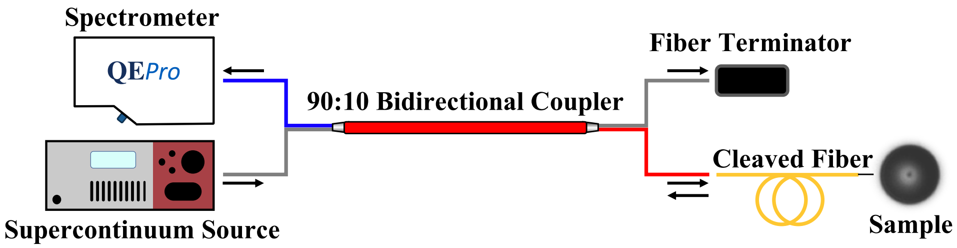

Fig. 5.9. A Schematic representation of the system used to obtain reflection measurements of buckled dome microcavities. A supercontinuum source is passed through a bidirectional coupler and into a cleaved fiber that is coupled to the cavity modes. The reflected light propagates back through the coupler and is measured using a spectrometer.

A representative reflection spectrum showing a family of modes obtained from a 60 μm dome can be seen in **Fig. 5.10** along with camera images of the measurement. The broad background notch superimposed on the family of modes could either be an artifact of the source spectrum (shown in **Fig. C.10**(a)) or the convolution of the modes themselves as the spectrometer is not capable of fully resolving them. It is also worth noting that the spacing of what appear to be transverse modes is ~ 5 nm, which is slightly larger than predicted using FDTD simulations but still reasonable. Note that the reflection plot is presented without normalization against the source or measurement system, as proper normalization would involve collecting reflection spectra from a featureless surface at the exact same working distance. The cleaved fiber needed to be placed extremely close to the device under test to achieve desirable results (**Fig. 5.10**(b)) and prevent a secondary Fabry-Perot cavity formed by the dome and fiber face from dominating the measurement. Damage often occurred as the fiber face came into physical contact with the dome. **Figure 5.10**(c-d) shows camera images with the fiber backed off from a dome. A bright spot is visible in **Fig. 5.10**(c), which we speculatively attributed to the cavity modes since the light exiting the fiber core is divergent and therefore should not focus down to a spot. In addition, the bright spot appears to "stick" to the dome when the fiber is moved slightly, further suggesting it is result of light interacting with cavity modes rather than light reflecting off the curved surface.

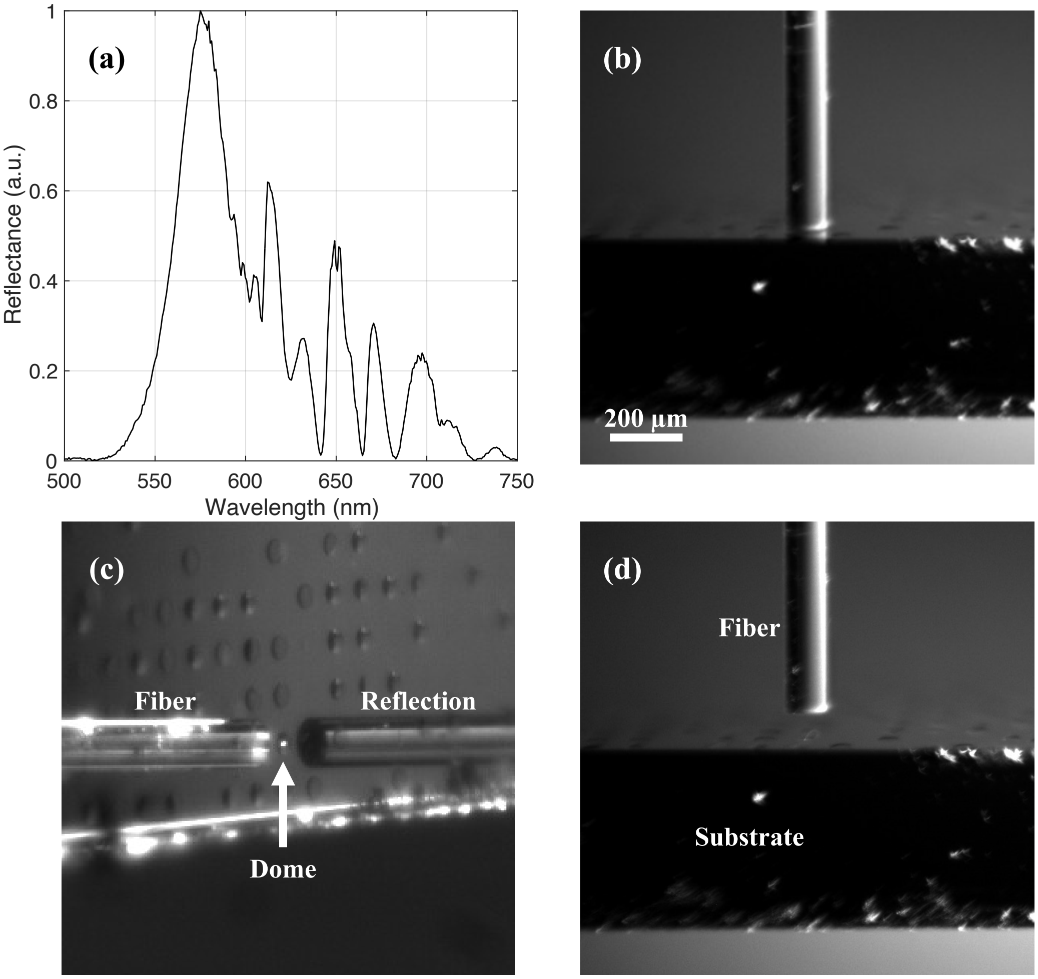

Fig. 5.10. Reflection measurements using a cleaved fiber and bidirectional coupler. **(a)** A reflection plot showing a family of cavity modes with the fundamental centered near 609 nm. **(b)** A camera view from the side showing the working distance required to obtain the measurement in (a). **(c)** A camera view with the fiber backed off to show the dome and potential cavity modes. **(d)** A camera view from the side with the fiber backed off showing with the location of the dome.

Unfortunately, we were unable to obtain convincing PL spectra showing cavity modes using the cleaved fiber measurement setup. The pump light could either be introduced through the primary input of the bidirectional coupler, or from the side at a glancing angle. Pumping through the fiber was problematic since autofluorescence from impurities within the fiber dominated the measurement and interacted with the cavity modes in the same fashion as light from the supercontinuum source in the reflection measurements. On the other hand, delivering significant power to the device under test when pumping at a glancing angle proved to be a challenge. In addition to the proximity of the cleaved fiber to the dome, it was significantly less efficient to pump at a sharp angle because of the angle-dependent reflectivity of the top mirror. Another problem was that the entire collection pathway was fiber coupled, meaning that residual pump light was directed into the spectrometer. This created a trade-off between integration time and pump power before saturation. Introducing a collimator and long-pass filter prior to the spectrometer eliminated this problem, but severely impacted coupling efficiency. Nevertheless, these measurements may still be possible with further refinements of the setup.

5.5 Conclusions

In summary, we have presented a promising way of integrating hexagonal boron nitride thin films into hemispherical optical cavities fabricated using thermally buckled Bragg mirrors. A novel method of obtaining reflection spectra was devised for measuring cavity modes, which might also be useful for measuring other highly directional optical resonators. We have also shown preliminary optical results in the form of photoluminescence imaging and spectra. However, undesired emission and fabrication issues still need to be accounted for.

Chapter 6 – Summary and Future Work

6.1 Summary

This thesis describes the integration of continuous hexagonal boron nitride films with various photonic devices in a comprehensive fashion that assumed no prior knowledge. It will hopefully serve as a stepping-stone for future emitter integration projects in the DeCorby lab.

The experimental work began in Chapter 3 with the design and construction of a photoluminescence spectroscope/microscope system that relied on a fiber pinhole to limit both the angular and spatial field of view. A critically important study on the autofluorescence properties of microscope objectives was then carried out to demonstrate the importance of accounting for system artifacts when making small-signal measurements. Spectral broadening resulting from critically stable Fabry-Perot cavities was also discussed as a problematic artifact that interferes with reflection and PL measurements.

With a reliable measurement system in place, Chapter 4 described the development of a centimeter-scale polymer-assisted hBN transfer process that inherently activated distinct emitters hosted in the material with success rates reaching > 80% measured by area. The optical properties of the resulting emitters were extensively characterized with the main conclusion being that the emission originating from regions corresponding to underlying substrate features was appreciably brighter than emission originating from luminescent wrinkles in the film.

Chapter 5 then focused on the integration of hexagonal boron nitride films with monolithic buckled microcavities and showed that it was indeed possible to induce thermal buckling on an hBN-embedded cavity. Photoluminescence imaging revealed that the cavity-enclosed hBN behaved as expected, with much of the emission localized to prepatterned features, though spectral measurements of buckled sites proved to be a challenge. A novel measurement scheme exploiting a standard cleaved 460HP fiber was also developed so that reflection measurements of buckled sites could be performed.

6.2 Future work

While this thesis has succeeded in showing that it is at least possible to integrate hexagonal boron nitride films into buckled microcavities, it has also shown the limitations of transferrable materials in the context of the type of devices fabricated by the DeCorby group. Most hBN-based integration schemes perform the hBN transfer as one of the final steps, or at least have minimal processing post-transfer [65–67,144]. The nature of buckled dome microcavities meant that the hBN needed to be introduced mid-process further reducing the overall yield. Another problem came from the buckling process which was heavily modified by both the introduction of etched holes and hBN, resulting in unfortunately low active device yield in many cases, especially since entire regions of hBN tended to buckle without patterning.

Several items need to be taken care of to ensure the success of quantum emitter integration into buckled dome microcavities for future projects. First, a second-order correlation measurement scheme needs to be integrated into the existing fluorescence spectroscopy/microscopy system. Such measurement schemes are not trivial but would permit the study of single emitters with confidence. A fast-steering mirror- or scanning stage-based system would also be advantageous as it would allow for PL spectra to be correlated with images easily. Second, the DeCorby group already has the necessary equipment to fully characterize buckled dome microcavities in the telecom wavelength range centered around 1550 nm. Additionally, much of the work involving buckled microcavities has historically taken place in this region so the materials and processing steps are well-understood. For example, a high-resolution tunable laser and photodetector could be used to characterize cavity resonances with fully resolved linewidths. The combination of an optical spectrum analyzer and spectrometer could then be used for photoluminescence measurements depending on the brightness of the individual emitters. Third, a method to fully localize emission needs to be conceived. While strain-activated emission from hBN has shown some success, nothing can be done to prevent emitters from randomly forming in other areas of the film during subsequent processing steps which generates a persistent background luminescence that obscures emission into cavity modes. This discovery suggests that specially trapping or patterning an emitting material might give more hope for success. If cavity-coupled emission from hBN is still desired, it may be worth considering a platelet in solution approach [38]. This method is highly suited for integration with buckled dome microcavities and would involve only minimal fine tuning of the thin-film optical design presented in Chapter 5 of this thesis. Patterned erbium or quantum dots would make excellent candidates for NIR devices.

Alternatively, the discovery that thin-film PTFE exhibits light fluorescence presents an interesting opportunity. **Figure 6.1** shows a representative photoluminescence measurement of patterned PTFE on silicon, fit to a Gaussian distribution, and is consistent with other accounts [145]. Some have shown that PTFE, albeit not Bosch-process Teflon, can be converted into nanodiamond films through controlled heating and cooling cycles induced by laser irradiation at specific wavelengths [146–148]. The DeCorby group already uses patterned PTFE films as low-adhesion layers, so there would theoretically be minimal processing involved in converting a portion of each PTFE pad into nanodiamond emitters.

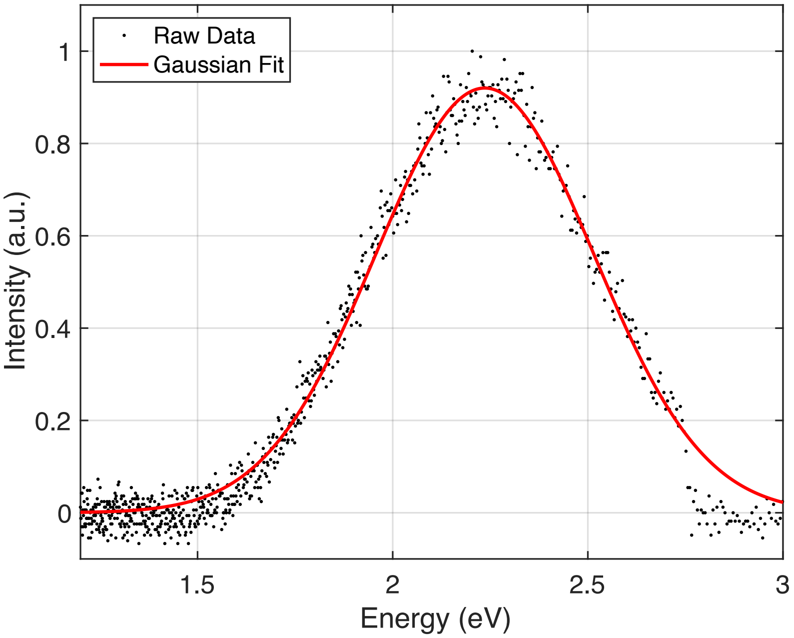

Fig. 6.1. A photoluminescence spectrum obtained from thin film PTFE. The Gaussian fit has a FWHM of 0.434 eV centered about 2.236 eV with $R^2 = 0.9874$.

Finally, the DeCorby group has recently demonstrated polarization dependence in elliptical buckled microcavities [149]. Once a fabrication process is established for integrating any emitter system into standard buckled microcavities it would be trivial to extend into elliptical variations. One use of such a system would involve pumping and collection in orthogonal planes while also ensuring all emitter photons are in the same polarization state. Additionally, there is typically a trade-off between a single photon source's efficiency and indistinguishability that could be addressed by such devices [150]. A device of this nature would be a significant contribution to the quantum optics community.

References

1. M. McConaughey, *Greenlights* (Crown Publishing Group, 2020).
2. Yongzhuo Li ; Hao Sun ; Lin Gan ; Jianxing Zhang ; Jiabin Feng ; Danyang Zhang ; Cun-Zheng Ning, "Optical Properties and Light-Emission Device Applications of 2-D Layered Semiconductors," Proc. IEEE 1–28 (2019).
3. A. K. Geim and K. S. Novoselov, "The rise of graphene," in *Nanoscience and Technology: A Collection of Reviews from Nature Journals* (2009).
4. P. Ajayan, P. Kim, and K. Banerjee, "Two-dimensional van der Waals materials," Phys. Today **69**, 38 (2016).
5. R. S. Sundaram, M. Engel, A. Lombardo, R. Krupke, A. C. Ferrari, P. Avouris, and M. Steiner, "Electroluminescence in single layer MoS2," Nano Lett. (2013).
6. O. Lopez-Sanchez, D. Lembke, M. Kayci, A. Radenovic, and A. Kis, "Ultrasensitive photodetectors based on monolayer MoS 2," Nat. Nanotechnol. (2013).
7. G. Wang, X. Marie, I. Gerber, T. Amand, D. Lagarde, L. Bouet, M. Vidal, A. Balocchi, and B. Urbaszek, "Giant Enhancement of the Optical Second-Harmonic Emission of WSe2 Monolayers by Laser Excitation at Exciton Resonances," Phys. Rev. Lett. (2015).
8. F. Withers, O. Del Pozo-Zamudio, A. Mishchenko, A. P. Rooney, A. Gholinia, K. Watanabe, T. Taniguchi, S. J. Haigh, A. K. Geim, A. I. Tartakovskii, and K. S. Novoselov, "Light-emitting diodes by band-structure engineering in van der Waals heterostructures," Nat. Mater. (2015).
9. N. F. Mott, "The basis of the electron theory of metals, with special reference to the transition metals," Proc. Phys. Soc. Sect. A (1949).
10. T. T. Tran, M. Kianinia, M. Nguyen, S. Kim, Z. Q. Xu, A. Kubanek, M. Toth, and I. Aharonovich, "Resonant Excitation of Quantum Emitters in Hexagonal Boron Nitride," ACS Photonics (2018).
11. J. D. Caldwell, I. Aharonovich, G. Cassabois, J. H. Edgar, B. Gil, and D. N. Basov, "Photonics with hexagonal boron nitride," Nat. Rev. Mater. **4**, 552–567 (2019).
12. H. S. Lee, M. S. Kim, Y. Jin, G. H. Han, Y. H. Lee, and J. Kim, "Selective Amplification of the Primary Exciton in a Mo S2 Monolayer," Phys. Rev. Lett. (2015).
13. T. T. Tran, D. Wang, Z. Q. Xu, A. Yang, M. Toth, T. W. Odom, and I. Aharonovich,

"Deterministic Coupling of Quantum Emitters in 2D Materials to Plasmonic Nanocavity Arrays," Nano Lett. **17**, 2634–2639 (2017).

14. Z. Eftekhari, Z. Eftekhari, A. Ghobadi, A. Ghobadi, M. C. Soydan, M. C. Soydan, D. U. Yildirim, D. U. Yildirim, N. Cinel, E. Ozbay, E. Ozbay, E. Ozbay, and E. Ozbay, "Strong light emission from a defective hexagonal boron nitride monolayer coupled to near-touching random plasmonic nanounits," Opt. Lett. Vol. 46, Issue 7, pp. 1664-1667 **46**, 1664–1667 (2021).
15. A. Kumar, M. A. Khan, and M. Kumar, "Recent advances in UV photodetectors based on 2D materials: a review," JPhD **55**, 133002 (2022).
16. J. Wu, G. K. W. Koon, D. Xiang, C. Han, C. T. Toh, E. S. Kulkarni, I. Verzhbitskiy, A. Carvalho, A. S. Rodin, S. P. Koenig, G. Eda, W. Chen, A. H. C. Neto, and B. Özyilmaz, "Colossal Ultraviolet Photoresponsivity of Few-Layer Black Phosphorus," ACS Nano **9**, 8070–8077 (2015).
17. K. Watanabe, T. Taniguchi, and H. Kanda, "Direct-bandgap properties and evidence for ultraviolet lasing of hexagonal boron nitride single crystal," (2004).
18. K. Watanabe and T. Taniguchi, "Hexagonal Boron Nitride as a New Ultraviolet Luminescent Material and Its Application," Int. J. Appl. Ceram. Technol. **8**, 977–989 (2011).
19. P. Jaffrennou, J. Barjon, J. S. Lauret, B. Attal-Trétout, F. Ducastelle, and A. Loiseau, "Origin of the excitonic recombinations in hexagonal boron nitride by spatially resolved cathodoluminescence spectroscopy," J. Appl. Phys. **102**, 116102 (2007).
20. M. Z. Bellus, M. Li, S. D. Lane, F. Ceballos, Q. Cui, X. C. Zeng, and H. Zhao, "Type-I van der Waals heterostructure formed by MoS2 and ReS2 monolayers," Nanoscale Horizons (2017).
21. B. Peng, G. Yu, X. Liu, B. Liu, X. Liang, L. Bi, L. Deng, T. C. Sum, and K. P. Loh, "Ultrafast charge transfer in MoS2/WSe2 p-n Heterojunction," 2D Mater. (2016).
22. F. Withers, O. Del Pozo-Zamudio, S. Schwarz, S. Dufferwiel, P. M. Walker, T. Godde, A. P. Rooney, A. Gholinia, C. R. Woods, P. Blake, S. J. Haigh, K. Watanabe, T. Taniguchi, I. L. Aleiner, A. K. Geim, V. I. Fal'Ko, A. I. Tartakovskii, and K. S. Novoselov, "WSe2 Light-Emitting Tunneling Transistors with Enhanced Brightness at Room Temperature," Nano Lett. (2015).

23. M. Li, M. Z. Bellus, J. Dai, L. Ma, X. Li, H. Zhao, and X. C. Zeng, "A type-I van der Waals heterobilayer of WSe2/MoTe2," Nanotechnology **29**, (2018).

24. N. V. Proscia, Z. Shotan, H. Jayakumar, P. Reddy, C. Cohen, M. Dollar, A. Alkauskas, M. Doherty, C. A. Meriles, and V. M. Menon, "Near-deterministic activation of room-temperature quantum emitters in hexagonal boron nitride," Optica **5**, 1128–1134 (2018).

25. M. Toth and I. Aharonovich, "Single Photon Sources in Atomically Thin Materials," Annu. Rev. Phys. Chem. (2019).

26. P. Tonndorf, R. Schmidt, R. Schneider, J. Kern, M. Buscema, G. A. Steele, A. Castellanos-Gomez, H. S. J. van der Zant, S. Michaelis de Vasconcellos, and R. Bratschitsch, "Single-photon emission from localized excitons in an atomically thin semiconductor," Optica (2015).

27. J. Ziegler, R. Klaiss, A. Blaikie, D. Miller, V. R. Horowitz, and B. J. Alemán, "Deterministic Quantum Emitter Formation in Hexagonal Boron Nitride via Controlled Edge Creation," Nano Lett. **19**, 2121–2127 (2019).

28. J. Klein, L. Sigl, S. Gyger, K. Barthelmi, M. Florian, S. Rey, T. Taniguchi, K. Watanabe, F. Jahnke, C. Kastl, V. Zwiller, K. D. Jöns, K. Müller, U. Wurstbauer, J. J. Finley, and A. W. Holleitner, "Scalable single-photon sources in atomically thin MoS 2," (n.d.).

29. N. Gregersen, D. P. S. McCutcheon, and J. Mørk, "Single-photon sources," in *Handbook of Optoelectronic Device Modeling and Simulation: Lasers, Modulators, Photodetectors, Solar Cells, and Numerical Methods* (2017).

30. T. Vogl, R. Lecamwasam, B. C. Buchler, Y. Lu, and P. K. Lam, "Compact Cavity-Enhanced Single-Photon Generation with Hexagonal Boron Nitride," ACS Photonics (2019).

31. K. S. Novoselov, A. K. Geim, S. V. Morozov, D. Jiang, Y. Zhang, S. V. Dubonos, I. V. Grigorieva, and A. A. Firsov, "Electric field in atomically thin carbon films," Science (80-.). **306**, 666–669 (2004).

32. L. H. Li, Y. Chen, G. Behan, H. Zhang, M. Petravic, and A. M. Glushenkov, "Large-scale mechanical peeling of boron nitride nanosheets by low-energy ball milling," J. Mater. Chem. **21**, 11862–11866 (2011).

33. Y. Zhou, L. Hu, and G. Grüner, "A method of printing carbon nanotube thin films," Appl. Phys. Lett. (2006).

34. Y. Lee, S. Bae, H. Jang, S. Jang, S. E. Zhu, S. H. Sim, Y. Il Song, B. H. Hong, and J. H. Ahn, "Wafer-scale synthesis and transfer of graphene films," Nano Lett. (2010).

35. A. Reina, X. Jia, J. Ho, D. Nezich, H. Son, V. Bulovic, M. S. Dresselhaus, and K. Jing, "Large area, few-layer graphene films on arbitrary substrates by chemical vapor deposition," Nano Lett. (2009).

36. N. S. Taghavi, P. Gant, P. Huang, I. Niehues, R. Schmidt, S. Michaelis de Vasconcellos, R. Bratschitsch, M. García-Hernández, R. Frisenda, and A. Castellanos-Gomez, "Thickness determination of MoS2, MoSe2, WS2 and WSe2 on transparent stamps used for deterministic transfer of 2D materials," Nano Res. (2019).

37. Q.-H. Tan, J.-M. Lai, X.-L. Liu, Y.-Z. Xue, X.-M. Dou, B.-Q. Sun, W.-B. Gao, P.-H. Tan, and J. Zhang, "Robust Ultraviolet to Near-infrared Quantum Emitters in Hexagonal Boron Nitride up to 1100 K," (n.d.).

38. J. A. Preuß, E. Rudi, J. Kern, R. Schmidt, R. Bratschitsch, and S. M. de Vasconcellos, "Assembly of large hBN nanocrystal arrays for quantum light emission," 2D Mater. **8**, 035005 (2021).

39. E. T. Yu, C. Hu, M. Kim, K. Yeol Ma, and H. Suk Shin, "Toward growth of wafer-scale single-crystal hexagonal boron nitride sheets," Nano Express **2**, 031004 (2021).

40. J. S. Lee, S. H. Choi, S. J. Yun, Y. I. Kim, S. Boandoh, J. H. Park, B. G. Shin, H. Ko, S. H. Lee, Y. M. Kim, Y. H. Lee, K. K. Kim, and S. M. Kim, "Wafer-scale single-crystal hexagonal boron nitride film via self-collimated grain formation," Science (80-.). **362**, 817–821 (2018).

41. K. Ahmed, R. Dahal, A. Weltz, J. J. Q. Lu, Y. Danon, and I. B. Bhat, "Effects of sapphire nitridation and growth temperature on the epitaxial growth of hexagonal boron nitride on sapphire," Mater. Res. Express **4**, 015007 (2017).

42. A. Castellanos-Gomez, M. Buscema, R. Molenaar, V. Singh, L. Janssen, H. S. J. Van Der Zant, and G. A. Steele, "Deterministic transfer of two-dimensional materials by all-dry viscoelastic stamping," 2D Mater. **1**, 011002 (2014).

43. T. T. Tran, K. Bray, M. J. Ford, M. Toth, and I. Aharonovich, "Quantum emission from hexagonal boron nitride monolayers," Nat. Nanotechnol. (2016).

44. M. Nguyen, S. Kim, T. T. Tran, Z. Q. Xu, M. Kianinia, M. Toth, and I. Aharonovich, "Nanoassembly of quantum emitters in hexagonal boron nitride and gold nanospheres,"

Nanoscale **10**, 2267–2274 (2018).

45. A. Bommer and C. Becher, "New insights into nonclassical light emission from defects in multi-layer hexagonal boron nitride," Nanophotonics **8**, 2041–2048 (2019).
46. F. Hayee, L. Yu, J. Linda Zhang, C. J. Ciccarino, M. Nguyen, A. F. Marshall, I. Aharonovich, J. Vučković, P. Narang, T. F. Heinz, and J. A. Dionne, "Revealing multiple classes of stable quantum emitters in hexagonal boron nitride with correlated optical and electron microscopy," (n.d.).
47. S. Hou, M. D. Birowosuto, S. Umar, M. A. Anicet, R. Y. Tay, P. Coquet, B. K. Tay, H. Wang, and E. H. T. Teo, "Localized emission from laser-irradiated defects in 2D hexagonal boron nitride," 2D Mater. **5**, 015010 (2017).
48. V. Shautsova, A. M. Gilbertson, N. C. G. Black, S. A. Maier, and L. F. Cohen, "Hexagonal Boron Nitride assisted transfer and encapsulation of large area CVD graphene," Sci. Rep. **6**, 1–8 (2016).
49. M. Gurram, S. Omar, S. Zihlmann, P. Makk, Q. C. Li, Y. F. Zhang, C. Schönenberger, and B. J. Van Wees, "Spin transport in two-layer-CVD-hBN/graphene/hBN heterostructures," Phys. Rev. B **97**, 045411 (2018).
50. K. K. Kim, A. Hsu, X. Jia, S. M. Kim, Y. Shi, M. Dresselhaus, T. Palacios, and J. Kong, "Synthesis and Characterization of Hexagonal Boron Nitride Film as a Dielectric Layer for Graphene Devices," ACS Nano **6**, 8583–8590 (2012).
51. N. Bernhardt, N. Bernhardt, S. Kim, S. Kim, J. E. Fröch, S. J. U. White, N. M. H. Duong, Z. He, B. Chen, J. Liu, I. Aharonovich, I. Aharonovich, A. S. Solntsev, and A. S. Solntsev, "Large few-layer hexagonal boron nitride flakes for nonlinear optics," Opt. Lett. Vol. 46, Issue 3, pp. 564-567 **46**, 564–567 (2021).
52. G. Hajisalem, M. S. Shariatdoust, R. F. Ali, B. D. Gates, P. E. Barclay, and R. Gordon, "Single Nanoflake Hexagonal Boron Nitride Harmonic Generation with Ultralow Pump Power," ACS Photonics **8**, 1922–1926 (2021).
53. N. Mendelson, D. Chugh, J. R. Reimers, T. S. Cheng, A. Gottscholl, H. Long, C. J. Mellor, A. Zettl, V. Dyakonov, P. H. Beton, S V Novikov, C. Jagadish, H. Hoe Tan, M. J. Ford, M. Toth, C. Bradac, and I. Aharonovich, "Identifying carbon as the source of visible single-photon emission from hexagonal boron nitride," Nat. Mater. (n.d.).
54. A. Sajid and K. S. Thygesen, "VNCB defect as source of single photon emission from

hexagonal boron nitride," 2D Mater. **7**, 31007 (2020).

55. S. A. Tawfik, S. Ali, M. Fronzi, M. Kianinia, T. T. Tran, C. Stampfl, I. Aharonovich, M. Toth, and M. J. Ford, "First-principles investigation of quantum emission from hBN defects," Nanoscale (2017).
56. Z. Q. Xu, C. Elbadawi, T. T. Tran, M. Kianinia, X. Li, D. Liu, T. B. Hoffman, M. Nguyen, S. Kim, J. H. Edgar, X. Wu, L. Song, S. Ali, M. Ford, M. Toth, and I. Aharonovich, "Single photon emission from plasma treated 2D hexagonal boron nitride," Nanoscale **10**, 7957–7965 (2018).
57. K. G. Scheuer, G. J. Hornig, and R. G. DeCorby, "Polymer transfer technique for strain-activated emission in hexagonal boron nitride," Opt. Express **29**, 26103 (2021).
58. R. Wang, J. Yang, X. Wu, and S. Wang, "Local charge states in hexagonal boron nitride with Stone–Wales defects," Nanoscale **8**, 8210–8219 (2016).
59. J. Ziegler, A. Blaikie, A. Fathalizadeh, D. Miller, F. S. Yasin, K. Williams, J. Mohrhardt, B. J. McMorran, A. Zettl, and B. Alemán, "Single-Photon Emitters in Boron Nitride Nanococoons," Nano Lett. **18**, 2683–2688 (2018).
60. W. Liu, Y.-T. Wang, Z.-P. Li, S. Yu, Z.-J. Ke, Y. Meng, J.-S. Tang, C.-F. Li, and G.-C. Guo, "An ultrastable and robust single-photon emitter in hexagonal boron nitride," (n.d.).
61. N. Chejanovsky, Y. Kim, A. Zappe, B. Stuhlhofer, T. Taniguchi, K. Watanabe, D. Dasari, A. Finkler, J. H. Smet, and J. Wrachtrup, "Quantum Light in Curved Low Dimensional Hexagonal Boron Nitride Systems," Sci. Reports 2017 71 **7**, 1–14 (2017).
62. X. Xu, Z. O. Martin, D. Sychev, A. S. Lagutchev, Y. P. Chen, T. Taniguchi, K. Watanabe, V. M. Shalaev, and A. Boltasseva, "Creating Quantum Emitters in Hexagonal Boron Nitride Deterministically on Chip-Compatible Substrates," Nano Lett. **21**, 8182–8189 (2021).
63. M. Fox, *Quantum Optics: An Introduction* (Oxford University Press, 2006).
64. S. Kim, J. E. Fröch, J. Christian, M. Straw, J. Bishop, D. Totonjian, K. Watanabe, T. Taniguchi, M. Toth, and I. Aharonovich, "Photonic crystal cavities from hexagonal boron nitride," Nat. Commun. 2018 91 **9**, 1–8 (2018).
65. J. E. Fröch, S. Kim, N. Mendelson, M. Kianinia, M. Toth, M. Toth, I. Aharonovich, and I. Aharonovich, "Coupling Hexagonal Boron Nitride Quantum Emitters to Photonic Crystal Cavities," ACS Nano **14**, 7085–7091 (2020).

66. S. Häußler, G. Bayer, R. Waltrich, N. Mendelson, C. Li, D. Hunger, I. Aharonovich, and A. Kubanek, "Tunable Fiber-Cavity Enhanced Photon Emission from Defect Centers in hBN," Adv. Opt. Mater. **9**, (2021).
67. N. V. Proscia, H. Jayakumar, X. Ge, G. Lopez-Morales, Z. Shotan, W. Zhou, C. A. Meriles, and V. M. Menon, "Microcavity-coupled emitters in hexagonal boron nitride," Nanophotonics **9**, 2937–2944 (2020).
68. G. J. Hornig, S. Al-Sumaidae, J. Maldaner, L. Bu, and R. G. Decorby, "Monolithically integrated membrane-in-the-middle cavity optomechanical systems," Opt. Express **28**, 28113 (2020).
69. J. Maldaner, J. Maldaner, S. Al-Sumaidae, S. Al-Sumaidae, G. J. Hornig, L. J. LeBlanc, and R. G. DeCorby, "Liquid infiltration of monolithic open-access Fabry–Perot microcavities," Appl. Opt. Vol. 59, Issue 23, pp. 7125-7130 **59**, 7125–7130 (2020).
70. C. A. Potts, A. Melnyk, H. Ramp, M. H. Bitarafan, D. Vick, L. J. LeBlanc, J. P. Davis, and R. G. DeCorby, "Tunable open-access microcavities for on-chip cavity quantum electrodynamics," Appl. Phys. Lett. **108**, 041103 (2016).
71. S. Al-Sumaidae, S. Al-Sumaidae, L. Bu, G. J. Hornig, M. H. Bitarafan, and R. G. DeCorby, "Pressure sensing with high-finesse monolithic buckled-dome microcavities," Appl. Opt. Vol. 60, Issue 29, pp. 9219-9224 **60**, 9219–9224 (2021).
72. "Luminescence of Solids," Lumin. Solids (1998).
73. P. W. Atkins, "Physical Chemistry, 6th ed," Oxford Univ. Press. Oxford 806 (1998).
74. J. R. Lakowicz, *Principles of Fluorescence Spectroscopy* (Springer, 2006).
75. K. L. Wong, J. C. G. Bünzli, and P. A. Tanner, "Quantum yield and brightness," J. Lumin. **224**, 117256 (2020).
76. J. Laverdant, W. Daney De Marcillac, C. Barthou, V. D. Chinh, C. Schwob, L. Coolen, P. Benalloul, P. T. Nga, and A. M. Maˆıtre, "Experimental Determination of the Fluorescence Quantum Yield of Semiconductor Nanocrystals," Materials (Basel). **4**, 1182–1193 (2011).
77. O. Labeau, P. Tamarat, and B. Lounis, "Temperature Dependence of the Luminescence Lifetime of Single CdSe/ZnS Quantum Dots," Phys. Rev. Lett. **90**, 4 (2003).
78. C. A. Leatherdale, W. K. Woo, F. V. Mikulec, and M. G. Bawendi, "On the absorption cross section of CdSe nanocrystal quantum dots," J. Phys. Chem. B **106**, 7619–7622

(2002).

79. M. Amani, D. H. Lien, D. Kiriya, J. Xiao, A. Azcatl, J. Noh, S. R. Madhvapathy, R. Addou, K. C. Santosh, M. Dubey, K. Cho, R. M. Wallace, S. C. Lee, J. H. He, J. W. Ager, X. Zhang, E. Yablonovitch, and A. Javey, "Near-unity photoluminescence quantum yield in MoS2," Science (80-.). (2015).

80. Y. Hoshi, T. Kuroda, M. Okada, R. Moriya, S. Masubuchi, K. Watanabe, T. Taniguchi, R. Kitaura, and T. Machida, "Suppression of exciton-exciton annihilation in tungsten disulfide monolayers encapsulated by hexagonal boron nitrides," Phys. Rev. B (2017).

81. T. Korn, S. Heydrich, M. Hirmer, J. Schmutzler, and C. Schller, "Low-temperature photocarrier dynamics in monolayer MoS2," Appl. Phys. Lett. (2011).

82. B. Lounis and M. Orrit, "Single-photon sources," Reports Prog. Phys. (2005).

83. M. Koperski, K. Nogajewski, and M. Potemski, "Single photon emitters in boron nitride: More than a supplementary material," Opt. Commun. **411**, 158–165 (2018).

84. T. Feldtmann, M. Kira, and S. W. Koch, "Phonon sidebands in semiconductor luminescence," Phys. Status Solidi Basic Res. **246**, 332–336 (2009).

85. S. O. Kasap, *Principles of Electronic Materials and Devices*, Fourth Edi (McGraw-Hill, 2018).

86. B. Xu, M. Lv, X. Fan, W. Zhang, Y. Xu, and T. Zhai, "Lattice parameters of hexagonal and cubic boron nitrides at high temperature and high pressure," Integr. Ferroelectr. **162**, 85–93 (2015).

87. S. O. Kasap, "Optoelectronics and Photonics: Principles and Practices (2nd Edition) Chapter 1," Optoelectron. Photonics Princ. Pract. (2nd Ed. Chapter 1 (2012).

88. P. Yeh, *Optical Waves in Layered Media (Pure & Applied Optics)* (Wiley-Interscience, 1988).

89. L. R. Brovelli and U. Keller, "Simple analytical expressions for the reflectivity and the penetration depth of a Bragg mirror between arbitrary media," Opt. Commun. **116**, 343–350 (1995).

90. J. Moon and A. M. Shkel, "Analysis of imperfections in a micromachined tunable-cavity interferometer," Smart Struct. Mater. 2001 Smart Electron. MEMS **4334**, 46 (2001).

91. J. Verdeyen, *Laser Electronics*, 3rd editio (Pearson, 1994).

92. "File:Laguerre-gaussian.png - Wikimedia Commons,"

https://commons.wikimedia.org/wiki/File:Laguerre-gaussian.png.

93. "File:Hermite-gaussian.png - Wikimedia Commons," https://commons.wikimedia.org/wiki/File:Hermite-gaussian.png.

94. A. Yariv, *Optical Electronics* (Saunders College Pub, 1991).

95. M. H. Bitarafan and R. G. DeCorby, "Small-mode-volume, channel-connected Fabr Perot microcavities on a chip," Appl. Opt. Vol. 56, Issue 36, pp. 9992-9997 **56**, 9992–9997 (2017).

96. B. W. Shore and P. L. Knight, "The Jaynes–Cummings model," J. Mod. Opt. **40**, 1195–1238 (1993).

97. C. Chakraborty, N. Vamivakas, and D. Englund, "Advances in quantum light emission from 2D materials," Nanophotonics **8**, 2017–2032 (2019).

98. L. J. Martínez, T. Pelini, V. Waselowski, J. R. Maze, B. Gil, G. Cassabois, and V. Jacques, "Efficient single photon emission from a high-purity hexagonal boron nitride crystal," Phys. Rev. B **94**, 121405 (2016).

99. H. Gross, O. Rodenko, X. Lu, and Y. Zhang, "Efficient simulation of autofluorescence effects in microscope lenses," Appl. Opt. Vol. 58, Issue 13, pp. 3589-3596 **58**, 3589–3596 (2019).

100. H. Gross, X. Lu, and Y. Zhang, "General analysis and optimization strategy to suppress autofluorescence in microscope lenses," Appl. Opt. Vol. 58, Issue 27, pp. 7404-7415 **58**, 7404–7415 (2019).

101. J. Grace, S. Edlou, J. Foss, C. Hodgson, J. P. Rheault, J. Rosvold, K. Sieber, and S. Walters, "Using optical interference filters to measure autofluorescence in substrates and coatings," Surf. Coatings Technol. **426**, 127777 (2021).

102. K. Visscher, G. J. Brakenhoff, and T. D. Visser, "Fluorescence saturation in confocal microscopy," J. Microsc. **175**, 162–165 (1994).

103. A. Sidike, I. Kusachi, and N. Yamashita, "Natural fluorite emitting yellow fluorescence under UV light," Phys. Chem. Miner. 2003 308 **30**, 478–485 (2003).

104. K. Kurata, "Objective Lens," U.S. patent US6822805B2 (November 18, 2002).

105. Schott, *TIE-36 : Fluorescence of Optical Glass* (2004).

106. H. E. Keller, "Objective lenses for confocal microscopy," in *Handbook of Biological Confocal Microscopy: Third Edition* (2006), pp. 145–161.

107. R. C. Linares, "Fluorescent Properties of Trivalent Rare Earths in Fluorite Structure Oxides*," JOSA, Vol. 56, Issue 12, pp. 1700-1702 **56**, 1700–1702 (1966).

108. R. C. Burruss, T. G. Ging, R. G. Eppinger, and ain M. Samson, "Laser-excited fluorescence of rare earth elements in fluorite: Initial observations with a laser Raman microprobe," Geochim. Cosmochim. Acta **56**, 2713–2723 (1992).

109. H. Lin, D. Yang, G. Liu, T. Ma, B. Zhai, Q. An, J. Yu, X. Wang, X. Liu, and E. Yue-Bun Pun, "Optical absorption and photoluminescence in Sm3+- and Eu 3+-doped rare-earth borate glasses," J. Lumin. **113**, 121–128 (2005).

110. V. B. Bozhilov, E. E. Bubev, S. V. Kozhukharov, M. Machkova, V. Kozhukharov, and C. R. Georgiev, "Optical Properties of Glasses in the System," J. Int. Sci. Publ. **8**, 322–327 (2014).

111. E. Diamanti, H. K. Lo, B. Qi, and Z. Yuan, "Practical challenges in quantum key distribution," npj Quantum Inf. (2016).

112. X. Ma, N. F. Hartmann, J. K. S. Baldwin, S. K. Doorn, and H. Htoon, "Room-temperature single-photon generation from solitary dopants of carbon nanotubes," Nat. Nanotechnol. (2015).

113. P. Michler, A. Kiraz, C. Becher, W. V. Schoenfeld, P. M. Petroff, L. Zhang, E. Hu, and A. Imamoğlu, "A quantum dot single-photon turnstile device," Science (80-.). (2000).

114. T. Schröder, F. Gädeke, M. J. Banholzer, and O. Benson, "Ultrabright and efficient single-photon generation based on nitrogen-vacancy centres in nanodiamonds on a solid immersion lens," New J. Phys. (2011).

115. H. G. Barros, A. Stute, T. E. Northup, C. Russo, P. O. Schmidt, and R. Blatt, "Deterministic single-photon source from a single ion," New J. Phys. (2009).

116. G. Grosso, H. Moon, B. Lienhard, S. Ali, D. K. Efetov, M. M. Furchi, P. Jarillo-Herrero, M. J. Ford, I. Aharonovich, and D. Englund, "Tunable and high-purity room temperature single-photon emission from atomic defects in hexagonal boron nitride," Nat. Commun. **8**, 705 (2017).

117. A. W. Schell, M. Svedendahl, and R. Quidant, "Quantum Emitters in Hexagonal Boron Nitride Have Spectrally Tunable Quantum Efficiency," Adv. Mater. **30**, 1704237 (2018).

118. N. Nikolay, N. Mendelson, E. Özelci, B. Sontheimer, F. Böhm, G. Kewes, M. Toth, I. Aharonovich, and O. Benson, "Direct measurement of quantum efficiency of single-

photon emitters in hexagonal boron nitride," Optica **6**, 1084 (2019).

119. M. Kianinia, S. White, J. E. Fröch, C. Bradac, and I. Aharonovich, "Generation of Spin Defects in Hexagonal Boron Nitride," ACS Photonics **7**, 2147–2152 (2020).

120. A. Gottscholl, M. Kianinia, V. Soltamov, C. Bradac, C. Kasper, K. Krambrock, A. Sperlich, M. Toth, I. Aharonovich, and V. Dyakonov, *Room Temperature Initialisation and Readout of Intrinsic Spin Defects in a Van Der Waals Crystal* (n.d.).

121. M. Hoese, P. Reddy, A. Dietrich, M. K. Koch, K. G. Fehler, M. W. Doherty, and A. Kubanek, "Mechanical decoupling of quantum emitters in hexagonal boron nitride from low-energy phonon modes," Sci. Adv. (2020).

122. T. T. Tran, K. Bray, M. J. Ford, M. Toth, and I. Aharonovich, "Quantum emission from hexagonal boron nitride monolayers," Nat. Nanotechnol. (2016).

123. A. Gottscholl, M. Kianinia, V. Soltamov, S. Orlinskii, G. Mamin, C. Bradac, C. Kasper, K. Krambrock, A. Sperlich, M. Toth, I. Aharonovich, and V. Dyakonov, "Initialization and read-out of intrinsic spin defects in a van der Waals crystal at room temperature," Nat. Mater. (2020).

124. W. Liu, Z.-P. Li, Y.-Z. Yang, S. Yu, Y. Meng, Z.-A. Wang, N.-J. Guo, F.-F. Yan, Q. Li, J.-F. Wang, J.-S. Xu, Y. Dong, X.-D. Chen, F.-W. Sun, Y.-T. Wang, J.-S. Tang, C.-F. Li, and G.-C. Guo, *Rabi Oscillation of* $V - B$ *Spin in Hexagonal Boron Nitride* (2021).

125. T. Vogl, G. Campbell, B. C. Buchler, Y. Lu, and P. K. Lam, "Fabrication and Deterministic Transfer of High-Quality Quantum Emitters in Hexagonal Boron Nitride," ACS Photonics (2018).

126. A. L. Exarhos, D. A. Hopper, R. R. Grote, A. Alkauskas, and L. C. Bassett, "Optical Signatures of Quantum Emitters in Suspended Hexagonal Boron Nitride," ACS Nano (2017).

127. A. Gurarslan, Y. Yu, L. Su, Y. Yu, F. Suarez, S. Yao, Y. Zhu, M. Ozturk, Y. Zhang, and L. Cao, "Surface-energy-assisted perfect transfer of centimeter-scale monolayer and few-layer MoS2 films onto arbitrary substrates," ACS Nano (2014).

128. N. Mendelson, Z. Q. Xu, T. T. Tran, M. Kianinia, J. Scott, C. Bradac, I. Aharonovich, and M. Toth, "Engineering and Tuning of Quantum Emitters in Few-Layer Hexagonal Boron Nitride," ACS Nano (2019).

129. C. Li, N. Mendelson, R. Ritika, Y.-L. Chen, Z.-Q. Xu, M. Toth, and I. Aharonovich,

"Scalable and Deterministic Fabrication of Quantum Emitter Arrays from Hexagonal Boron Nitride," (2021).

130. K. Qian, R. Y. Tay, V. C. Nguyen, J. Wang, G. Cai, T. Chen, E. H. T. Teo, and P. S. Lee, "Hexagonal Boron Nitride Thin Film for Flexible Resistive Memory Applications," Adv. Funct. Mater. **26**, 2176–2184 (2016).
131. B. Spokoyny, H. Utzat, H. Moon, G. Grosso, D. Englund, and M. G. Bawendi, "Effect of Spectral Diffusion on the Coherence Properties of a Single Quantum Emitter in Hexagonal Boron Nitride," J. Phys. Chem. Lett **11**, 47 (2020).
132. M. A. Feldman, A. Puretzky, L. Lindsay, E. Tucker, D. P. Briggs, P. G. Evans, R. F. Haglund, and B. J. Lawrie, "Phonon-induced multicolor correlations in hBN single-photon emitters," Phys. Rev. B **99**, (2019).
133. Z. Shotan, H. Jayakumar, C. R. Considine, M. Mackoit, H. Fedder, J. Wrachtrup, A. Alkauskas, M. W. Doherty, V. M. Menon, and C. A. Meriles, "Photoinduced Modification of Single-Photon Emitters in Hexagonal Boron Nitride," ACS Photonics **3**, 2490–2496 (2016).
134. I. Aharonovich, D. Englund, and M. Toth, "Solid-state single-photon emitters," Nat. Photonics (2016).
135. S. Takeuchi, "Recent progress in single-photon and entangled-photon generation and applications," (2014).
136. C. Fournier, A. Plaud, S. Roux, A. Pierret, M. Rosticher, K. Watanabe, T. Taniguchi, S. Buil, X. Quélin, J. Barjon, J.-P. Hermier, and A. Delteil, "Position-controlled quantum emitters with reproducible emission wavelength in hexagonal boron nitride," (n.d.).
137. H. Akbari, W.-H. Lin, B. Vest, P. K. Jha, H. A. Atwater, and T. J. Watson, "Temperature-dependent Spectral Emission of Hexagonal Boron Nitride Quantum Emitters on Conductive and Dielectric Substrates," Phys. Rev. Appl. **10**, 14036 (2021).
138. N. Lassaline, D. Thureja, T. Chervy, D. Petter, P. A. Murthy, A. W. Knoll, and D. J. Norris, "Freeform Electronic and Photonic Landscapes in Hexagonal Boron Nitride," Nano Lett. **4**, 29 (2021).
139. Q. T. Nanyang, T. Unviersity, J.-M. Lai, D. Guo, Y.-Z. Xue, X.-M. Dou, B.-Q. Sun, H.-X. Deng, I. Aharonovich, and J. Zhang, "Donor-Acceptor Pair Quantum Emitters in Hexagonal Boron Nitride," (2021).

140. C. Jara, T. Rauch, S. Botti, M. A. L. Marques, A. Norambuena, R. Coto, J. E. Castellanos-Águila, J. R. Maze, and F. Munoz, "First-Principles Identification of Single Photon Emitters Based on Carbon Clusters in Hexagonal Boron Nitride," J. Phys. Chem. A **125**, 1325–1335 (2021).

141. T. Tashima, H. Takashima, A. W. Schell, S. Takeuchi, T. T. Tran, and I. Aharonovich, "Hybrid Device of Hexagonal Boron Nitride Nanooakes with Defect Centres and a Nano-Fibre Bragg Cavity Hybrid device of hexagonal boron nitride nanoflakes with defect centres and a nano-fibre Bragg cavity," (2021).

142. A. Ghobadi, D. U. Yildirim, E. Ozbay, M. C. Soydan, N. Cinel, Z. Eftekhari, D. U. Yildirim, D. U. Yildirim, N. Cinel, E. Ozbay, E. Ozbay, E. Ozbay, and E. Ozbay, "Strong light emission from a defective hexagonal boron nitride monolayer coupled to near-touching random plasmonic nanounits," Opt. Lett. Vol. 46, Issue 7, pp. 1664-1667 **46**, 1664–1667 (2021).

143. C. A. Potts, A. Melnyk, H. Ramp, M. H. Bitarafan, D. Vick, L. J. LeBlanc, J. P. Davis, and R. G. DeCorby, "Tunable open-access microcavities for on-chip cavity quantum electrodynamics," Appl. Phys. Lett. **108**, 041103 (2016).

144. P. K. Shandilya, J. E. Fröch, M. Mitchell, D. P. Lake, S. Kim, M. Toth, B. Behera, C. Healey, I. Aharonovich, and P. E. Barclay, "Hexagonal Boron Nitride Cavity Optomechanics," Nano Lett. **19**, 1343–1350 (2019).

145. A. Scanni, A. Valentini, G. Perna, V. Capozzi, and A. Convertino, "Photoluminescence analysis on Teflon bulk and Teflon-like films grown by Ion-beam sputtering," J. Lumin. **91**, 87–90 (2000).

146. R. Ye, X. Han, D. V. Kosynkin, Y. Li, C. Zhang, B. Jiang, A. A. Martí, and J. M. Tour, "Laser-Induced Conversion of Teflon into Fluorinated Nanodiamonds or Fluorinated Graphene," ACS Nano **12**, 1083–1088 (2018).

147. S. Gupta and J. Narayan, "Direct conversion of Teflon into nanodiamond films," http://mc.manuscriptcentral.com/tmrl **8**, 408–416 (2020).

148. P. Joshi, P. Riley, S. Gupta, R. J. Narayan, and J. Narayan, "Advances in laser-assisted conversion of polymeric and graphitic carbon into nanodiamond films," Nanotechnology **32**, 432001 (2021).

149. G. Hornig, R. DeCorby, L. Bu, and S. Alsumaidae, "Monolithic elliptical dome Fabry-

Perot microcavities exhibiting large birefringence," J. Opt. Soc. Am. B (2022).

150. H. Wang, Y. M. He, T. H. Chung, H. Hu, Y. Yu, S. Chen, X. Ding, M. C. Chen, J. Qin, X. Yang, R. Z. Liu, Z. C. Duan, J. P. Li, S. Gerhardt, K. Winkler, J. Jurkat, L. J. Wang, N. Gregersen, Y. H. Huo, Q. Dai, S. Yu, S. Höfling, C. Y. Lu, and J. W. Pan, "Towards optimal single-photon sources from polarized microcavities," Nat. Photonics 2019 1311 **13**, 770–775 (2019).

151. G. R. Araujo, T. Pollmann, and A. Ulrich, "Photoluminescence response of acrylic (PMMA) and polytetrafluoroethylene (PTFE) to ultraviolet light," Eur. Phys. J. C 2019 798 **79**, 1–8 (2019).

Appendix A – Isolated microscope photoluminescence

To further demonstrate that the persistent photoluminescence signal was attributable to the objective lenses a secondary experiment was performed that involved isolating the lenses from other components within the epifluorescence system. In this case, the excitation laser was filtered using the same short pass filter set described in the main text and passed directly into the collection side of the objective under test. Two long pass filters (both Thorlabs FELH0450) were placed immediately after the exit pupil of the objective to filter pump light. The photoluminescence signal was collected using a standard small-format collimator (Thorlabs) and passed into the Ocean Optics QEPro spectrometer with a 600 µm core fiber (Thorlabs). Spectra collected using a pump power of ~ 100 mW and integration time of 1 second are presented in **Fig. A.1** along with a schematic of the measurement setup. The data is again presented as measured.

Removing extraneous optical elements from the measurement such as the dichroic mirror, beamsplitter, and fiber pinhole provided a more direct measurement of the objective lens luminescence and shows that spectral features centered near 600 nm and 650 nm are generally present across photoluminescence signal collected from each objective lens. Additionally, no detectable signal is present without an objective in place, as shown in **Fig. A.1**(b).

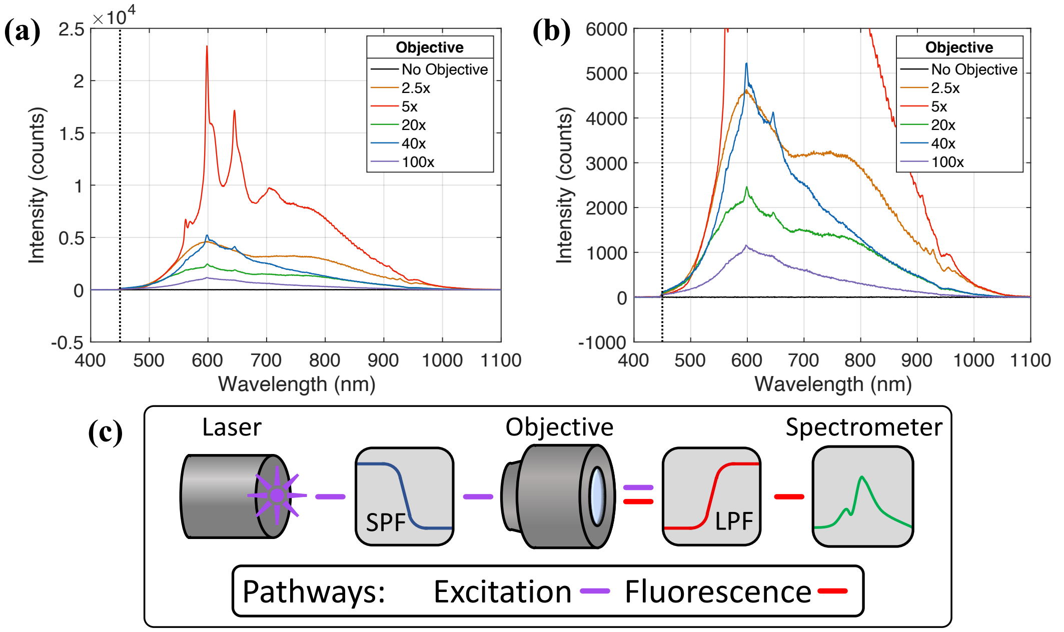

Fig. A.1. Direct measurements of photoluminescence from the microscope objectives in **Table 3.2**. **(a)** Measurements for each objective subject to ~ 100 mW of power captured using an integration time of 1 second. **(b)** A zoomed version of (a) showing subtle differences between the 2.5x, 20x, 40x, and 100x objectives as well as no appreciable signal in the case where no objective was present. **(c)** A simplified schematic of the isolated experimental setup. (Legend: SPF/LPF – short pass/long pass filter).

Appendix B – Additional fabrication and characterization information for pillar substrates

Pillar substrate fabrication began by piranha cleaning a thermally oxidized Si wafer. Next, a chrome mask was sputtered on using a Kurt J. Lesker CMS-18 DC Magnetron Sputtering System. The thickness of the chrome layer ultimately determines the height of the pillars. The wafer was then spin coated with AZ 1529 photoresist. The spin settings were 10 seconds at 500 RPM for the spread step and 60 seconds at 3000 RPM for the spin step. The resist was approximately 3.7 µm thick. A Heidelberg MLA 150 direct write lithography system was used to pattern the resist. This system was equipped with a 405 nm laser diode and set to deliver a dosage of 230 mJ/cm^2. Following patterning, the wafer was developed for 120 s in AZ 400K diluted to 1:4 to wash away the exposed resist. We noted that it was possible to produce nanopillars smaller than the minimum feature size of the MLA 150 through careful tuning of exposure and development times.

Once the resist was fully patterned, an Oxford Instruments inductively coupled plasma reactive ion etching (ICPRIE) system was used to etch through the chrome layer using the parameters in Table S1. The endpoint was determined visually though etches typically ran from 3-5 minutes. A separate RIE system was then used to strip away the remaining photoresist using the settings in Table S1. Now with the Cr serving as a mask for the underlying SiO_2, an oxide etch was performed in the Cobra ICPRIE system according to the parameters given in the final column of Table S1. A second Cr etch was then run to remove the remaining chrome mask. The wafer was once again coated with AZ 1529 for temporary protection and diced into 1 cm x 1 cm chips. Finally, acetone was used to remove the protective resist layer. Pillar heights typically ranged between 150 nm to 170 nm. **Fig. B.1** shows a schematic of the entire process.

Table B.1. Etching parameters for the pillar fabrication process.

Step	Cr Etch	O_2 Strip	SiO_2 Etch
Gas/Rate [sccm]	Cl_2/42	O_2/50	CHF_3/50
Gas/Rate [sccm]	O_2/8	N/A	SF_6/25
Gas/Rate [sccm]	N/A	N/A	Ar/25
Power [W]	1200	200	1000
Temp. [C]	20	20	20
Pressure [mT]	12	100	90

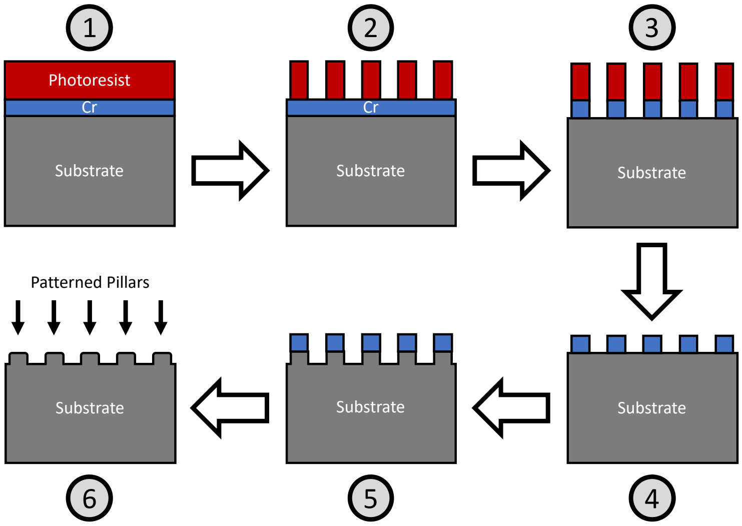

Fig. B.1. A schematic representation of the pillar fabrication process flow

Pillar substrates were comprised of 63 individual chips labelled A2 through H8 which were otherwise identical. The feature sizes on each chip ranged from 1 um to 8 um. Each individual chip was further sectioned into an 8 by 8 array of repeating unit cells. **Figure B.2** below shows one such unit cell. The minimum features size specified by the MLA 150 is on the order of 1 μm, which was also the smallest size of pillar fabricated. The 1 μm diameter pillars were clearly visible post-lithography but often ended up being smoothed over or washed away, presumably during the etching process. Most pillars ended up being smaller than designed, an observation we attribute to either exposure or development during photolithography.

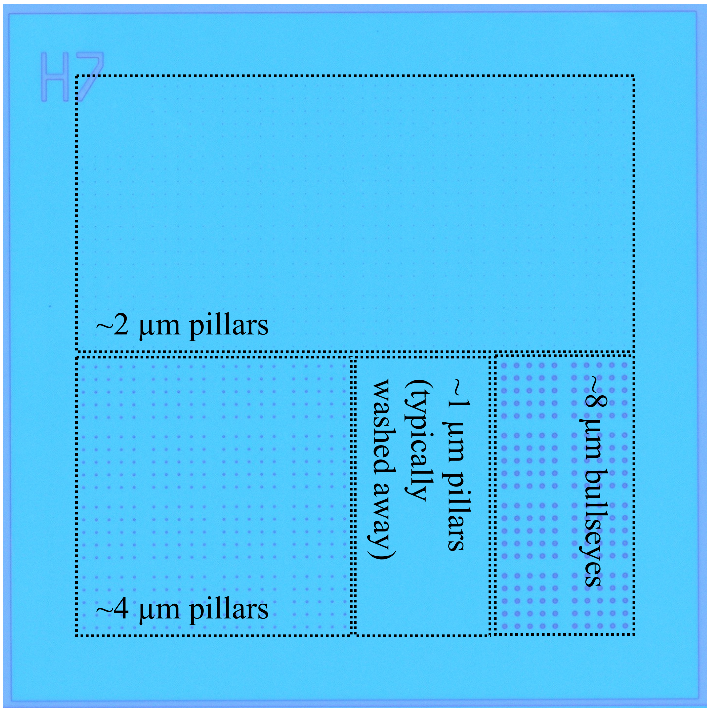

Fig. B.2. A unit cell containing patterned oxide structures that was used to obtain the results seen in Chapter 4.

Several issues were encountered during the process development of the pillar substrates first used in Chapter 3. First, it was observed that the RIE recipe used during the oxide etch often left “spikes” near the center of features. These spikes could significantly interfere with the hBN transfer process by piercing the film and thus disrupting the strain. This issue was mitigated by over etching whenever possible. **Figure B.3**(a) shows a pillar with a spike near the center. Spike artifacts near the center of some pillars could potentially be exploited as a method of localizing emission if fabricated reliably. The second issue was that the etching processes tended to leave behind an optically rough surface, as seen in **Fig. B.3**(b) below. The rough surfaces present in many of the devices undoubtably resulted in scattering but could likely be smoothed while still preserving sharp feature edges using a buffered oxide etch. Rough surfaces have the potential to trap contaminates as well as damage hBN films during the transfer process.

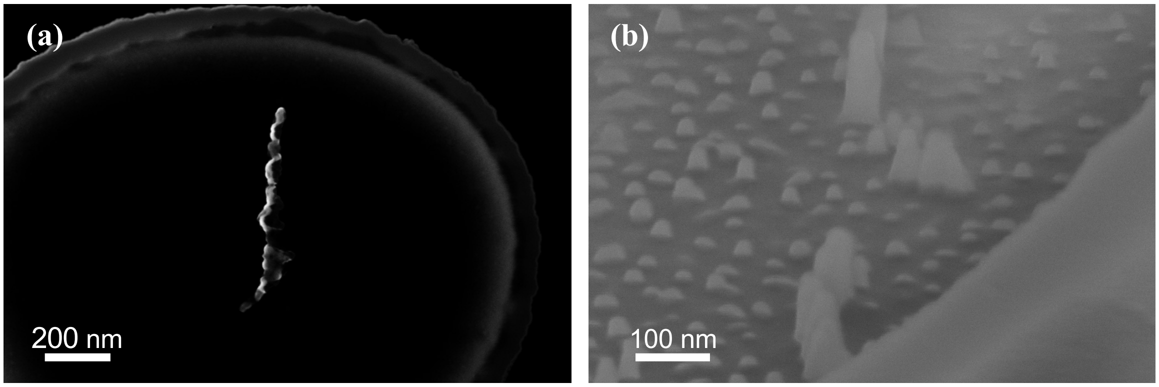

Fig. B.3. SEM images of interesting defects noticed early on in pillar fabrication. **(a)** A pillar with a spike on the top resulting from the reactive ion etching process. **(b)** Surface roughness that resulted from the reactive ion etching process.

In addition to what was presented in Chapter 4, a sampling of the final transfer product can be seen in **Fig. B.4**. Film regions near the edges of transfers were typically rougher than interior regions. Characteristic wrinkling and crackling can also be observed across all cells. Furthermore, hBN transfers were also carried out for hole samples, where the hBN was transferred to a substrate with the pillars mask inverted. This was done in preparation for integration with the buckled microcavity devices discussed in Chapter 5 when it was realized that the delamination process favoured holes rather than pillars. A sampling of the final transfer product can be seen in **Fig. B.5**

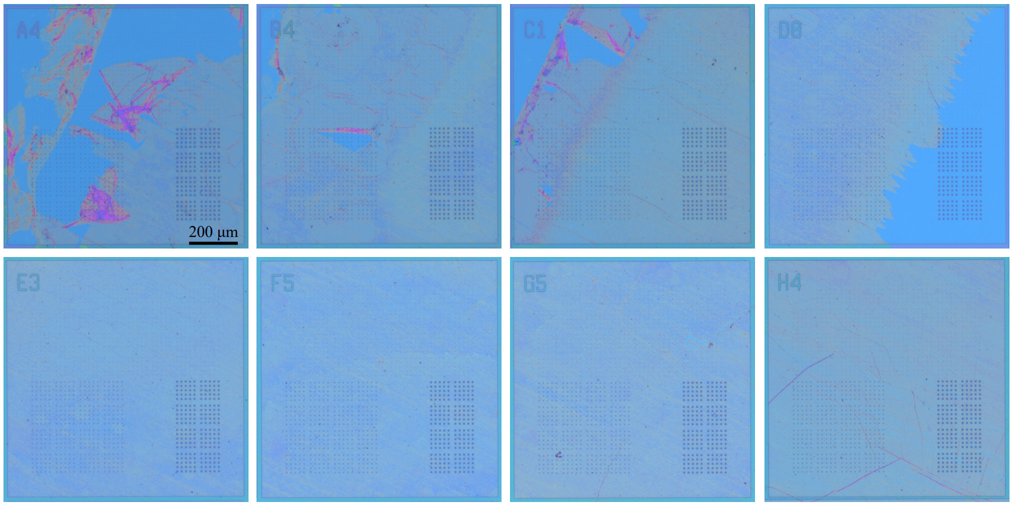

Fig. B.4. A sampling of BF images showing the success rate of the hBN transfer process on nanopillar substrates. The top row shows films edges while the bottom row shows interior regions.

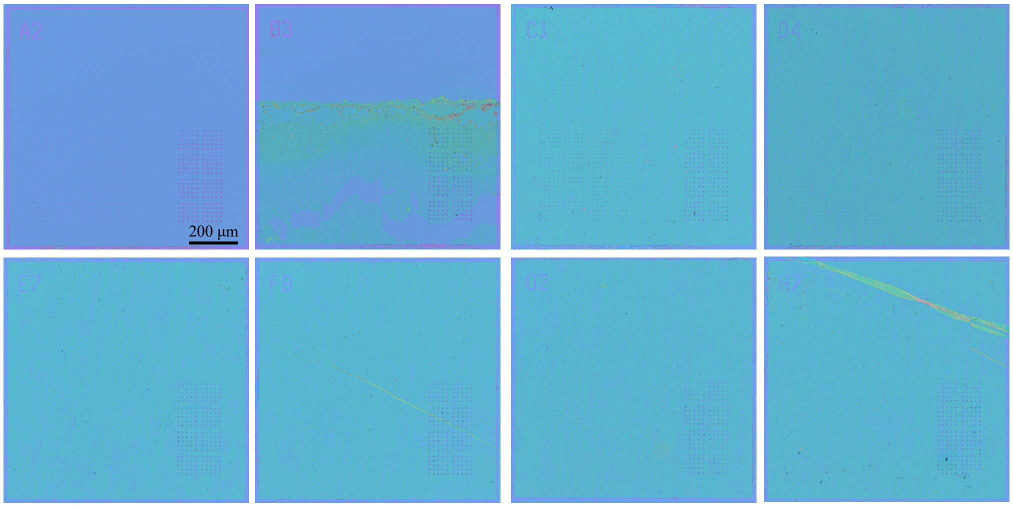

Fig. B.5. A sampling of BF images showing the success rate of the hBN transfer process on nanoholes substrates. Cell A2 is uncoated, cell B3 is partially coated, and the rest of the cells are completely coated. Wrinkles are visible in cells F8 and H7.

Several other variations of the hBN transfer process were also investigated in addition to what is reported in the main text of Chapter 4. **Figure B.6** presents a flow chart outlining the variations that did and did not result in a successful transfer process as well as general comments and observations. The process can largely be divided to into four general components: (i) coating one side of the CVD hBN on Cu foil with PMMA. (ii) Removing the undesired hBN and etching the Cu. (iii) Transferring the hBN/PMMA stack onto the target substrate. (iv) Removing the intermediate PMMA layer.

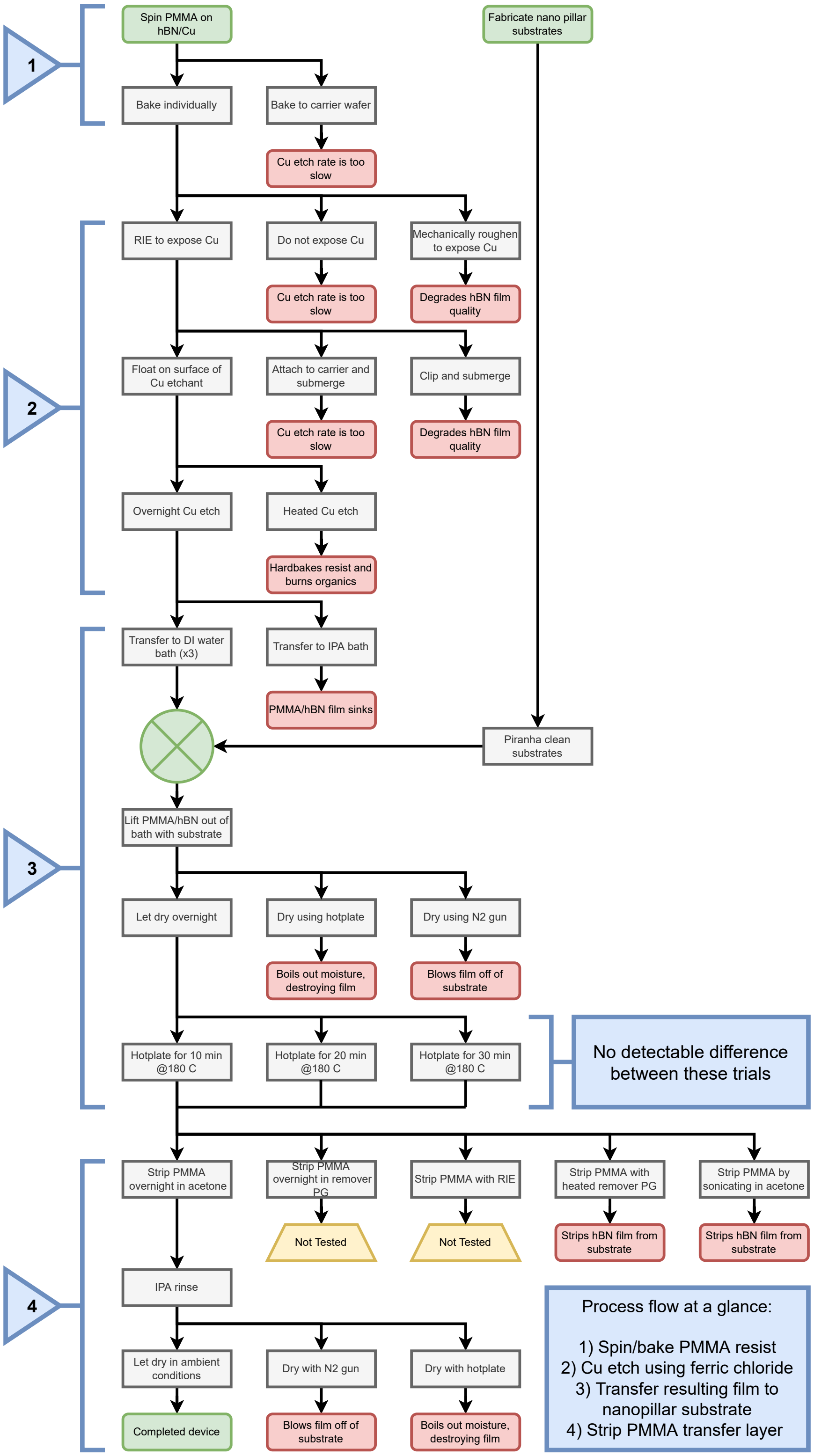

Fig. B.6. A flowchart schematic showing possible pathways for the hBN transfer process that ultimately led to the optimized version. Legend: green – start and end points, yellow – pathway not tested, red – failed pathway, blue – comments and overview.

All the spectral data presented in Chapter 4 was obtained with an Ocean Optics USB4000 spectrometer configured to have a ~ 7 nm resolution. The DeCorby lab was able to obtain an Ocean Optics QEPro thanks to the generosity of Wilson Analytical Inc. The QEPro had a resolution of > 1 nm and was an overall superior instrument in terms of noise floor, sensitivity, and dynamic range. **Figure B.7** shows photoluminescence results from an interesting hBN-coated micro-bullseye feature using this spectrometer.

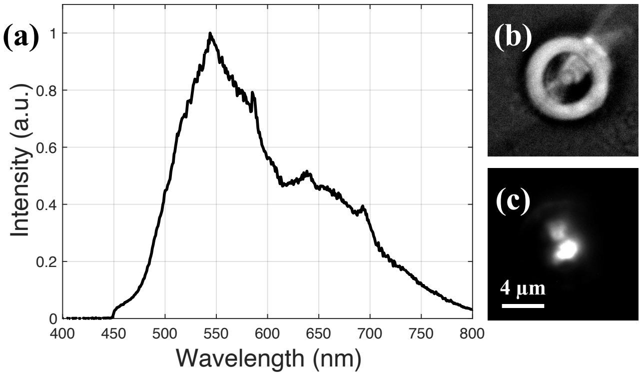

Fig. B.7. Photoluminescence results from a bullseye where the hBN has folded over the structure in an interesting way. **(a)** A non-background corrected PL spectra showing multiple peaks. **(b)** A BF image of the hBN coated region showing folding. **(c)** A PL image showing preferential emission from highly disturbed sites as well as some emission near the outer edge of the structure.

Appendix C – Additional fabrication and characterization information for buckled microcavity substrates

Figure C.1 shows index fits for Ta_2O_5 and SiO_2 obtained with a J. A. Woollam M-2000 ellipsometer. Extinction coefficients are not provided as they were too low to be fit to. The index of refraction values at the Bragg mirror design wavelength of 600 nm were 2.12 and 1.46 for Ta_2O_5 and SiO_2, respectively. This data was obtained from test layers prior to the deposition of the bottom mirror.

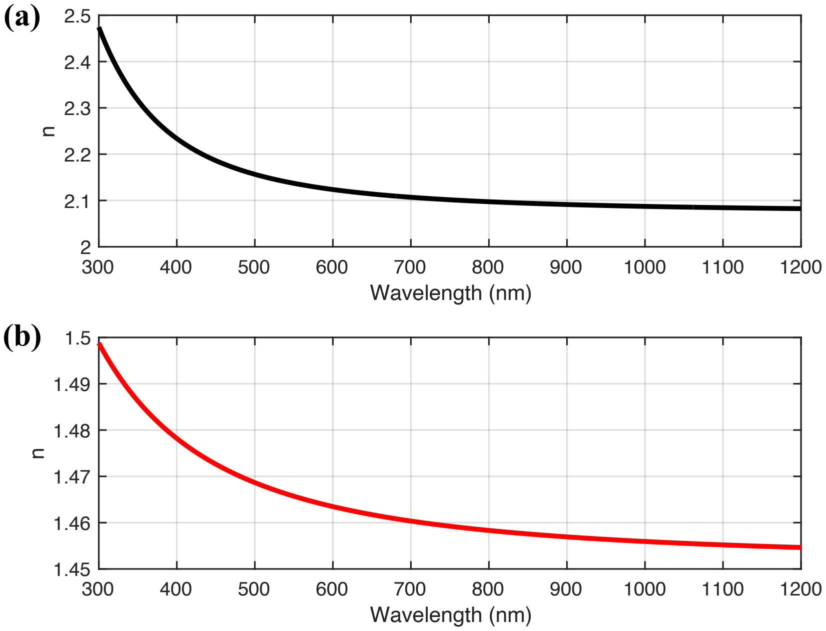

Fig. C.1. Index of refraction fits for **(a)** Ta_2O_5 and **(b)** SiO_2 based on test layer depositions in Sputtering System #2 (Doug). Obtained with a J. A. Woollam M-2000 Ellipsometer.

The bottom mirror and field optimization layer were characterized prior to hole etching and hBN transfer. This was done by measuring the reflectivity at 20°, 50°, and 80° with a J. A. Woollam VASE ellipsometer. The instrument design paired with the silicon substrate prohibited characterisation at normal incidence. Plots comparing the TE and TM polarizations for simulated and experimental data at a 20° angle of incidence can be seen in **Fig. C.2**. Interestingly, the experimental Bragg stopband spans a slightly greater wavelength range than the structure simulated using the material fits in **Fig. C.1**. This implies a slightly greater index contrast between the Ta_2O_5 and SiO_2 than initially measured.

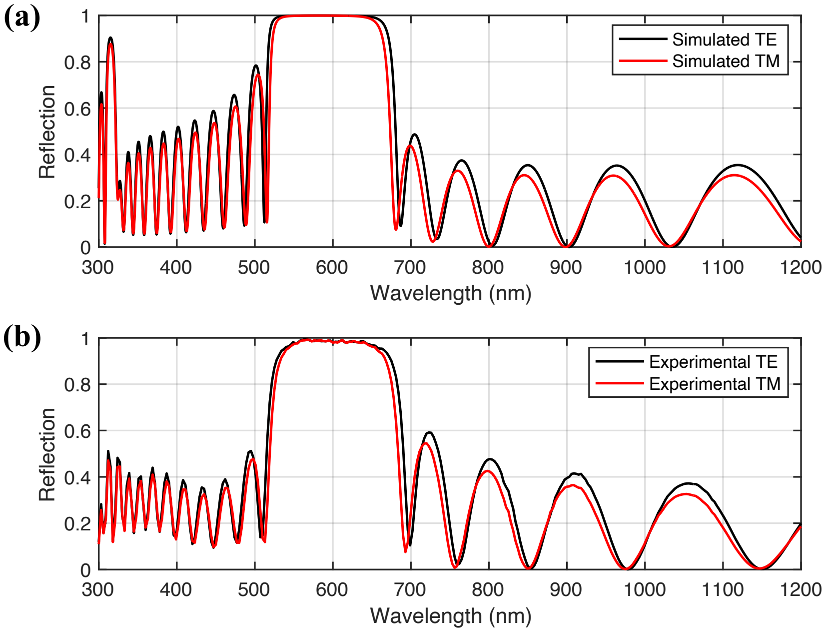

Fig. C.2. Reflectivity of the bottom 10.5 period Bragg mirror with field optimization layer at a 20° angle of incidence. **(a)** Simulated results based on transfer matrices. **(b)** Experimental results obtained with a VASE ellipsometer.

Figure C.3 shows images taken at various points in the fabrication process. A large-scale image representing an hBN transfer is shown in **Fig. C.3**(a). The edges of the film along with PMMA residue can approximately be made out, as indicated by the black arrows. **Figure C.3**(b) shows a film edge at a smaller scale. The film is difficult to se, but cracks and wrinkles characteristic to hBN can be made out. An image of patterned PTFE pads on the bottom mirror is also shown in **Fig. C.3**(c). Each pad is centered about a hole etched into the field optimization layer. The combination of the PTFE index and thickness made it difficult to see, hence the red filter applied to the image.

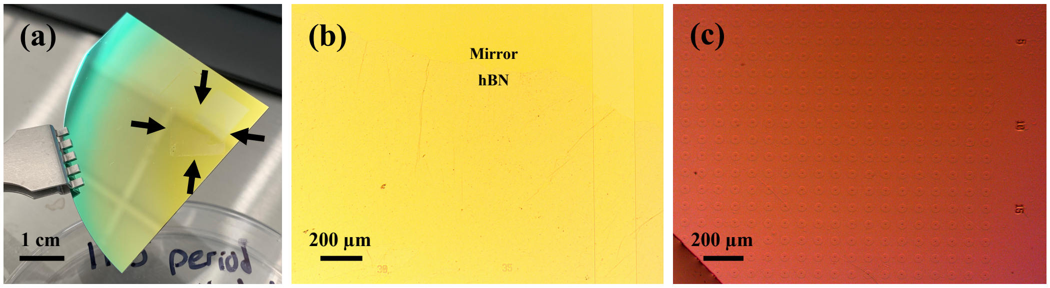

Fig. C.3. Images at various points in the fabrication process flow. **(a)** A quartered mirror piece with a transferred hBN film indicated by black arrows. **(b)** A microscope image showing the hBN film on the quartered mirror piece. **(c)** A microscope image showing arrays of PTFE pads on a quartered mirror piece.

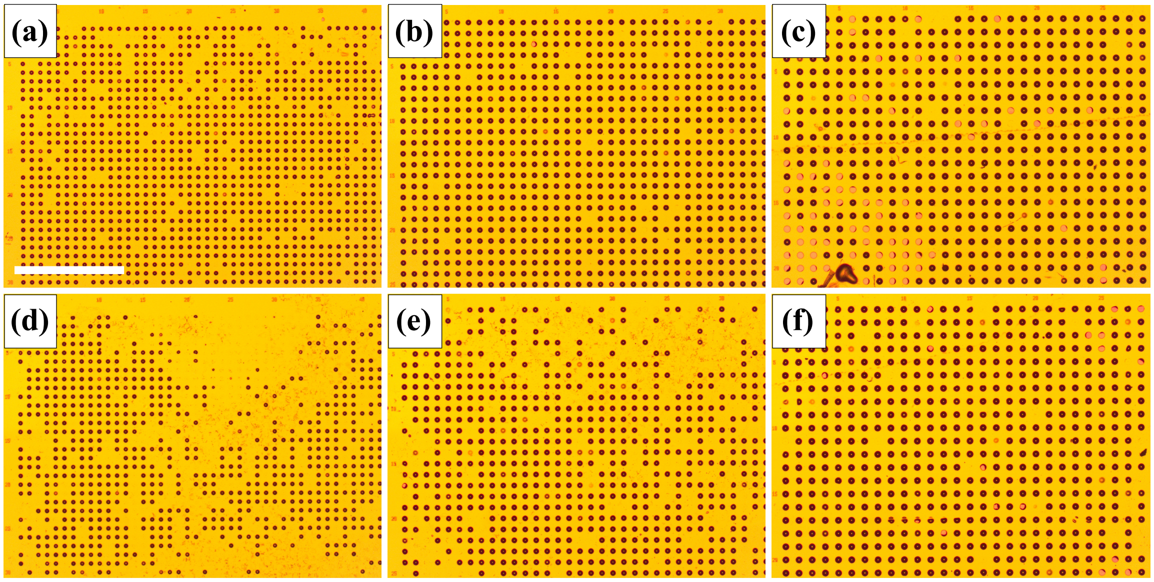

Fig. C.4. Arrays of (gold-coated) domes with different diameters containing holes of different sizes. Scale bar represents 1 mm. **(a)** 40 μm diameter domes containing 1 μm diameter holes. **(b)** 50 μm diameter domes containing 1 μm diameter holes. **(c)** 60 μm diameter domes containing 1 μm diameter holes. **(d)** 40 μm diameter domes containing 2 μm diameter holes. **(e)** 50 μm diameter domes containing 2 μm diameter holes. **(f)** 60 μm diameter domes containing 2 μm diameter holes.

Devices typically existed in three distinct states after buckling. The first is buckled, where the top mirror successfully separated from the bottom mirror in a cylindrically symmetrical manner. The second is a pop-off, where the top mirror over the patterned PTFE separated entirely from the substrate, leaving the bottom mirror exposed. The third device state is unbuckled, where the top mirror did not separate from the bottom mirror at all, leaving the device looking much like it did prior to the buckling process. **Figure C.5** shows examples for each type of device. The 2 μm holes etched into the mirror can also be seen in the center of each dome.

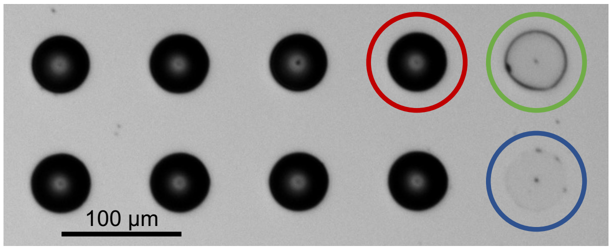

Fig. C.5. A microscope image showing an array of domes with circled examples. Legend: red – buckled, green – popped off, blue – unbuckled.

It was noted that the low-adhesion fluorocarbon layer exhibited a broad, low amplitude fluorescence across most of the visible range that was ~ 10x dimmer than that obtained from CVD-hBN on Cu. Measurements were taken using an integration time of 5 seconds with the 100x objective in **Table 3.2**. The approximate beam spot size is shown at collection areas for reference. A photoluminescence measurement of the bare silicon next to the patterned fluorocarbon is also provided to show that there is no appreciable signal, demonstrating that the signal observed in **Fig. C.6**(b) is likely not due to scattered light, autofluorescence, etc. While bulk PTFE is not known to fluoresce [151], the low-adhesion layers deposited here were typically on the order of 10 – 20 nm which may result in material characteristics that differ from the bulk material and could explain the emission. Our measured spectrum is also similar to what has been reported previously [145].

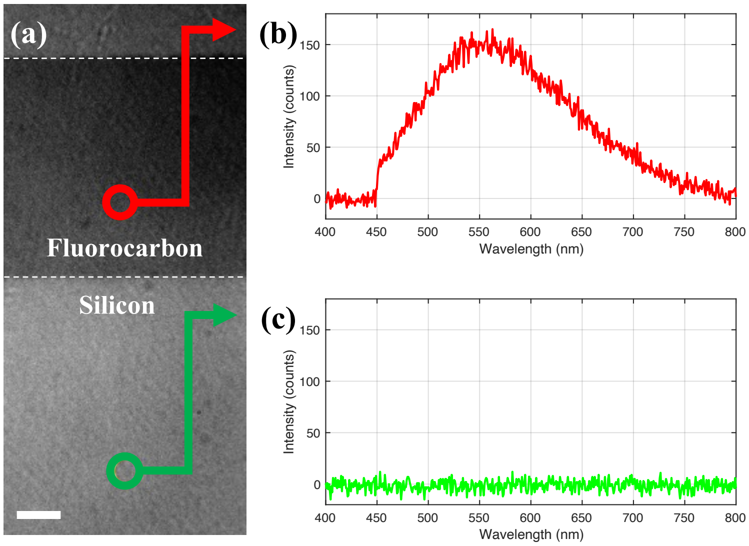

Fig. C.6. The initial discovery that thin-film fluorocarbon emits light in the visible range when pumped with a 405 nm laser (~ 4 mW of incident power). **(a)** A bright field image showing pattern patterned fluorocarbon on silicon with a 10 µm scale bar. **(b)** Photoluminescence signal obtained from patterned fluorocarbon. **(c)** Photoluminescence obtained from bare silicon showing no appreciable signal.

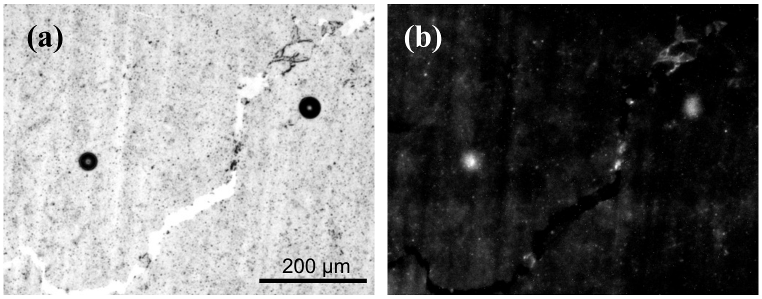

Fig. C.7. Accidental domes formed by delamination of the hBN film in non-patterned areas. **(a)** A bright field image clearly showing two domes of different sizes. **(b)** A photoluminescence image showing emission originating from the dome areas.

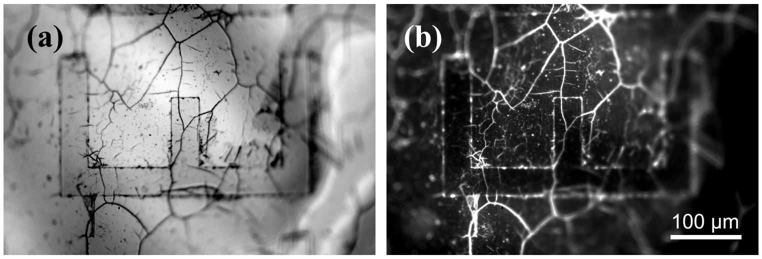

Fig. C.8. An area where a large, millimeter-sized portion of the hBN film has delaminated. The differences in buckle height across the film are greater than the depth of focus of the objective used, making certain areas appear blurred. **(a)** A bright field image. **(b)** A photoluminescence image.

After discovering that reflection measurements of the buckled microcavities could not be obtained using the microscope setup described in Chapter 3, a series of proof-of-concept measurements were carried out using fiber reflection scheme with an NIR dome sample. **Fig. C.9** shows an example measurement performed with a standard cleaved SMF-28 fiber. An NKT SuperK COMPACT supercontinuum source was launched into a fused-fiber bidirectional coupler. A cleaved SMF-28 fiber was used at the tapped output to couple light into the cavity mode as well as collect reflected light. The unused output was capped with a fiber terminator. A Yokogawa OSA was used at the tapped input to measure the reflected signal. The sample reflection measurement was performed with membrane-in-the-middle devices fabricated by Lintong Bu (**Fig. C.9**(a)). It should be noted that this measurement has also been successfully attempted with a tapered fiber chosen to match the numerical aperture of the devices studied, though the availability of such tapers in the visible range prevented this measurement from being transferred over.

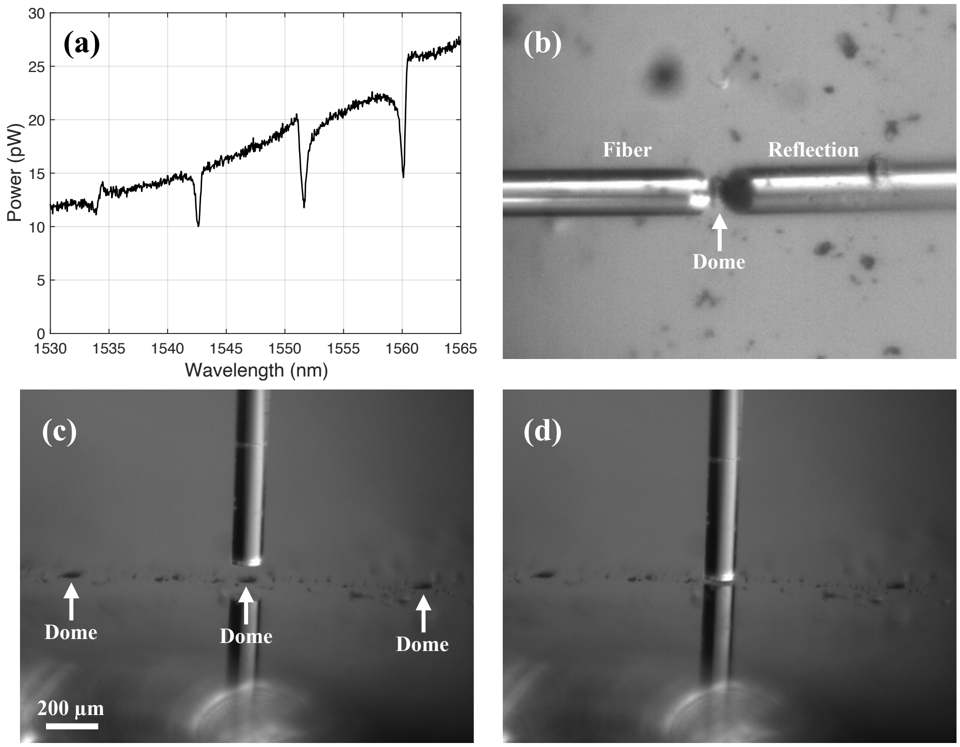

Fig. C.9. Proof of concept for reflection measurements with a cleaved fiber performed around 1550 nm. **(a)** An unnormalized reflection spectrum. **(b)** A camera view from the side with the fiber backed off showing the fiber, dome, and fiber reflection. **(c)** A camera view from the top with the fiber backed off showing an array of domes. **(d)** A camera view from the top showing the fiber to dome distance required for reflection measurements.

The proof-of-concept measurement system was adapted for visible range measurements in which case a spectrometer was used instead of an OSA. **Figure C.10**(a) shows a transmission plot of the source (NKT SuperK COMPACT) connected to a single mode fiber (Thorlabs 460HP) and aligned to the spectrometer (Ocean Optics QEPro) in free space. The spectrum is relatively ripple free when multimode fiber is avoided. **Figure C.10**(b) shows a reflection plot corresponding to a planar region on the samples described in Chapter 5. Characteristic Bragg mirror spectral features are present including the stopband, but there are no sequential notches indicative of cavity modes.

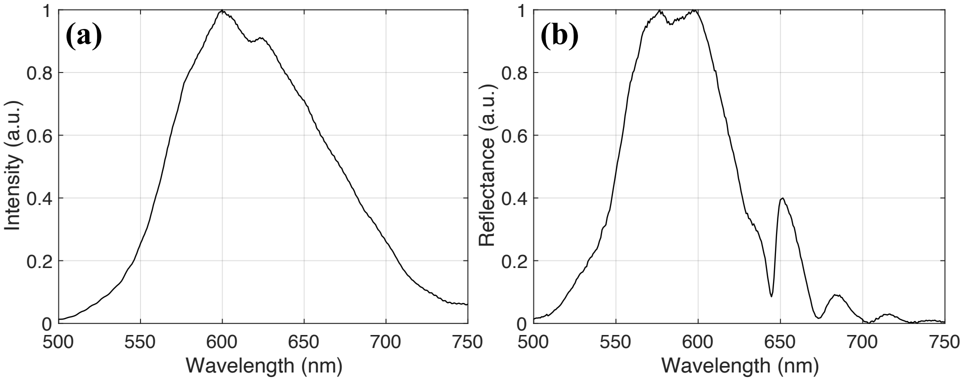

Fig. C.10. Supplementary reflection plots using a cleaved fiber in the visible range. **(a)** A plot showing the lineshape of the source used for visible range tapered fiber reflection measurements. **(b)** A reflection measurement of a planar region where no cavity modes are present.

In some cases, it was noticed that a Fabry Perot cavity formed between the dome and cleaved fiber resulting that appeared to depend on the working distance of the fiber. Some domes exhibited a particularly interesting phenomenon where a broad notch, possibly attributable to this unintentional Fabry Perot, appeared to shift in wavelength as heat was applied to the dome. **Figure C.11** shows one case where this has happened to a 60 µm dome over a 30 second period. Thermal tuning of domes typically results in resonances shifting to higher wavelengths as the airgap between the top and bottom mirrors lengthens. The opposite was observed here, which is consistent with the unintentional Fabry Perot theory. However, the process observed here does not seem to be reversible, causing further contradiction.

Alternatively, the true power circulating inside the dome could be significant enough to vaporize the PTFE low-adhesion layer, which might blue shift cavity features. This theory is also supported by the fact the spectral drifting doesn't seem to be reversible. However, the refractive index of the thin-film PTFE used in the fabrication of buckled dome microcavities is typically between 1.4 and 1.5. A 15 nm layer of PTFE should not be able to induce a ~ 25 nm shift in wavelength.

Finally, it is possible that this thermal drift is the result of further induced buckling caused by the thermal power provided by the NKT. This would explain why this phenomenon was only observed a handful of times, as well as why it was not reversible. Further study would be required to make any definitive claims.

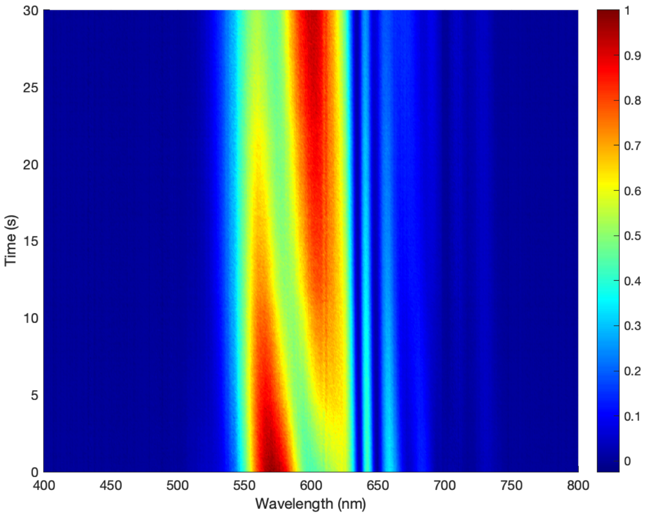

Fig. C.11. A time trace diagram showing the effect of temperature on a certain dome. The time/temperature dependent notch could be due to a Fabry Perot cavity formed between the dome and cleaved fiber which changes in length as the dome is heated.

Appendix D – Streamlined Lumerical code for simulating buckled microcavity structures

The code presented below is a streamlined version of what has previously been used by the DeCorby group and can be used as a starting point for future work. Several other important features have been added including field apodization, automated layer calculations, and the creation of mirror layers through looping. It is my hope that this well-commented code will save future students time and significantly speed up the creation of related models.

```
##################################################################
# Title: ExampleScriptForThesis600nm                             #
# Authors: Kyle Scheuer, Phillip Kirwin, Ray DeCorby             #
# Date: March 01, 2022                                           #
#                                                                #
# A useful template for anyone who is interested in simulating   #
# buckled dome microcavities. This version generates a           #
# symmetrical 10.5 period Ta2O5/SiO2 mirror separated by a 300   #
# nm airgap with the dipole placed in the very center.           #
##################################################################

###### Clear all data ######
deleteall;
if (materialexists("Ta2O5"))
{
    deletematerial("Ta2O5");
}
if (materialexists("SiO2"))
{
    deletematerial("SiO2");
}

###### Add materials ######
mymaterial2=addmaterial("(n,k) Material");
setmaterial(mymaterial2,"name","Ta2O5");
setmaterial("Ta2O5", "color",[0.1,0.2,1,0.9]);
setmaterial("Ta2O5","Refractive Index", 2.1041);
setmaterial("Ta2O5","Imaginary Refractive Index", 0);

mymaterial2=addmaterial("(n,k) Material");
setmaterial(mymaterial2,"name","SiO2");
setmaterial("SiO2", "color",[0.1,0.6,0.3,0.9]);
setmaterial("SiO2","Refractive Index", 1.4737);
setmaterial("SiO2","Imaginary Refractive Index", 0);

###### Set constants ######
r_dome = 20e-6;
target_lambda = 600e-9;
lambdastart = 585e-9;
lambdastop = 610e-9;
lambdanum = 20;
num_period = 10.5;
dH = real(target_lambda/(4*getindex("Ta2O5",1)));
dL = real(target_lambda/(4*getindex("SiO2",1)));
period = dH+dL;
dA = target_lambda/2; # peak buckle height
```

```
###### Create bottom structures and layers ######
addstructuregroup;
set("name","bottom");
set("x",0); set("y",0); set("z",0);
x_res = 120;
y_res = 120;
x=linspace(-1.2*r_dome,1.2*r_dome,x_res);
y=linspace(-1.2*r_dome,1.2*r_dome,y_res);
X = meshgridx(x,y);
Y = meshgridy(x,y);
Z = 0*ones(x_res,y_res);

# Extra high index layer (N+1/2)
addimport;
set("name","hi index 1");
set("render type","detailed");
set("detail",0.1);
importsurface2(Z,x,y);
importsurface2(Z,x,y,0);
set("upper ref height",0);
set("lower ref height",-dH);
set("material","Ta2O5");
addtogroup("bottom");

# Build layers
for(p=1:num_period)
{
    # Low index
    addimport;
    set("name","lo index " + num2str(p));
    set("render type","detailed");
    set("detail",0.1);
    Z = Z - dH;
    importsurface2(Z,x,y);
    importsurface2(Z,x,y,0);
    set("upper ref height",0);
    set("lower ref height",-dL);
    set("material","SiO2");
    addtogroup("bottom");

    # High Index
    addimport;
    set("name","hi index " + num2str(p+1));
    set("render type","detailed");
    set("detail",0.1);
    Z = Z - dL;
    importsurface2(Z,x,y);
    importsurface2(Z,x,y,0);
    set("upper ref height",0);
    set("lower ref height",-dH);
    set("material","Ta2O5");
    addtogroup("bottom");
}

# Add silicon substrate
addimport;
set("name","Si substrate");
set("render type","detailed");
set("detail",0.1);
Z = Z - dH;
importsurface2(Z,x,y);
importsurface2(Z,x,y,0);
set("upper ref height",0);
set("lower ref height",-1e-6);
set("material","Si (Silicon) - Palik");
addtogroup("substrate");

###### Create upper structures and layers ######
addstructuregroup;
```

```
set("name","upper");
set("x",0); set("y",0); set("z",0);
x_res = 120;
y_res = 120;
x=linspace(-1.2*r_dome,1.2*r_dome,x_res);
y=linspace(-1.2*r_dome,1.2*r_dome,y_res);
X = meshgridx(x,y);
Y = meshgridy(x,y);
r = sqrt(X^2+Y^2);
# Bessel function models buckle geometry
Z = dA*(0.2871+0.7129*besselj(0, 3.8317*sqrt(X^2+Y^2)/r_dome));

# Zero area surrounding dome
for(qx=1:x_res)
{
    for(qy=1:y_res)
    {
        if(sqrt(X(qx,qy)^2+Y(qx,qy)^2) > r_dome)
        {
            Z(qx,qy) = 0;
        }
    }
}

# Extra high index layer (N+1/2)
addimport;
set("name","hi index 1");
set("render type","detailed");
set("detail",0.1);
importsurface2(Z,x,y);
importsurface2(Z,x,y,0);
set("upper ref height",dH);
set("lower ref height",0);
set("material","Ta2O5");
addtogroup("upper");

# Build layers
for(p=1:num_period)
{
    # Low index
    addimport;
    set("name","lo index " + num2str(p));
    set("render type","detailed");
    set("detail",0.1);
    Z = Z + dH;
    importsurface2(Z,x,y);
    importsurface2(Z,x,y,0);
    set("upper ref height",dL);
    set("lower ref height",0);
    set("material","SiO2");
    addtogroup("upper");

    # High Index
    addimport;
    set("name","hi index " + num2str(p+1));
    set("render type","detailed");
    set("detail",0.1);
    Z = Z + dL;
    importsurface2(Z,x,y);
    importsurface2(Z,x,y,0);
    set("upper ref height",dH);
    set("lower ref height",0);
    set("material","Ta2O5");
    addtogroup("upper");
}

###### Perform meshing ######
mesh_dx = 100e-9;
mesh_dy = 100e-9;
```

```
mesh_dz = period/10; # mesh periodically

# Mesh bottom mirror
addmesh;
set("name","bottom");
set("set maximum mesh step",1);
set("override x mesh",1);
set("override y mesh",1);
set("override z mesh",1);
set("dx",mesh_dx);
set("dy",mesh_dy);
set("dz",mesh_dz);
set("based on a structure",1);
set("structure","bottom");

# Mesh top mirror
addmesh;
set("name","upper");
set("set maximum mesh step",1);
set("override x mesh",1);
set("override y mesh",1);
set("override z mesh",1);
set("dx",mesh_dx);
set("dy",mesh_dy);
set("dz",mesh_dz);
set("based on a structure",1);
set("structure","upper");

# Mesh cavity
addmesh;
set("name","cavity");
set("set maximum mesh step",1);
set("override x mesh",1);
set("override y mesh",1);
set("override z mesh",1);
set("dx",mesh_dx);
set("dy",mesh_dy);
set("dz",mesh_dz);
set("x",0);
set("x span",2*r_dome);
set("y",0);
set("y span",2*r_dome);
set("z",dA/2);
set("z span",dA);

###### FDTD ######
fdtd_x_span = 2*r_dome;
fdtd_y_span = 2*r_dome;
fdtd_z_span =24*period+dA;
addfdtd;
set("dimension",2);  #  1 = 2D, 2 = 3D
set("x",0);
set("x span",fdtd_x_span);
set("y",0);
set("y span",fdtd_y_span);
set("z",2*(dH+dA)/4);
set("z span",fdtd_z_span);
set("y min bc","Symmetric");
set("x min bc","anti-Symmetric");
set("simulation time",6000e-14);
set("mesh accuracy",2);
set("pml profile",1);
set("auto shutoff min",1e-20);
set("index",1);
set("pml profile",1);
set("same settings on all boundaries",0);
# setting z min bc to "stabilized", and all other bc to "standard"
set("pml profile", [1,1,1,1,2,1]);
```

```
###### Add dipole ######
dz = dA/2;
adddipole;
set("x",0);
set("y",0);
set("z",dz);
set("theta",90);
set("wavelength start",lambdastart);
set("wavelength stop",lambdastop);

###### addtime point ######
addtime;
set("name","time");
set("monitor type",1);  # 1 = point
set("x",0);
set("y",0);
set("z",dz - 2*mesh_dz);
set("start time",200e-15);

###### addpower normal z ######
addpower;
set("name","Z-normal");
set("monitor type",7);  # 7 = 2D z-normal
set("x",0);
set("x span",2*r_dome);
set("y",0);
set("y span",2*r_dome);
set("z",dA + 11*period);
setglobalmonitor("frequency points",lambdanum);
set("apodization",3); # 3 = start
set("apodization center",5e-12);
set("apodization time width",1e-12);
set("output power",0);
set("output Hx",0);
set("output Hy",0);
set("output Hz",0);

###### addpower normal x ######
addpower;
set("name","x_normal_Powermonitor");
set("monitor type",5); # 5 = 2D x-normal
set("x",0.5*dA);
set("y",0);
set("y span",2*r_dome);
set("z",(dA)/2);
set("z span",21*period+dA);
setglobalmonitor("frequency points",lambdanum);
set("apodization",3); # 3 = start
set("apodization center",5e-12);
set("apodization time width",1e-12);
set("output power",0);
set("output Hx",0);
set("output Hy",0);
set("output Hz",0);

setglobalsource("wavelength start",lambdastart);
setglobalsource("wavelength stop",lambdastop);
```